SpringerBriefs in Physics

S. Lakshmibala · V. Balakrishnan

Nonclassical Effects and Dynamics of Quantum Observables

Springer

SpringerBriefs in Physics

Series Editors

Balasubramanian Ananthanarayan, Centre for High Energy Physics, Indian Institute of Science, Bangalore, Karnataka, India

Egor Babaev, Department of Physics, Royal Institute of Technology, Stockholm, Sweden

Malcolm Bremer, H. H. Wills Physics Laboratory, University of Bristol, Bristol, UK

Xavier Calmet, Department of Physics and Astronomy, University of Sussex, Brighton, UK

Francesca Di Lodovico, Department of Physics, Queen Mary University of London, London, UK

Pablo D. Esquinazi, Institute for Experimental Physics II, University of Leipzig, Leipzig, Germany

Maarten Hoogerland, University of Auckland, Auckland, New Zealand

Eric Le Ru, School of Chemical and Physical Sciences, Victoria University of Wellington, Kelburn, Wellington, New Zealand

Dario Narducci, University of Milano-Bicocca, Milan, Italy

James Overduin, Towson University, Towson, MD, USA

Vesselin Petkov, Montreal, QC, Canada

Stefan Theisen, Max-Planck-Institut für Gravitationsphysik, Golm, Germany

Charles H. T. Wang, Department of Physics, University of Aberdeen, Aberdeen, UK

James D. Wells, Department of Physics, University of Michigan, Ann Arbor, MI, USA

Andrew Whitaker, Department of Physics and Astronomy, Queen's University Belfast, Belfast, UK

SpringerBriefs in Physics are a series of slim high-quality publications encompassing the entire spectrum of physics. Manuscripts for SpringerBriefs in Physics will be evaluated by Springer and by members of the Editorial Board. Proposals and other communication should be sent to your Publishing Editors at Springer.

Featuring compact volumes of 50 to 125 pages (approximately 20,000–45,000 words), Briefs are shorter than a conventional book but longer than a journal article. Thus, Briefs serve as timely, concise tools for students, researchers, and professionals.

Typical texts for publication might include:

- A snapshot review of the current state of a hot or emerging field
- A concise introduction to core concepts that students must understand in order to make independent contributions
- An extended research report giving more details and discussion than is possible in a conventional journal article
- A manual describing underlying principles and best practices for an experimental technique
- An essay exploring new ideas within physics, related philosophical issues, or broader topics such as science and society

Briefs allow authors to present their ideas and readers to absorb them with minimal time investment. Briefs will be published as part of Springer's eBook collection, with millions of users worldwide. In addition, they will be available, just like other books, for individual print and electronic purchase. Briefs are characterized by fast, global electronic dissemination, straightforward publishing agreements, easy-to-use manuscript preparation and formatting guidelines, and expedited production schedules. We aim for publication 8–12 weeks after acceptance.

S. Lakshmibala · V. Balakrishnan

Nonclassical Effects and Dynamics of Quantum Observables

Springer

S. Lakshmibala
Department of Physics
Indian Institute of Technology Madras
Chennai, India

V. Balakrishnan
Department of Physics
Indian Institute of Technology Madras
Chennai, India

ISSN 2191-5423 ISSN 2191-5431 (electronic)
SpringerBriefs in Physics
ISBN 978-3-031-19413-9 ISBN 978-3-031-19414-6 (eBook)
https://doi.org/10.1007/978-3-031-19414-6

© The Author(s), under exclusive license to Springer Nature Switzerland AG 2022
This work is subject to copyright. All rights are solely and exclusively licensed by the Publisher, whether the whole or part of the material is concerned, specifically the rights of translation, reprinting, reuse of illustrations, recitation, broadcasting, reproduction on microfilms or in any other physical way, and transmission or information storage and retrieval, electronic adaptation, computer software, or by similar or dissimilar methodology now known or hereafter developed.
The use of general descriptive names, registered names, trademarks, service marks, etc. in this publication does not imply, even in the absence of a specific statement, that such names are exempt from the relevant protective laws and regulations and therefore free for general use.
The publisher, the authors, and the editors are safe to assume that the advice and information in this book are believed to be true and accurate at the date of publication. Neither the publisher nor the authors or the editors give a warranty, expressed or implied, with respect to the material contained herein or for any errors or omissions that may have been made. The publisher remains neutral with regard to jurisdictional claims in published maps and institutional affiliations.

This Springer imprint is published by the registered company Springer Nature Switzerland AG
The registered company address is: Gewerbestrasse 11, 6330 Cham, Switzerland

Preface

Our job in physics is to see things simply, to understand a great many complicated phenomena in a unified way, in terms of a few simple principles.

—Steven Weinberg

The divide between classical and quantum physics, where and how this divide blurs, and proposals to identify genuinely quantum effects have been aspects of immense interest for researchers since the early days of the discovery of quantum laws. Several questions of both philosophical and practical importance have been raised through different approaches to understanding these aspects. Notably, optics provides an ideal platform for examining possible overlaps between the classical and quantum worlds, as interference, coherence, polarization, and even entanglement can be recognized, experimentally tested, and analyzed within both the classical and quantum settings. Significant progress in identifying inherently quantum effects has been made in recent years by means of novel experiments supported by theoretical arguments. In many situations, however, universally acceptable quantities that will unequivocally signal the classical or quantum nature of specific phenomena are not available.

Not surprisingly, therefore, diverse approaches have been developed even within the setting of optics, in order to examine the underlying nature of physical processes as varied as photosynthesis, superradiance, and manifestations of entanglement. The availability of several novel states of light that are nonclassical in the sense that they depart from ideal coherence, and could exhibit different types of squeezing, has given tremendous impetus to both theoretical and experimental investigations aimed at understanding the overlap between the classical and quantum descriptions. The framework of spin systems and hybrid quantum systems of light-matter interactions provides the possibility of examining nonclassical effects in relatively lower-dimensional Hilbert spaces than those of continuous variables, as exemplified by the radiation field. Extensive current research uses these platforms to understand the nature of genuine quantum entanglement and its connections, if any, with squeezing.

In this work, we focus primarily on two approaches to understanding the quantum regime. The first is based on the recognition that the basic laws of probability theory

govern both the classical and quantum domains. Much work is being done to understand the quantum nature of macroscopic phenomena using tests based on probability theory. In particular, we recognize that, while quasiprobability functions such as the Wigner distribution are used as standard identifiers of the nonclassicality of quantum states, the tomograms from which they are constructed are genuine probability distributions. Investigations carried out using only tomograms (we shall refer to this loosely as the tomographic approach) could help in understanding the limitations on extracting information about quantum states without undertaking state reconstruction from tomograms. The second approach is based on the recognition that the temporal evolution of quantum observables could well be converted into long time series of data, and the tools of time series and network analysis, which are well developed in the treatment of classical dynamical variables, could be applied to such data. Together with the understanding that the quantum wave packet revival phenomenon is similar to Poincaré recurrences in classical phase space, this approach has the potential to identify the limitations of the classical toolbox in a quantum setting. Since our focus is primarily on these two approaches, it is inevitable that the references cited in this work comprise only a small subset of the extensive and growing literature on nonclassical effects, tomograms, and the analysis of large data sets.

We acknowledge with pleasure discussions with several former students of ours over more than two decades, which enhanced our comprehension of several aspects of quantum physics. In particular, we recall numerous helpful conversations with Drs. S. Seshadri, C. Sudheesh, Athreya Shankar, Pradip Laha, and B. Sharmila. Our sincere thanks to Pradip for readily creating and sharing a substantial part of the contents and plots that we have used in Chaps. 3, 6, and 7. This work would not have been possible but for the painstaking and tireless effort put in by Sharmila who has been with us through every stage of the preparation of this manuscript, sharing relevant files and formatting the various chapters. Our very special thanks to her. We also thank Dr. S. Ramanan for her invaluable technical assistance during the preparation of the manuscript. Finally, we record our thanks to Drs. B. Ananthanarayan (IISc) and Lisa Scalone (Springer) for editorial advice and support.

The authors were supported, in part, by a grant from Mphasis to the Center for Quantum Information, Communication, and Computing (CQuICC).

We dedicate this work with affectionate gratitude to our respective parents and grandparents.

Chennai, India
September 2022

S. Lakshmibala
V. Balakrishnan

Contents

1 Introduction 1
References 17

2 Revivals, Fractional Revivals and Tomograms 21
2.1 Introduction 21
2.2 Basic Mechanism of Wave Packet Revivals 23
2.3 An Illustrative Example 24
2.4 Signatures of Revivals in Expectation Values of Observables 26
2.5 Effect of an Imperfectly Coherent Initial State 29
2.6 Revivals in Single-Mode Systems: A Tomographic Approach 32
2.7 Decoherence Effects 36
2.8 A Tomographic Approach to the Double-Well BEC System 37
References 41

3 Tomographic Approach to Squeezing 43
3.1 Introduction 43
3.2 Entropic Squeezing from Optical Tomograms 45
3.3 Quadrature and Higher-Order Squeezing from Optical Tomograms 48
References 52

4 Entanglement at Avoided Level Crossings 53
4.1 Introduction 53
4.2 Entanglement Indicators from Optical and Qubit Tomograms 55
4.3 Entanglement Indicators and Squeezing in Spin Systems 58
4.4 Bipartite CV Models and Avoided Level Crossings 63
4.5 Avoided Crossings in Multipartite HQ Systems: The Tavis–Cummings Model 66
References 68

5 Dynamics and Entanglement Indicators in Bipartite CV Systems 71
5.1 Introduction 71
5.2 The Bipartite Atom-Field Interaction Model Revisited 72
5.2.1 Time Evolution 72
5.2.2 Entanglement Dynamics 75
5.2.3 Tomographic Entanglement Indicators During Time Evolution 77
5.3 The Double-Well BEC Model Revisited 79
5.3.1 Time Development 79
5.3.2 Decoherence Effects in the Double-Well BEC Model 80
References 81

6 Dynamics of Entanglement Indicators in Hybrid Quantum and Spin Systems 83
6.1 Introduction 83
6.2 The Double Jaynes-Cummings Model 84
6.2.1 Dynamics 84
6.2.2 Equivalent Circuit for the DJC Model and the IBM Q Platform 86
6.3 The Double Tavis-Cummings Model 88
6.3.1 The Model 88
6.3.2 Equivalent Circuit and the IBM Q Platform 88
6.4 Bipartite Entanglement in Tripartite Models 89
6.4.1 The Cavity Optomechanical System 90
6.4.2 Λ-Atom Interacting with Radiation Fields 93
6.5 Entanglement and Squeezing in NMR Experiments 96
6.5.1 NMR Experiment I 98
6.5.2 Blockade and Freezing in Nuclear Spins 101
6.6 Concluding Remarks 104
References 105

7 Dynamics of the Mean Photon Number: Time Series and Network Analysis 107
7.1 Introduction 107
7.2 Brief Overview of Time Series Analysis 108
7.3 The Bipartite Atom-Field Interaction Model: Time Series Analysis 110
7.3.1 Dynamics 110
7.3.2 Power Spectrum and Lyapunov Exponent 111
7.3.3 Recurrence Statistics 113
7.4 Three-Level Atom Interacting with Radiation Fields 114
7.5 The Tripartite HQ Model with Intensity-Dependent Couplings 116
7.5.1 The Model 116
7.5.2 Time Series Analysis with Large and Small Data Sets 117
7.5.3 Return Maps and Recurrence Time Distributions 118

7.5.4 Recurrence Plots and Recurrence Network 119
7.5.5 Network Analysis 123
7.6 Concluding Remarks 125
References 125

8 Conclusion and Outlook 127

Acronyms

APL	Average path length
BEC	Bose-Einstein condensate
CC	Clustering coefficient
CS	Coherent state
CV	Continuous variable
DJC	Double Jaynes–Cummings model
DTC	Double Tavis–Cummings model
ESD	Entanglement sudden death
EIT	Electromagnetically induced transparency
HQ	Hybrid quantum
IBM Q	IBM quantum computing platform
IDC	Intensity-dependent coupling
IPR	Inverse participation ratio
LD	Link density
MLE	Maximal Lyapunov exponent
PACS	Photon-added coherent state
PCC	Pearson correlation coefficient
QASM	Quantum assembly language
SLE	Subsystem linear entropy
SVNE	Subsystem von Neumann entropy
TCS	Truncated coherent state
TEI	Tomographic entanglement indicator

Chapter 1
Introduction

Over the years, investigations on quantum states and observables have shed light on novel effects, some of which have no classical counterparts. Effects such as quadrature and spin squeezing of quantum states [1–3] have their origins in the Heisenberg uncertainty relation, and hence have no analogs in classical physics. Some others, such as entanglement (where the state of the full system cannot be considered as a factored product of the states of the subsystems), can also be realized with classical electromagnetic waves. The entanglement between the polarization and orbital angular momentum modes of light is an example of the latter [4]. Another interesting effect comprises wave packet revival phenomena in quantum systems during temporal evolution [5]. Under specific conditions, a generic wave packet corresponding to an initial state $|\psi_0\rangle$ may return to its original state, apart from an overall phase, at integer multiples of a revival time $T_{\rm rev}$. Correspondingly, the fidelity $|\langle\psi(0)|\,\psi(t)\rangle|^2$ becomes equal to unity at $t = T_{\rm rev}$. Under real experimental conditions near-revivals are more common, when the fidelity comes close to unity, but does not become equal to it. Further, under certain conditions, at instants $T_{\rm rev}/m$ ($m = 2, 3, \ldots$), m copies with a smaller amplitude than the original wave packet could appear. These correspond to the m-subpacket fractional revivals.

The origins of the revival phenomena that occur during temporal evolution of a wave packet can be traced back to interference between its constituent basis states. A parallel can be drawn with the classical Talbot effect when images, which comprise one or more copies of a diffraction grating through which light is passed, can be captured at specific distances from the grating. In this case, the analog of the revival time is the Talbot distance. Squeezing, quantum entanglement and full and fractional revivals of quantum states are some examples of nonclassical effects. An ideal platform to examine the links between quantum and classical physics is provided by optics, where comparison between the behavior of an electromagnetic wave with that of photons sets the stage for identifying inherently quantum phenomena (see, for instance, [6]).

© The Author(s), under exclusive license to Springer Nature Switzerland AG 2022

S. Lakshmibala and V. Balakrishnan, *Nonclassical Effects and Dynamics of Quantum Observables*, SpringerBriefs in Physics,
https://doi.org/10.1007/978-3-031-19414-6_1

Several approaches to understanding the passage from the quantum to the classical domain have been attempted in the literature. One of the aims in such investigations is to identify and understand genuinely quantum phenomena with no parallels or counterparts in classical situations, and also to evaluate how far the tools of classical physics can be applied to understanding quantum effects, and where they fail. Since classical dynamics is defined in the phase space of observables for both conservative and dissipative systems, and symmetries and invariance principles which guide classical evolution are defined in this phase space, the canonical structure of Hamilton's equations may naturally be expected to leave trails in the semiclassical and quantum domains as well. There is a sizeable body of literature in this regard, starting from the pioneering works on the invariance principles in semiclassical physics [7–9]. In a sense, a contrasting approach to this is available in the form of investigations on wave packets using the WKB method which is concerned with the eikonal representation of wave functions in configuration space alone, leading to situations in which the position wave function diverges, but the momentum space wave function does not. In a seminal report [10], the author discusses wave packet propagation, attempting to maintain position and momentum on an equal footing and extensively showcasing the corresponding transformation properties.

A somewhat oversimplified starting point for studying the dynamics is to approximate the Hamiltonian governing the temporal evolution of the system by a quadratic form in the neighborhood of the wave packet. The effect of cubic and higher order terms in the Hamiltonian on the dynamics of the quantum wave packet, leading to change of shape as it evolves, can be investigated through the dynamics of judiciously chosen observables. This exercise can be carried out using the Ehrenfest connection.

Consider a particle of mass m and linear momentum $\mathbf{p}$ (magnitude p) moving in one dimension, subject to the potential $V(x)$. The Hamiltonian is given by $p^2/2m + V(x)$. The Ehrenfest relations are

$$d\langle x\rangle/dt = \langle p\rangle/m \tag{1.1}$$

and

$$d\langle p\rangle/dt = -\langle dV(x)/dx\rangle. \tag{1.2}$$

In the special case of a quadratic Hamiltonian, $\langle dV(x)/dx\rangle$ is equal to $dV(\langle x\rangle)/dx$, and the corresponding expectation values follow classical motion. Approximating the Hamiltonian by its quadratic form is a technique used sometimes to track the semiclassical evolution of wave packets. For generic Hamiltonians, the contribution from higher moments of x and p are very revealing. The dynamical equations for the squares of x, p and their cross terms are given by

$$d\langle x^2\rangle/dt = (1/m)\langle xp + px\rangle, \tag{1.3}$$

$$d\langle xp\rangle/dt = d\langle px\rangle/dt = \langle p^2\rangle/m + \langle xF(x)\rangle, \tag{1.4}$$

and

$$d\langle p^2\rangle/dt = \langle pF(x) + F(x)p\rangle, \tag{1.5}$$

where $F(x) = -dV/dx$. The role played by these second and other higher moments, particularly in the context of the revival phenomena, will be illustrated in Chap. 2. It suffices now to draw attention to the fact that, in order to identify the state of a quantum system completely, we need to measure an infinite number of moments of all the relevant observables. In practice, however, one carefully selects a finite set of observables, whose expectation values in the instantaneous state of the system as it evolves in time are measured. State reconstruction from this subset can be a formidable task, especially in the case of Hilbert spaces of high dimensions, with multipartite subsystems interacting nonlinearly with each other. A recurring theme in this work will be about estimating nonclassical effects from raw experimental data available in the form of tomograms. An important feature is that, while a Gaussian wave packet continues to be Gaussian when evolving under a quadratic Hamiltonian, this does not hold good for other forms of the wave packet. Perhaps one of the finest demonstrations of this feature is through the temporal behavior of different states of quantized light. Quantum optics provides an ideal framework for examining the time evolution of various states of the radiation field, and for investigating nonclassical effects captured through experimentally relevant observables such as the mean photon number of the field.

In the chapters that follow, we will explore a variety of nonclassical effects using different states of light. As a starting point, by drawing a parallel between the quadratic forms of the Hamiltonian for a linear harmonic oscillator and the electromagnetic field energy density for a single-mode radiation field, the mathematical framework of the oscillator is carried over to the description of the radiation field. The standard oscillator ladder operators are interpreted as the photon annihilation operator a and its hermitian conjugate, the photon creation operator $a^\dagger$. The photon number operator is $\mathsf{N} = a^\dagger a$, and its eigenstates comprise the set of n-photon states $\{|n\rangle\}$, where $n = 0, 1, 2, \ldots$. Useful lessons can then be learnt by examining the manner in which various states of light evolve in time. For ready reference, we first list the states of the radiation field that we shall use for this purpose in this work, in different contexts. The simplest such state, which also sets the reference level for coherence and the bound below which squeezing occurs, is the standard normalized oscillator coherent state (CS) $|\alpha\rangle$, where $\alpha \in \mathbb{C}$. This CS is an eigenstate of a, satisfying $a|\alpha\rangle = \alpha|\alpha\rangle$. In the photon number basis $\{|n\rangle\}$, we have

$$|\alpha\rangle = e^{-|\alpha|^2/2} \sum_{n=0}^{\infty} \frac{\alpha^n}{\sqrt{n!}} |n\rangle. \tag{1.6}$$

$|\alpha\rangle$ is a 'minimum uncertainty state'—in units such that $\hbar = 1$, the uncertainty product in the field quadratures x and p is $(\Delta x)(\Delta p) = \frac{1}{2}$ for a CS. Further, it sets the reference level for squeezing, since if a state has variance (in a field quadrature) less

than that of the CS (i.e., less than $\frac{1}{2}$), it is said to be squeezed in that quadrature. $|\alpha\rangle$ is also a displaced vacuum state, i.e., $|\alpha\rangle = \mathcal{D}(\alpha)\,|0\rangle$, where $|0\rangle$ is the vacuum or zero-photon state and

$$\mathcal{D}(\alpha) = e^{(\alpha a^\dagger - \alpha^* a)} \tag{1.7}$$

is the Weyl–Heisenberg displacement operator.

The concept of a coherent state has been generalized in many ways (see, for instance, [11, 12]). There are many differences, however, in the manner in which this idea is extended by different authors. For instance, in the formalism given by Perolomov, an arbitrary Lie group acts on any fixed reference state to create displaced states, although some states turn out to be more preferable as reference states than others. Gilmore and his collaborators have worked with a finite dimensional dynamical symmetry group which acts on an extremal state that can be annihilated by a maximal subset of the algebra of the dynamical symmetry group. Generalization of the CS in other directions include the nonlinear coherent states of direct interest to us, such as the photon-added coherent states (PACS) [13]. The m-photon-added coherent state (m-PACS) $|\alpha, m\rangle$, where $m = 1, 2, \ldots$, is obtained by normalizing the state $a^{\dagger m}|\alpha\rangle$ to unity. Then $\{|\alpha, m\rangle\}$ is a family of states whose departure from coherence is precisely quantifiable. It is evident that if we set $m = 0$, we recover the standard CS $|\alpha\rangle$. In the photon number basis, we have

$$|\alpha,\ m\rangle = \frac{e^{-\frac{1}{2}|\alpha|^2}}{\sqrt{m! L_m(-|\alpha|^2)}} \sum_{n=m}^{\infty} \alpha^{n-m} \frac{\sqrt{n!}}{(n-m)!} |n\rangle, \tag{1.8}$$

where $L_m(-|\alpha|^2)$ is the Laguerre polynomial of order m. The m-PACS is a *nonlinear* coherent state, being an eigenstate of the operator $[1 - m(1 + a^\dagger a)^{-1}]\,a$ [14]. The one-photon-added CS $|\alpha, 1\rangle$ has been identified in the laboratory through state tomography methods [15], and it may be expected that m-PACS ($m > 1$) will also be realized in practice with advances in experimental technology.

Two interesting and useful superpositions of $|\alpha\rangle$ are the even and odd coherent states [16]. The normalized even coherent state (ECS) and the normalized odd coherent state (OCS) are expressed in terms of $|\alpha\rangle$ as

$$\text{ECS} = \mathcal{N}_{\alpha_+}\,(|\alpha\rangle + |-\alpha\rangle) \tag{1.9}$$

and

$$\text{OCS} = \mathcal{N}_{\alpha_-}\,(|\alpha\rangle - |-\alpha\rangle)\,, \tag{1.10}$$

where $\mathcal{N}_{\alpha_\pm} = [2(1 \pm e^{-2|\alpha|^2})]^{-1/2}$. In the photon number basis, we have

$$\mathrm{ECS} = \mathcal{N}_{\alpha_+}\, e^{-\frac{1}{2}|\alpha|^2} \sum_{n=0}^{\infty} \left[1 + (-1)^n\right] \frac{\alpha^n}{\sqrt{n!}}\, |n\rangle \tag{1.11}$$

and

$$\mathrm{OCS} = \mathcal{N}_{\alpha_-}\, e^{-\frac{1}{2}|\alpha|^2} \sum_{n=0}^{\infty} \left[1 - (-1)^n\right] \frac{\alpha^n}{\sqrt{n!}}\, |n\rangle. \tag{1.12}$$

The Yurke–Stoler state (YSS) [17], defined as

$$\mathrm{YSS} = \frac{1}{\sqrt{2}} \left(|\alpha\rangle + i\, |-\alpha\rangle\right), \tag{1.13}$$

is given in the photon number basis by

$$\mathrm{YSS} = \frac{1}{\sqrt{2}} e^{-\frac{1}{2}|\alpha|^2} \sum_{n=0}^{\infty} \left[1 + i(-1)^n\right] \frac{\alpha^n}{\sqrt{n!}}\, |n\rangle. \tag{1.14}$$

Since $|\alpha\rangle$ and $|-\alpha\rangle$ are macroscopically distinguishable for large $|\alpha|$, superpositions of these two states are referred to as Schrödinger cat states (or just cat states). The squeezing and dissipation properties of these cat states have been discussed extensively in [18]. In particular, these authors have established that fourth-order squeezing (i.e., squeezing of combinations of the fourth moments of the photon creation and destruction operators) can be generated by damping. Addition of one or more photons to cat states produces 'kitten states' which display interesting effects. For instance, it has been shown [19] by examining the relevant Wigner functions that there is increased visibility of sub-Planck structures after photon addition to YSS, and that the photon number statistics changes from Poissonian to sub-Poissonian, suggesting that such photon addition could be potentially useful in quantum noise reduction.

There is a very interesting link between the ECS and the squeezed vacuum state (SQV) (which is also expandable as a superposition of even photon number states), and similarly between the OCS and the Yuen state, the latter being expandable as a superposition of odd photon number states. This has been discussed further in Ref. [20], along with the general procedure to create such 'Janus-faced' partner states in the context of multiphoton processes. We discuss this in some detail below. The Fock states $|0\rangle$ and $|1\rangle$, respectively, are ground states in the 'even' Hilbert space spanned by $\{|2n\rangle\}$ and the 'odd' Hilbert space spanned by $\{|2n+1\rangle\}$. The relevant operators for two-photon processes are a^2 and its Hermitian conjugate $a^{\dagger 2}$. Defining $I_a = (1 + a^\dagger a)^{-1}$, let

$$G_0^\dagger = \frac{1}{2} a^{\dagger 2} I_a,\ G_1^\dagger = \frac{1}{2} a^\dagger I_a a^\dagger. \tag{1.15}$$

Then the commutation relations of interest here are $[a^2, {G_0}^\dagger] = 1$ in the even subspace and $[a^2, {G_1}^\dagger] = 1$ in the odd subspace. Eigenstates of a^2, namely,

$$|f\rangle_0 = e^{f\, G_0^\dagger}|0\rangle \tag{1.16}$$

and

$$|f\rangle_1 = e^{f\, G_1^\dagger}|1\rangle \tag{1.17}$$

where $f \in \mathbb{C}$, can be identified after a change of variables ($f = \alpha^2$) as the ECS and the OCS, respectively. Similarly, the eigenstates of G_0 and G_1 (the hermitian conjugates of $G_0^\dagger$ and $G_1^\dagger$) are

$$|g\rangle_0 = e^{g\, a^{\dagger 2}}|0\rangle \tag{1.18}$$

and

$$|g\rangle_1 = e^{g\, a^{\dagger 2}}|1\rangle \tag{1.19}$$

respectively, where $g \in \mathbb{C}$. Now consider the SQV $|\xi\rangle_0$ given by $\mathcal{S}(\xi)|0\rangle$, where

$$\mathcal{S}(\xi) = \exp\left[\frac{1}{2}(\xi^* a^2 - \xi a^{\dagger^2})\right] \ (\xi \in \mathbb{C}) \tag{1.20}$$

is the standard single-mode squeezing operator. Writing $\xi = r\, e^{i\theta}$, we can derive the expansion

$$|\xi\rangle_0 = (\cosh r)^{-1/2} \sum_{n=0}^{\infty} \left(-\frac{1}{2} e^{i\theta} \tanh r\right)^n \frac{\sqrt{2n!}}{n!} |2n\rangle. \tag{1.21}$$

Similarly, consider the Yuen state $|\xi\rangle_1$ given by [21, 22]

$$|\xi\rangle_1 = \mathcal{S}(\xi)|1\rangle = (\cosh r)^{-3/2} \sum_{n=0}^{\infty} \left(\frac{1}{2} e^{-i\theta} \tanh r\right)^n \frac{\sqrt{(2n+1)!}}{n!} |2n+1\rangle. \tag{1.22}$$

With the substitution $g = -\frac{1}{2}(\xi/|\xi|) \tanh|\xi|$, the states $|g\rangle_0$ and $|g\rangle_1$ defined above can be identified as the SQV and the Yuen state, respectively.

The concept of Janus-faced partners also extends to the multi-mode sector. Consider the two-mode case. Let a ($a^\dagger$) and b ($b^\dagger$), respectively, denote the destruction (creation) operators of the modes A and B. The Caves–Schumaker state [23, 24] or the two-mode squeezed vacuum state $|\xi; 0\rangle_{AB}$ ($\xi \in \mathbb{C}$) is defined as $|\xi; 0\rangle_{AB} = \mathcal{S}_{AB}(\xi)|0;\ 0\rangle$, where $|0; 0\rangle \equiv |0\rangle_A \otimes |0\rangle_B$ and

$$\mathcal{S}_{AB}(\xi) = \exp\left[\frac{1}{2}(\xi a^\dagger b^\dagger - \xi^* a\, b)\right] \tag{1.23}$$

is the two-mode squeezing operator. In the photon number basis, we have

$$|\xi;\ 0\rangle_{AB} = \frac{1}{\cosh r}\sum_{n=0}^{\infty}(-e^{i\theta}\tanh r)^n |n;\ n\rangle, \tag{1.24}$$

where ξ is equal to $re^{i\theta}$.

Another two-mode state of relevance to us is the pair coherent state $|\eta; q\rangle_{AB}$, defined [25] as the simultaneous eigenstate of the pair annihilation operator ab with eigenvalue η ($\eta \in \mathbb{C}$) and the number difference operator $(a^\dagger a - b^\dagger b)$ with eigenvalues $q = \ldots, -2, -1, 0, 1, 2, \ldots$. Equivalently, in the photon number basis,

$$|\eta; q\rangle_{AB} = \left[|\eta|^q / I_q(2|\eta|)\right]^{\frac{1}{2}} \sum_{n=0}^{\infty} \frac{\eta^n}{\sqrt{n!(n+q)!}}\, |n+q; n\rangle, \tag{1.25}$$

where $I_q(2|\eta|) = \sum_{n=0}^{\infty} |\eta|^{2n+q}/[n!(n+q)!]$ is the modified Bessel function of order q. In this two-mode case, the relevant commutator is given by $[ab,\ G^\dagger] = 1$, where

$$G^\dagger = a^\dagger b^\dagger (I_a + I_b) \tag{1.26}$$

and $I_a = (1 + a^\dagger a)^{-1}$, $I_b = (1 + b^\dagger b)^{-1}$. The state

$$\exp(f' G^\dagger)|0, 0\rangle \quad (f' \in \mathbb{C}),$$

after an appropriate change of variables, can be identified as the pair coherent state corresponding to $q = 0$. Its 'Janus-faced' partner is the state

$$\exp(g' a^\dagger b^\dagger)|0, 0\rangle, \quad (g' \in \mathbb{C})$$

which, after a suitable change of variables, can be identified as the Caves–Schumaker or two-mode squeezed vacuum state. The Caves–Schumaker state and the pair coherent state have been shown to be the short-time and steady-state solutions, respectively, of an appropriate master equation [26]. Subsequently, in Ref. [27], a general master equation has been obtained for all 'Janus-faced' pairs such that one of the states is the short-time solution and the other is the steady-state solution.

The binomial state of the radiation field, as the name implies, yields a binomial counting probability distribution. The single-mode version of this state [28] interpolates between the photon number state and the CS. This state displays rich nonclassical properties such as squeezing for certain parameter ranges, sub-Poissonian statistics, and so on. In Chap. 5, we will consider the two-mode generalization of the binomial state given by

$$|\psi_{\text{bin}}\rangle = 2^{-N/2} \sum_{n=0}^{N} \binom{N}{n}^{1/2} |N-n; n\rangle, \tag{1.27}$$

where N is a non-negative integer and $|N-n; n\rangle \equiv |N-n\rangle \otimes |n\rangle$.

For completeness we mention in passing the isospectral coherent state [29], although we will not consider this state in this work. It differs from the CS in the following sense: Consider the operator

$$a_1 = a^\dagger (1 + a^\dagger a)^{-\frac{1}{2}}\, a\, (1 + a^\dagger a)^{-\frac{1}{2}}\, a. \tag{1.28}$$

It is easily checked that $[a_1,\ a_1^\dagger] = 1 - |0\rangle\langle 0|$, so that a_1 annihilates both $|0\rangle$ and $|1\rangle$. In the restricted Hilbert space with basis $\{|n_1\rangle\}$ $(n_1 = 1,\ 2, \ldots)$, we can therefore define the isospectral coherent state

$$|\zeta, 1\rangle = \exp\left(\zeta a_1^\dagger - \zeta^* a_1\right)|1\rangle, \quad \zeta \in \mathbb{C}. \tag{1.29}$$

This state is an eigenstate of a_1, with eigenvalue ζ. This idea can further be extended to other restricted Hilbert spaces with bases $\{|n_i\rangle\}$ $(n_i = i, i+1, \ldots)$.

Exploiting the parallels in the mathematical structure of the simple harmonic oscillator, on the one hand, and the states of the radiation field of a single frequency and polarization propagating in free space, on the other, along with the Ehrenfest relations, we can map the time evolution of the field to the oscillator dynamics. This enables an instructive pedagogical comparison to be made of the behavior of classical and nonclassical states of radiation [30]. The time evolution of any initial state of the radiation field as it propagates in free space is given by the time evolution of the corresponding initial wave function (of a particle) in position space as governed by the oscillator Hamiltonian, i.e., in a parabolic potential. Thus, for instance, for the CS $|\alpha\rangle$, the dynamics of the wave function $\alpha(x)$ governed by the oscillator Hamiltonian is all that needs to be examined. Fixing the mean energy (the horizontal line in Fig. 1.1),[1] we can track the positional probability density and also the expectation value of the position operator x (equivalently, the field quadrature in the context of radiation), denoted by the dot, in time. Obviously, the Gaussian form of the probability density does not change in time and $\langle x(t)\rangle$ does not cross the parabolic wall; the farthest point reached is the classical turning point, as is clear from the inset. However, a similar procedure carried out for an initial 1-PACS (Fig. 1.2) and for an initial squeezed state (Fig. 1.3) reveal that the positional probability density for each of these nonclassical states changes its shape in time, and $\langle x(t)\rangle$ does not reach the classical turning point at any instant.

A more substantial understanding of the extent of nonclassicality of a state requires detailed state reconstruction. The starting point for any reconstruction program is a tomogram, i.e., a set of histograms of experimentally measured quantities. A siz-

[1] For figures similar to Figs. 1.1, 1.2 and 1.3, but for different values of the parameters, see "*Ehrenfest's Theorem and Nonclassical States of Light 2. Dynamics of Nonclassical States of Light*", George et al. [30].

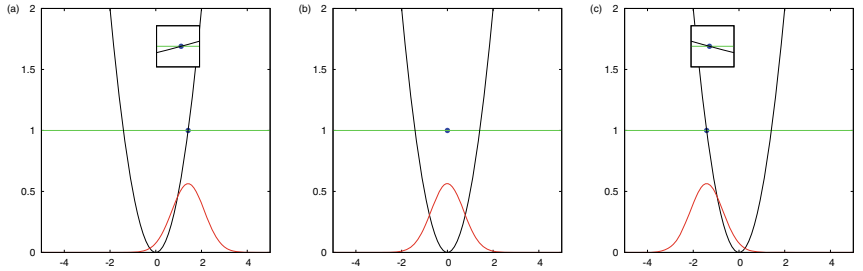

Fig. 1.1 Periodic motion of the positional probability density (red curve) and $\langle x(t)\rangle$ (blue dot) for a coherent state $|\alpha\rangle$ with $|\alpha| = 1$. **a** $t = 0$; **b** $t = \pi/(2\omega)$; **c** $t = \pi/\omega$, $\omega = 1$. The parabolic curve in black is the oscillator potential. The horizontal green line indicates the mean energy of the state. The probability density profile does not change shape during the time evolution, but merely translates back and forth. For similar figures with $|\alpha| = 1$ and $\omega = 0.005$, see [30]

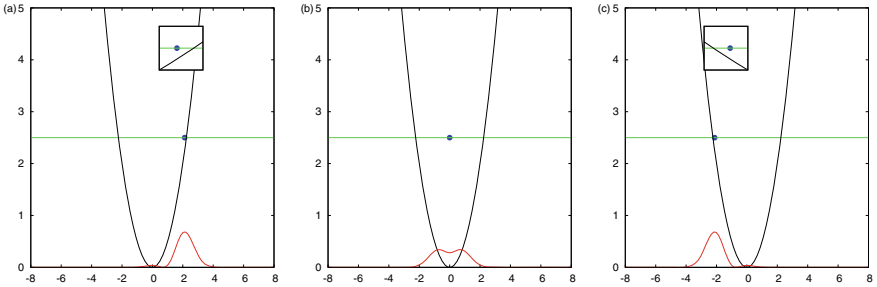

Fig. 1.2 Periodic motion of the positional probability density (red curve) and $\langle x(t)\rangle$ (blue dot) for a 1-photon-added coherent state $|\alpha, 1\rangle$ with $|\alpha| = 1$. **a** $t = 0$; **b** $t = \pi/(2\omega)$; **c** $t = \pi/\omega$, $\omega = 1$. The horizontal green line indicates the mean energy E of the state. Note that (i) the probability density profile changes shape during the time evolution, and (ii) $\langle x(t)\rangle$ does not reach the classical turning points at any time. For similar figures with $|\alpha| = 1$ and $\omega = 0.005$, see [30]

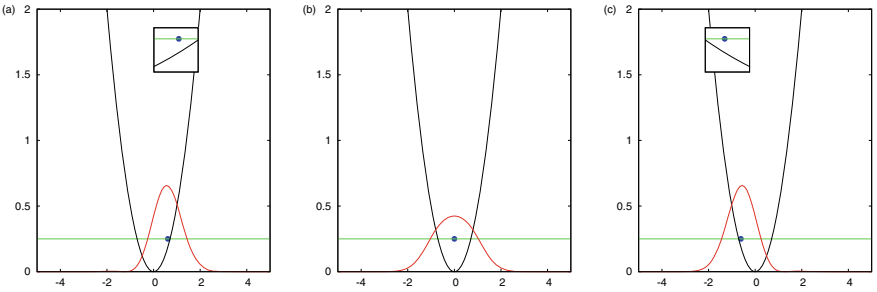

Fig. 1.3 Periodic motion of the positional probability density (red curve) and $\langle x(t)\rangle$ (blue dot) for a squeezed state $(\sqrt{3}|0\rangle + |1\rangle)/2$. **a** $t = 0$; **b** $t = \pi/(2\omega)$; **c** $t = \pi/\omega$, $\omega = 1$. Note that the probability density profile is unimodal, but changes shape during the time evolution. As in the case of the PACS, $\langle x(t)\rangle$ does not reach the classical turning points at any time. For similar figures with $\omega = 0.005$, see [30]

able body of literature exists on tomography, both classical and quantum (see, for instance, [31]). In the quantum case which is of relevance to us, these histograms are typically obtained by repeated preparation of the quantum state of interest, and measurement of an appropriately chosen quorum of observables in this state. Various schemes have been proposed to reconstruct the density matrix or the Wigner function from the tomogram (see, for instance, [32] and references therein). In the case of optical tomograms, state reconstruction relies usually on homodyne tomographic methods, and pattern function techniques [33–35]. In practice, the task of distinguishing between even a CS and thermal light for low photon numbers is not easy, since a large number of measurements needs to be made in order to distinguish between the correlation properties of different states of light. More recently, it has been demonstrated that neural network techniques together with targeted machine learning programs help in dramatically reducing the number of such measurements [36, 37]. However, much more work needs to be done, exploiting novel techniques, before identification of arbitrary superposed states of light is achieved, particularly in the low-photon-number regime.

Over and above merely distinguishing between two or more states, quantum state tomography aims at understanding all the properties of the unknown state. Whether the starting point is optical tomograms or spin/qubit tomograms, this becomes a formidable task with an increase in the dimensions of the Hilbert spaces, as the number of density matrix elements to be computed correspondingly increases significantly [38]. This is true of the radiation field, which is the archetypal example of a continuous-variable (CV) system, hybrid quantum (HQ) systems involving field-atom interactions [39], and systems where an array of qubits couple to each other [40]. Inevitable losses due to decoherence and dissipation effects provide additional challenges to state reconstruction since the data is inherently noisy, and the computational complexity could be very high [41, 42]. It follows from the discussion above that clever identification of the necessary data for reconstruction, the optimal number of measurements, the novel techniques to be employed to characterize different states, and so on, pose diverse challenges, and a universal prescription for state tomography is hard to come by.

Against this backdrop, the question of how much knowledge about the state can be gleaned directly from a tomogram, circumventing elaborate state reconstruction, becomes both relevant and important. For illustrative purposes, we consider optical tomograms. In the case of a single mode of light, the tomogram is a collection of probability distributions $\omega(X_\theta, \theta)$ corresponding to the rotated quadrature operators $\mathbb{X}_\theta = (ae^{-i\theta} + a^\dagger e^{i\theta})/\sqrt{2}$. Here, a and $a^\dagger$ are the photon destruction and creation operators satisfying $[a, a^\dagger] = 1$, and

$$\mathbb{X}_\theta |X_\theta, \theta\rangle = X_\theta |X_\theta, \theta\rangle. \tag{1.30}$$

The tomogram $\omega(X_\theta, \theta)$ is defined as the diagonal matrix element

$$\omega(X_\theta, \theta) = \langle X_\theta, \theta | \rho | X_\theta, \theta\rangle, \tag{1.31}$$

where ρ is the density matrix. For every value of θ, the corresponding set of states $\{|X_\theta, \theta\rangle\}$ forms a complete basis, and we have the normalization

$$\int_{-\infty}^{\infty} \mathrm{d}X_\theta \, \omega(X_\theta, \theta) = 1. \tag{1.32}$$

The tomogram is plotted with X_θ on the horizontal axis and θ on the vertical axis. It is clear that the tomogram represents a probability density for each value of θ.

A straightforward extension of the definition of the single-mode tomogram can be used to define multimode (multipartite) tomograms. The tomogram for the full system, as well as the marginal distributions corresponding to specific subsystems of the multipartite system (obtained by tracing out the other subsystems from the full tomogram), satisfy the requirements of classical probability densities [34]. This is in contrast to the generic Wigner function, which is negative in certain regions of the quadrature plane, and which is related through a Radon transform to the tomogram. It is to be emphasized that all information about the quantum state is encoded in the tomogram. Thus, working with tomograms alone allows for the possibility of formulating the theory of optical states and their dynamics within a 'classical' framework, applying the rules of classical probability theory. In this spirit 'symplectic tomography' techniques have been employed to describe quantum dynamics, by recasting quantum dynamical equations in terms of dynamical equations for appropriate positive marginal distributions (see, for instance, [43, 44]).

Some related important tasks that need to be addressed when working with probability densities instead of quasiprobability distributions are the following: the assessment of the extent to which nonclassical effects such as quantum wave packet revivals can be identified directly from tomograms; the scope for quantification of the squeezing properties of an unknown quantum state from the corresponding tomogram; and examining the efficacy of entanglement indicators whose genesis lies in 'distances' between classical probability distributions, and which can be calculated directly from the tomogram. Since spin systems also display squeezing and entanglement, the exercise would be incomplete unless it is carried out on those systems as well. A substantial part of the present work addresses these tasks. This is especially relevant for HQ platforms where light interacts with one or more atoms, each with a finite number of energy levels. In contrast to the field quadratures for which there is a complete basis for every θ among a continuous infinity of values, and from which a judicious choice of a finite set of values must be made, the Pauli basis comes in handy in obtaining spin tomograms. It is evident, however, that the complexity of the tomogram and the basis set in which measurements need to be performed in spin arrays also increases with the dimension of the associated linear vector space. We will investigate both optical and spin tomograms, using 'real' data obtained from NMR experiments in the latter case [45].

Without invoking tomography, quantum wave packet revivals have been investigated in the literature in diverse examples, such as systems subject to different one-dimensional potentials, integrable two-dimensional billiard systems, systems with

more than one quantum number, and specific atomic, molecular and optical systems [5]. Techniques such as the analysis of the 'complex' phase space with trajectories that evolve in complex time have been employed in order to follow the trajectory of the wave packet of strongly anharmonic systems from the classical period to the revival time [46]. The qualitative signatures of revivals and fractional revivals of an initial CS propagating in a Kerr-like medium (with a Hamiltonian proportional to $a^{\dagger 2}a^2$) have been identified through optical tomograms at different instants of time during the dynamical evolution, in Ref. [47].

Another interesting line of thought which we will take forward relies on the parallels between near-revivals in quantum systems and Poincaré recurrences in coarse-grained classical dynamical systems. The idea is to consider the dynamics in the effective 'phase space' of quantum expectation values of observables pertaining to the system of interest. Periodic returns of the wave packet to its original form would correspond to closed orbits in this phase space, and near-revivals to quasiperiodic orbits. These near-revivals are the analogs of Poincaré recurrences in classical systems. In the latter case, investigations have been conducted on recurrence time statistics of trajectories to cells in a coarse-grained classical phase space, both in discrete and continuous time. For instance, recurrence-time statistics for chaotic dynamics in discrete time maps [48] has been investigated in detail. A comparison has been made between recurrence time statistics in deterministic and stochastic systems in continuous time [49]. Exact analytical expressions for the distribution of successive recurrences in generic 1-dimensional maps exhibiting intermittent chaos have been obtained, and it has been established that multiple recurrences are not statistically independent events in this case [50]. In an investigation aimed at drawing parallels between classical recurrences and revivals of quantum states, it has been shown that the revival times of a CS in a deformed, adiabatically and cyclically varying oscillator Hamiltonian are exactly those of Poincaré recurrences for a rotation map [51]. An exercise to ascertain the extent to which results on recurrence time statistics from classical dynamical systems theory hold in the quantum case, in which the space of expectation values has been coarse-grained into cells, has been conducted in the context of both CV and HQ systems involving field-atom interactions. Further, the entire machinery of time-series and network analysis, which is ubiquitous in classical dynamics, has been employed in the quantum context in order to understand the role played by the initial state and by parameter values in determining the ergodicity properties of observables such as the mean photon number. Long time series of quadrature observables and the mean photon number, when analyzed using recurrence plots, could in principle shed light on how departure from coherence of the initial state of a radiation field present in a CV or HQ system can affect the ergodicity properties of the observable. We will elaborate upon such a detailed time series analysis using numerically generated data in Chap. 7.

We now move on to draw attention to the usefulness of tomograms in determining the squeezing properties of an unknown quantum state. In the context of the radiation field, a detailed prescription has been provided [52] for obtaining the normally ordered moments of combinations of a and $a^\dagger$ directly from tomograms. This pro-

cedure can be used in a straightforward manner to quantify the extent of quadrature squeezing. We draw attention to the fact that detailed investigations on other types of squeezing properties, such as entropic squeezing, have been reported in the literature (for a recent review, see [53]). Defining entropy in this context using ideas from information theory, entropic uncertainty relations, entropic squeezing, and generalizations of these uncertainty relations to non-canonically conjugate variables have been obtained for various states of light.

The importance of correlations in formulating such relations has also been investigated in some detail. In particular, we note that information itself plays a vital role in defining entanglement and entanglement measures. For instance, inspired by the classical Shannon entropy, a standard measure of entanglement, namely, the subsystem von Neumann entropy (SVNE) or the entropy of entanglement, has been defined. For a bipartite system with subsystems A and B (with subsystem label $i = A, B$), we shall denote the SVNE by ξ_{SVNE}. It is defined in terms of the subsystem density matrix ρ_i as

$$\xi_{\text{SVNE}} = -\text{Tr}\,(\rho_i \log_2 \rho_i). \tag{1.33}$$

For a pure state of the full system with density matrix ρ_{AB}, the numerical value of the SVNE in Eq. (1.33) is the same for $i = A$ and $i = B$. In those situations where we compute the von Neumann entropy of a composite system AB, we shall refer to it as $\xi_{\text{SVNE}}^{(AB)}$, given by $-\text{Tr}\,(\rho_{AB} \log_2 \rho_{AB})$. (In the literature both the natural logarithm and the logarithm to base 2 are used in the definition of the SVNE. In this work we will use both notations, and indicate in each context which notation has been adopted.)

Not surprisingly, there exist interesting links between entropy and entropic uncertainty relations, on the one hand, and certain entanglement indicators, on the other. The entropic uncertainty principle has been extended to include the effect of quantum entanglement [54]. An experimental investigation of how entanglement affects the entropic uncertainty principle has been carried out using an optical set-up in [55], and it has been shown that the uncertainty is close to zero for quasi-maximal entanglement. More recently, it has been proposed [56], that the Wehrl entropy which is associated with the Husimi distribution is ideally suited to quantify entanglement in CV systems. The corresponding mutual information could be used to define a good entanglement witness for pure state bipartite entanglement. In Chap. 3, we demonstrate how both entropic and quadrature squeezing properties of an optical state can be obtained solely from the corresponding tomogram.

Again, spin squeezing in an effectively bipartite system comprising interacting spins, can be estimated directly from spin tomograms [45]. The amount of spin squeezing can be related to the Fisher information, and to entanglement. Spin squeezing is a powerful tool in quantum metrology and non-demolition measurements. For a review see, for instance, [3]. It turns out that not only signatures of wave packet revivals and quantifiers of squeezing, but also estimators of the extent of bipartite entanglement, can be obtained directly from appropriate tomograms [57]. These quantifiers are not measures, and their absolute values need not necessarily agree in magnitude with the standard measures of entanglement. However, they are useful in

understanding the manner in which the entanglement changes with variations in the parameters of the system considered, and also with time, as the system evolves unitarily. This approach is particularly useful when the Hilbert space dimensionality is large, and state reconstruction from the tomogram becomes a formidable task. While this will be a primary aspect under scrutiny in this work, we point out that there exists an extensive literature, spanning a considerable number of years, on entanglement and its importance as a resource for applications in spin and CV systems for quantum information processing [58]. While it is beyond the scope and emphasis of the present work to elaborate upon the substantial effort put into understanding the very many aspects of quantum entanglement and its applications, we point out an interesting feature here, which helps us appreciate the role of the dimensionality of the Hilbert space. Even in a bipartite system in which the Hilbert space of each of the two subsystems is infinite dimensional, the set of separable states is nowhere dense, in contrast to the finite dimensional case, where there is always an open neighborhood of separable states. The set of states with infinite entropy of entanglement in the former case is trace-norm dense in state space, implying that in any neighborhood of every product state there is an arbitrarily strongly entangled state (see, for instance, [59, 60]). A detailed investigation of this feature reveals that it is possible to generate, in principle, an infinite amount of entanglement (as estimated with an appropriate quantifier) in an infinitely short time in CV systems under specific conditions. An instance in optics is that of an initial CS subject to unitary time evolution which incorporates Kerr nonlinearity and a 50% beam-splitter operation. Further, in this set up, paradoxically, only a finite degree of entanglement can be generated over longer times [61].

Considerable research has been carried out on entanglement transfer in HQ systems in recent years, as they offer tremendous scope for multitasking simultaneously, without compromising significantly on efficiency. The recognition that under specific conditions entanglement sudden death (ESD) [62–65] and subsequent sudden birth can happen in many HQ systems, has led to several investigations on the effect of various interactions. Examples include a beamsplitter acting on the field subsystem, and the dipole-dipole and Ising interactions on qubit subsystems of a generic HQ system. The objective is to control the extent of entanglement and to use it as a resource for quantum technologies. A variety of HQ systems have been proposed within the framework of circuit QED, using mechanical oscillators, surface acoustic waves, magnonics and couplings between superconducting circuits and spins (for a review, see [66, 67]). Further, since ESD happens on finite time scales which are much shorter than the decoherence time of the qubits subsystem due to noise, judicious application of NOT operations during decoherence on one or more qubit subsystems have been shown to hasten, delay or even prevent ESD from occurring [68].

Since our focus in later chapters will be on bipartite entanglement and its ramifications such as the collapse of entanglement to a constant non-zero value, we first recall some of the standard quantifiers that are used in this context, denoting the two subsystems by the index $i = A, B$. Apart from the entanglement entropy SVNE defined earlier, one often uses in quantum optics the subsystem linear entropy (SLE)

to quantify the extent of entanglement, in view of the relation between the Wigner function $W(x, p)$ and the square of the density matrix ρ given by

$$\int W^2(x, p)dx\, dp = (1/2\pi\hbar)\,\mathrm{Tr}\,(\rho^2). \tag{1.34}$$

The quantum generalization of the classical Tsallis entropy is given by

$$T_q(\rho) = \left[1 - \mathrm{Tr}(\rho^q)\right]/(q-1). \tag{1.35}$$

For the subsystem density matrix ρ_i, and in the case $q = 2$, this reduces precisely to the subsystem linear entropy

$$\xi_{\mathrm{SLE}} = [1 - \mathrm{Tr}(\rho_i^2)]. \tag{1.36}$$

Wherever necessary in this work, when investigating entanglement at avoided energy level crossings, and entanglement in CV and HQ systems during dynamical evolution, we will use the SVNE and SLE as reference levels for comparison with tomographic entanglement indicators.

A versatile entanglement monotone used in the context of qubit systems, for both pure and mixed states, is concurrence [69]. It is helpful to outline the procedure for defining concurrence in the context of bipartite entanglement, using the notation in the reference cited above. The definition uses the spin-flip operation which can be performed on an arbitrary number of qubits. In the case of two-qubit mixed states with both the density matrix ρ and the Pauli matrix σ_y (which is essential for the spin-flip operation) written in a chosen basis, we define

$$\widetilde{\rho} = (\sigma_y \otimes \sigma_y)\,\rho^*\,(\sigma_y \otimes \sigma_y), \tag{1.37}$$

where ρ^* is the complex conjugate of the density matrix in the chosen basis. Consider the eigenvalues of the Hermitian matrix $R = \left(\sqrt{\rho}\,\widetilde{\rho}\,\sqrt{\rho}\right)^{1/2}$ arranged in decreasing order and denoted by λ_i, $i = 1, 2, 3, 4$. The concurrence in this case is defined as

$$C(\rho) = \max\{0, \lambda_1, -\lambda_2, -\lambda_3, -\lambda_4\}. \tag{1.38}$$

Now consider

$$\mathcal{E}\,(C(\rho)) = h\left(\frac{1}{2}[1 + \sqrt{1 - C^2}]\right), \tag{1.39}$$

where the function $h(x)$ is given by

$$h(x) = -x\log_2 x - (1-x)\log_2(1-x). \tag{1.40}$$

(In the special case of a pure state $|\psi\rangle$, it can be shown that $\mathcal{E}\left(C(\psi)\right)$ is the SVNE for the state where $C(\psi)$ is the concurrence of the pure state $|\psi\rangle$.) Since $\mathcal{E}\left(C(\psi)\right)$ increases monotonically from 0 to 1 as the concurrence increases from 0 to 1, the latter is itself taken to be the entanglement estimator. In Chap. 6, we briefly review the phenomenon of ESD in a specific HQ system, where concurrence has been used to understand entanglement dynamics.

The negativity is another useful and readily computable entanglement monotone [70]. It is defined as

$$N(\rho_{AB}) = \frac{1}{2}\sum_i \left(|\mathcal{L}_i| - \mathcal{L}_i\right). \tag{1.41}$$

Here $\{\mathcal{L}_i\}$ is the set of eigenvalues of $\rho_{AB}^{T_A}$, the partial transpose of ρ_{AB} with respect to the subsystem A. (Equivalently, the partial transpose $\rho_{AB}^{T_B}$ may be used.) We will analyze the efficacy of entanglement indicators obtained solely from tomograms using experimental data from different NMR experiments in Chap. 6. For this purpose we will use negativity as the reference for comparison. We mention in passing that a related monotone is the logarithmic negativity [71], often used in the literature.

In examining data from certain NMR experiments, we will also use the discord as the reference entanglement indicator when assessing the performance of the indicators obtained solely from tomograms. The quantum discord $D(B:A)$ between the two subsystems A and B of the composite system AB is another standard measure of quantum correlations, and is defined as follows. If ρ_{AB} is the density matrix of AB, its von Neumann entropy is $\xi_{\rm SVNE}^{(AB)} = -{\rm Tr}[\,\rho_{AB}\log_2\rho_{AB}]$. If projective measurements are carried out on A, the discord $D(B:A)$ is defined as

$$D(B:A) = \xi_{\rm SVNE}^{(A)} - \xi_{\rm SVNE}^{(AB)} + \min_{\{\mathcal{O}_i^A\}}\left\{-\sum_j p_{ij}^A {\rm Tr}\left(\varrho_{ij}\log_2\varrho_{ij}\right)\right\}, \tag{1.42}$$

where $\{\mathcal{O}_i^A\}$ is a set of subsystem observables pertaining to A. Here,

$$p_{ij}^A = {\rm Tr}[(\Pi_{ij}^A \otimes \mathbb{I}_B)\rho_{AB}] \tag{1.43}$$

and

$$\varrho_{ij} = \frac{{\rm Tr}_A[(\Pi_{ij}^A \otimes \mathbb{I}_B)\rho_{AB}(\Pi_{ij}^A \otimes \mathbb{I}_B)]}{p_{ij}^A}, \tag{1.44}$$

where $\{\Pi_{ij}^A\}$ is the set of projection operators corresponding to $\mathcal{O}_i^A$ and $\mathbb{I}_B$ denotes the identity operator in B. $D(A:B)$ is similarly defined when projective measurements are carried out on B. In general, $D(A:B) \neq D(B:A)$. The set of entanglement quantifiers we have defined above suffices for our purposes.

The plan of the rest of this work is as follows: In Chap. 2, we discuss the revival phenomena, showcasing the importance of various moments of the quadrature observables, and pointing out how, under certain conditions, full and fractional revivals leave signatures in CV tomograms. In Chap. 3, the procedure for extracting quadrature and entropic squeezing properties from optical tomograms is discussed. Chapter 4 deals with entanglement indicators that can be obtained directly from tomograms. The connection between entanglement indicators and spin squeezing is outlined in this chapter. The indicators are specifically assessed in the context of avoided energy level crossings in both CV and HQ systems. In Chap. 5, we examine the efficacy of tomographic bipartite entanglement indicators in CV systems during temporal evolution. Their sensitivity to various initial states of the system is assessed. In Chap. 6, we examine the performance of the entanglement indicators in HQ systems. These tomographic indicators are computed in specific instances using the IBM quantum platform, by working with circuits that are equivalent to the HQ system concerned. Further, we discuss the usefulness of the entanglement indicators obtained from spin tomograms using experimental data from a set of NMR experiments. The experiments were performed by our collaborators in the NMR-QIP group at IISER Pune, India. In Chap. 7, we consider various models of atom-field interactions with the objective of exploring how well the tools of time series and network analysis fare in explaining the ergodicity properties of quantum observables. This also gives us a glimpse of the situations where results from classical ergodicity theory may fail in the quantum context. This chapter is followed by a brief set of concluding remarks pointing out some possible directions for future work in bridging the classical-quantum divide.

The list of references given here is by no means exhaustive, as there exists a vast literature on the topics mentioned in this chapter. We have cited a representative set of pertinent references in order to put in perspective the central theme of this work.

References

1. V.V. Dodonov, J. Opt. B Quant. Semiclass. Opt. **4**, R1 (2002)
2. V.V. Dodonov, V.I. Man'ko (eds.), *Theory of Nonclassical States of Light* (Taylor and Francis, London, 2003)
3. J. Ma, X. Wang, C.P. Sun, F. Nori, Phys. Rep. **509**, 89 (2011)
4. E. Toninelli, B. Ndagano, A. Vallés, B. Sephton, I. Nape, A. Ambrosio, F. Capasso, M.J. Padgett, A. Forbes, Adv. Opt. Photon. **11**, 67 (2019)
5. R.W. Robinett, Phys. Rep. **392**, 1 (2004)
6. J.H. Eberly, X.-F. Qian, A. Al Qasimi, H. Ali, M.A. Alonso, R. Gutiérrez-Cuevas, B.J. Little, J.C. Howell, T. Malhotra, A.N. Vamivakas, Phys. Scr. **91**, 063003 (2016)
7. J.B. Keller, Ann. Phys. **4**, 180 (1958)
8. V.P. Maslov, *Théorie des Perturbations et Méthodes Asymptotiques* (Dunod, Paris, 1972)
9. V.P. Maslov, M.V. Fedoriuk, *Semi-classical Approximation in Quantum Mechanics* (D. Reidel, Dordrecht, 1981)
10. R.G. Littlejohn, Phys. Rep. **138**, 193 (1986)
11. W.-M. Zang, D.H. Feng, R. Gilmore, Rev. Mod. Phys. **62**, 867 (1990)
12. A. Perelomov, *Generalized Coherent States and Their Applications* (Springer, Berlin, 1986)

13. G.S. Agarwal, K. Tara, Phys. Rev. A **43**, 492 (1991)
14. S. Sivakumar, J. Phys. A Math. Gen. **32**, 3441 (1999)
15. A. Zavatta, S. Viciani, M. Bellini, Science **306**, 660 (2004)
16. V.V. Dodonov, I.A. Malkin, V.I. Man'ko, Physica **72**, 597 (1974)
17. B. Yurke, D. Stoler, Phys. Rev. Lett. **57**, 13 (1986)
18. V. BuŽek, A. Vidiella-Barranco, P.L. Knight, Phys. Rev. A **45**, 6570 (1992)
19. Arman, G. Tyagi, P.K. Panigrahi, Opt. Lett. **46**, 1177 (2021)
20. P. Shanta, S. Chaturvedi, V. Srinivasan, G.S. Agarwal, C.L. Mehta, Phys. Rev. Lett. **72**, 1447 (1994)
21. H.P. Yuen, Phys. Rev. A **13**, 2226 (1976)
22. C.L. Mehta, A.K. Roy, G.M. Saxena, Phys. Rev. A **46**, 1565 (1992)
23. C.M. Caves, B.L. Schumaker, Phys. Rev. A **31**, 3068 (1985)
24. B.L. Schumaker, C.M. Caves, Phys. Rev. A **31**, 3093 (1985)
25. G.S. Agarwal, J. Opt. Soc. Am. B **5**, 1940 (1988)
26. G.S. Agarwal, Phys. Rev. Lett. **57**, 827 (1986)
27. K.V.S.S. Chaitanya, V. Srinivasan, J. Phys. A Math. Theor. **43**, 485205 (2010)
28. D. Stoler, B.E.A. Saleh, M.C. Teich, Opt. Acta **32**, 345 (1985)
29. S. Seshadri, V. Balakrishnan, S. Lakshmibala, J. Math. Phys. **39**, 838 (1998)
30. L.T. George, C. Sudheesh, S. Lakshmibala, V. Balakrishnan, Resonance **17**(2), 192–211 (2012). https://doi.org/10.1007/s12045-012-0018-7
31. M.A. Man'ko, V.I. Man'ko, G. Marmo, A. Simoni, F. Ventriglia, Nuovo Cim. **36**, 163 (2013)
32. Y.S. Teo, *Introduction to Quantum State Estimation* (World-Scientific, Singapore, 2016)
33. A.I. Lvovsky, M.G. Raymer, Rev. Mod. Phys. **81**, 299 (2009)
34. K. Vogel, H. Risken, Phys. Rev. A **40**, 2847 (1989)
35. S. Olivares, A. Allevi, G. Caiazzo, M.G.A. Paris, M. Bondani, New J. Phys. **21**, 103045 (2019)
36. C. You, M.A. Quiroz-Juárez, A. Lambert, N. Bhusal, C. Dong, A. Perez-Leija, A. Javaid, R.d.J. León-Montiel, O.S. Magaña-Loaiza, Appl. Phys. Rev. **7**, 021404 (2020)
37. S. Ahmed, C.S. Muñoz, F. Nori, A.F. Kockum, Phys. Rev. Res. **3**, 033278 (2021)
38. C.M. Caves, I.H. Deutsch, R. Blume-Kohout, J. Opt. B Quant. Semiclass. Opt. **6**, S801 (2004)
39. S. Ashhab, F. Nori, Phys. Rev. A **81**, 042311 (2010)
40. Y.-X. Liu, L.F. Wei, F. Nori, Phys. Rev. B **72**, 014547 (2005)
41. S. Deléglise, I. Dotsenko, C. Sayrin, J. Bernu, M. Brune, J.M. Raimond, S. Haroche, Nature **455**, 510 (2008)
42. J.A. Smolin, J.M. Gambetta, G. Smith, Phys. Rev. Lett. **108**, 070502 (2012)
43. S. Mancini, V.I. Man'ko, P. Tombesi, Phys. Lett. A **213**, 1 (1996)
44. S. Mancini, V.I. Man'ko, P. Tombesi, Found. Phys. **27**, 801 (1997)
45. B. Sharmila, V.R. Krithika, S. Pal, T.S. Mahesh, S. Lakshmibala, V. Balakrishnan, J. Chem. Phys. **156**, 154102 (2022)
46. W. Koch, D.J. Tannor, Chem. Phys. Lett. **683**, 306 (2017)
47. M. Rohith, C. Sudheesh, Phys. Rev. A **92**, 053828 (2015)
48. V. Balakrishnan, G. Nicolis, C. Nicolis, J. Stat. Phys. **86**, 191 (1997)
49. V. Balakrishnan, G. Nicolis, C. Nicolis, Phys. Rev. E **61**, 2490 (2000)
50. V. Balakrishnan, G. Nicolis, C. Nicolis, Stoch. Dyn. **1**, 345 (2001)
51. S. Seshadri, S. Lakshmibala, V. Balakrishnan, Phys. Lett. A **256**, 15 (1999)
52. A. Wunsche, Phys. Rev. A **54**, 5291 (1996)
53. A. Hertz, N.J. Cerf, J. Phys. A Math. Theor. **52**, 173001 (2019)
54. M. Berta, M. Christandl, R. Colbeck, J.M. Renes, R. Renner, Nat. Phys. **6**, 659 (2010)
55. C.-F. Li, J.-S. Xu, X.-Y. Xu, K. Li, G.-C. Guo, Nat. Phys. **7**, 752 (2011)
56. S. Floerchinger, T. Haas, H. Müller-Groeling, Phys. Rev. A **103**, 062222 (2021)
57. B. Sharmila, S. Lakshmibala, V. Balakrishnan, J. Phys. B At. Mol. Opt. **53**, 245502 (2020)
58. R. Horodecki, P. Horodecki, M. Horodecki, K. Horodecki, Rev. Mod. Phys. **81**, 865 (2009)
59. R. Clifton, H. Halvorson, Phys. Rev. A **61**, 012108 (1999)
60. J. Eisert, C. Simon, M.B. Plenio, J. Phys. A Math. Gen. **35**, 3911 (2002)
61. S.J. van Enk, Phys. Rev. Lett. **91**, 017902 (2003)

62. J.H. Eberly, T. Yu, Science **316**, 555 (2007)
63. M.P. Almeida, F. de Melo, M. Hor-Meyll, A. Salles, S.P. Walborn, P.H.S. Ribeiro, L. Davidovich, Science **316**, 579 (2007)
64. J. Laurat, K.S. Choi, H. Deng, C.W. Chou, H.J. Kimble, Phys. Rev. Lett. **99**, 180504 (2007)
65. T. Yu, J. Eberly, Science **323**, 598 (2009)
66. A.A. Clerk, K.W. Lehnert, P. Bertet, J.R. Petta, Y. Nakamura, Nat. Phys. **16**, 257 (2020)
67. A. Blais, A.L. Grimsmo, S.M. Girvin, A. Wallraff, Rev. Mod. Phys. **93**, 025005 (2021)
68. A. Singh, S. Pradyumna, A.R.P. Rau, U. Sinha, J. Opt. Soc. Am. B **34**, 681 (2017)
69. W.K. Wooters, Phys. Rev. Lett. **80**, 2245 (1998)
70. G. Vidal, R.F. Werner, Phys. Rev. A **65**, 032314 (2002)
71. M.B. Plenio, Phys. Rev. Lett. **95**, 090503 (2005)

Chapter 2
Revivals, Fractional Revivals and Tomograms

2.1 Introduction

From the earliest days of quantum mechanics, there has been considerable interest in the similarities as well as the analogies between the temporal evolution of classical systems and the dynamics of quantum systems. As mentioned in Chap. 1, the Talbot effect in classical physics and wave packet revival phenomena in quantum systems are two physical effects which are often compared in this context. In the former, when light falls on a diffraction grating, images of the grating ('Talbot copies') appear at multiples of a fundamental spatial period along the direction of propagation of light. At specific distances between two successive Talbot images, there appear superimposed copies of an integer number of images of the grating. This is the fractional Talbot effect [1]. These images create exquisite patterns called Talbot carpets with interesting fractal properties (see, for instance, [2]). Although the Talbot effect was observed originally with electromagnetic waves, subsequent studies have shown that the effect can be captured with matter waves as well [3].

The quantum mechanical analog of the foregoing is the phenomenon of wave packet revivals. In the case of electromagnetic waves, the effect is as follows. While propagating through a suitable 'nonlinear' atomic medium, a wave packet of light can recover its original form (apart from an overall phase) at specific instants of time. These instants occur periodically at integer multiples of a fundamental revival time $T_{\rm rev}$. Further, an integer number of copies of the original wave packet could form, with overlap between them, at certain instants between two successive revivals, heralding a fractional revival. (For an extensive review and references, see [4].) In practice however, revivals cannot be sustained beyond a few multiples of $T_{\rm rev}$, because of the decoherence effects that arise due to system-environment interactions. In the Talbot set-up, the effects observed arise from the interference between light passing through the different slits of the grating. In wave packet revival phenomena, the wave packet is comprised of basis states which interfere with each other. In both cases, the mathematical origins can be traced to the properties of Gauss sums, which are

© The Author(s), under exclusive license to Springer Nature Switzerland AG 2022

S. Lakshmibala and V. Balakrishnan, *Nonclassical Effects and Dynamics of Quantum Observables*, SpringerBriefs in Physics,
https://doi.org/10.1007/978-3-031-19414-6_2

known to appear in unanticipated ways in a variety of physical contexts. In the sequel, we will demonstrate the role of Gauss sums in the context of wave packet revival phenomena.

Although there is an extensive literature on investigations of the Talbot effect, many interesting aspects remain open, such as its potential application to quantum information processing and computation. The classical Talbot effect has been shown [5] to be useful in decomposing a number into its prime factors. A temporal version of the Talbot effect exploits the fact that the frequency components of a classical electric field composed of suitably-shaped femtosecond pulses of light can be determined using Gauss sums. This version of the Talbot effect also has been used to factor numbers [6]. Another variant is the quantum Talbot effect (see, for instance, [7, 8]), where the source comprises single photons or entangled photon pairs produced through parametric down-conversion. More recently, the quantum Talbot effect has been interpreted in a novel manner as a logic gate operation, and it has been established that the Talbot carpets in this context can be used for quantum information processing [9]. It appears that there are many more unexplored features of Talbot effects with the potential for application in information processing and computation.

In the quantum mechanical context, additional features that have been examined are the occurrence of fractional revivals in systems with two time scales [10], and the appearance of super-revivals of the states of various systems including Rydberg wave packets [11]. Super-revivals occur when there are higher-order nonlinearities in the system, and certain relations between the various frequencies in the governing Hamiltonian are satisfied. The phenomenon has also been observed experimentally. The new features in the dynamics of expectation values brought in by super-revivals provide material for further investigations.

Revival phenomena have also been examined extensively in the case of coherent states subject to a host of one-dimensional potentials [12]. It has been shown that wave packet revivals (or at least near-revivals) may be expected to occur in effectively single-mode systems, but are not guaranteed to occur in bipartite or multipartite systems. General conclusions cannot be drawn about the conditions under which revivals can happen in the latter, as their occurrence depends on details such as the initial state considered, the interplay between the various frequencies in the Hamiltonian, and the range of values of system parameters.

Over the years, the term ‘revivals’ has been used with somewhat different connotations in different contexts. In general, however, a revival corresponds to the return of an attribute of the system to its original value. The instants of revival are separated by periods of collapse during which the system observables settle down to nearly constant values. One of the earliest instances of revival phenomena in bipartite systems reported in the literature was in the Jaynes–Cummings model of a two-level atom interacting with light in an initially coherent state. Here, revivals and collapses are associated with the dynamics of the atomic inversion (the difference in the probability of the atom being in the excited and ground states, respectively), which displays rapid oscillations (revivals) separated by collapse to a constant value over an interval of time. In this case, the finite number of levels of the atom is primarily responsible for the phenomenon. Although the Jaynes–Cummings model (a fully quantum

mechanical model of atom-field interaction) in the rotating wave approximation is an exactly solvable, seemingly simple model, it reveals an important lesson on the return of a bipartite initial state to a form close to it, at a subsequent instant. It is well known that, even if the bipartite state is initially a direct product of the atom state and a coherent field state, it inevitably becomes entangled during dynamical evolution. One might then expect the state of the system to be close to its initial separable form during the revival phase of the atomic inversion. It has however been established, first using approximations [13] and subsequently through exact analytical calculations [14] that the state is closest to its original factored form at approximately the mid-point of the interval of collapse of the inversion. Moreover, the system attains this state through unitary evolution, independent of the specific values of parameters and the intensity of the initial coherent state. It has therefore been referred to as an 'attractor state'. Here again it would be of interest to probe further into a possible parallel between the flow to an attractor in a dissipative classical dynamical system, on the one hand, and the evolution, albeit unitary, of states to such an 'attractor' state in a quantum system, on the other.

2.2 Basic Mechanism of Wave Packet Revivals

The manner in which full and fractional revivals arise as a consequence of certain relationships between different frequency parameters in the Hamiltonian is as follows [15, 16].

Consider a system whose Hamiltonian H has a discrete spectrum $\{E_n\}$ and corresponding eigenstates $\{|\phi_n\rangle\}$, where $E_n > E_{n'}$ if $n > n'$. Suppose the initial state $|\psi(0)\rangle$ of the system is a superposition of the basis states $\{|\phi_n\rangle\}$ that is sharply peaked about some value n_0 of the quantum number n. (The typical experimental situation involves wave packets of Rydberg states, so that $n_0 \gg 1$.) We may expand E_n as

$$E_n = E_{n_0} + (n - n_0)E_{n_0}^{'} + \frac{1}{2}(n - n_0)^2 E_{n_0}^{''} + \cdots . \tag{2.1}$$

We shall see that terms up to the quadratic in $(n - n_0)$ suffice to produce revivals and fractional revivals. Shifting n by n_0 for notational simplicity, we have the quadratic form

$$E_n = C_0 + C_1 n + C_2 n^2, \tag{2.2}$$

where the coefficients C_i depend on the parameters in H. Without loss of generality we consider $C_1, C_2 > 0$. The unitary time-evolution operator has the spectral decomposition

$$U(t) = e^{-iHt/\hbar} = \sum_{n}^{\infty} e^{-i\,(C_0 + C_1 n + C_2 n^2)t/\hbar} |\phi_n\rangle\langle\phi_n\,|. \tag{2.3}$$

For a full revival to occur at time t, $U(t)$ must reduce to the unit operator (apart from a possible overall phase factor), i.e., $(C_1 n + C_2 n^2)t$ must be an integer multiple of $2\pi\hbar$ for every n in the sum. There are four possible cases, of which three are very simple ones. If $C_1 \neq 0,\ C_2 = 0$ (linear spectrum), the initial state revives periodically with a period $2\pi\hbar/C_1$. If $C_1 = 0, C_2 \neq 0$, we again have periodicity with a period $2\pi\hbar/C_2$. If $C_1, C_2 \neq 0$ and C_1/C_2 is a rational number r/s, full revivals occur with a fundamental revival time $T_{\rm rev} = 2\pi\hbar s/C_2$. Finally, we have the generic case in which $C_1, C_2 \neq 0$, and C_1/C_2 is irrational. As the condition $(C_2 n^2 + C_1 n)t = 2\pi\hbar m$ (where m is an integer) cannot be satisfied for *all* n at any value of t, full revivals are no longer possible. However, at certain instants of time, the state could come arbitrarily close to the initial state, signaling a near-revival.

Between occurrences of full (or near) revivals, the wave packet breaks up into a finite sum of subsidiary packets at specific instants of time, if the spectrum is nonlinear, i.e., if $C_2 \neq 0$. These fractional revivals occur at instants $t = \pi\hbar r/(C_2 s)$ where r and s are mutually prime integers. It can be shown that at these instants U can be expressed as a finite sum of operators U_p, in each of which the phase factor multiplying the projection operator $|\phi_n\rangle\langle\phi_n|$ is linear in n. One finds [15]

$$U(\pi\hbar r/C_2 s) = \sum_{p=0}^{l-1} a_p^{(r,s)}\, U_p \tag{2.4}$$

where

$$a_p^{(r,s)} = (1/l) \sum_{k=0}^{l-1} e^{i\pi[(2kp/l)-(k^2 r/s)]}, \tag{2.5}$$

$$U_p = \sum_{n=0}^{\infty} e^{-in\theta_p}\, |\phi_n\rangle\langle\phi_n|, \quad \theta_p \ = \ \pi\ [(C_1 r/C_2 s) + (2p/l)]\,. \tag{2.6}$$

Here, $l = s/2$ if s is an integer multiple of 4, and $l = s$ in all other cases. The occurrence of fractional revivals can be traced back to this decomposition of U, which is crucially dependent on its periodicity properties at the instants of revivals and fractional revivals. These properties are rooted in Gauss sums, as we will now illustrate with a specific example.

To sum up: revivals and fractional revivals arise from the quadratic dependence of E_n on n. Super-revivals, if any, arise from terms higher than quadratic in n.

2.3 An Illustrative Example

As mentioned earlier, the revival of a wave packet during temporal evolution corresponds to the return of expectation values to their initial values. It is therefore worth examining the manner in which distinctive signatures of revivals and fractional

revivals are captured in the dynamics of relevant observables—see, for instance, Ref. [17] for a discussion of revivals in the case of the infinite square well. Our focus here is on the dynamics of radiation fields. We therefore consider a specific model of single-mode light propagating through a nonlinear (Kerr) medium. The effective Hamiltonian in terms of the photon destruction and creation operators a and $a^\dagger$ is [18]

$$H = \hbar\chi\, a^{\dagger 2} a^2 = \chi\, \mathsf{N}(\mathsf{N}-1). \tag{2.7}$$

$\mathsf{N} = a^\dagger a$ is the photon number operator, and χ (> 0) is essentially the third-order nonlinear susceptibility of the medium. We note that the eigenvalues of H in this case explicitly involve terms linear and quadratic in the eigenvalue of the number operator, without any approximation. This will help us highlight the role of Gauss sums in wave packet revival phenomena in the simplest possible way.

The Hamiltonian (2.7) is also relevant in a very different physical context, namely, in describing the dynamics of a Bose–Einstein condensate (BEC) in a potential well. In that case, a and $a^\dagger$ are boson annihilation and creation operators, and χ characterizes the energy needed to overcome the inter-atomic repulsion in adding an atom to the population of the potential well. Thus, the results obtained here are relevant for condensate wave functions as well. In a later section we will also discuss revival phenomena in the context of BECs, when considering the dynamics of the condensate trapped in a double-well potential, treating it as a bipartite system.

As the eigenvalues of N are integers ($= N$), the unitary time evolution operator corresponding to H, $U(t) = e^{-i\chi t \mathsf{N}(\mathsf{N}-1)}$, displays interesting periodicity properties. At the instants $t = \pi/(k\chi)$ where k is an integer,

$$U(\pi/k\chi) = e^{-i\pi \mathsf{N}(\mathsf{N}-1)/k}. \tag{2.8}$$

From the easily verified periodicity properties

$$e^{-i\pi(N+k)(N+k-1)/k} = e^{-i\pi N(N-1)/k} \quad (k = \text{odd integer}) \tag{2.9}$$

and

$$e^{-i\pi(N+k)^2/k} = e^{-i\pi N^2/k} \quad (k = \text{even integer}), \tag{2.10}$$

it follows that $U(\pi/k\chi)$ can be expanded in a Fourier series with $\{e^{-2\pi ij/k}\}$ as the basis, in the form

$$e^{-i\pi N(N-1)/k} = \sum_{j=0}^{k-1} f_j\, e^{-2\pi ijN/k} \quad (k \text{ odd}) \tag{2.11}$$

and

$$e^{-i\pi N^2/k} = \sum_{j=0}^{k-1} g_j\, e^{-2\pi ijN/k} \quad (k \text{ even}), \tag{2.12}$$

where the coefficients f_j and g_j are known. In order to be specific, let us take the initial state of the field to be the standard CS $|\alpha\rangle$ ($\alpha \in \mathbb{C}$) defined in Eq. (1.6). Using Eqs. (2.8), (2.11) and (2.12) and the property

$$e^{i\chi a^\dagger a}|\alpha\rangle = |\alpha e^{i\chi}\rangle, \tag{2.13}$$

we arrive at

$$|\psi(\pi/k\chi)\rangle = \begin{cases} \sum_{j=0}^{k-1} f_j |\alpha\, e^{-2\pi i j/k}\rangle & (k \text{ odd}) \\ \sum_{j=0}^{k-1} g_j |\alpha\, e^{i\pi/k}\, e^{-2\pi i j/k}\rangle & (k \text{ even}). \end{cases} \tag{2.14}$$

It is evident that the state revives for the first time at $t = T_{\rm rev} = \pi/\chi$, corresponding to $k = 1$, and subsequently at integer multiples of $T_{\rm rev}$. In between $t = 0$ and $t = T_{\rm rev}$, and in between two successive revivals, fractional revivals occur at instants $n\,T_{\rm rev} + T_{\rm rev}/k$, when the state of the system is a superposition of spatially distributed Gaussians with different amplitudes. Thus, for example, at the instant $\pi/(2\chi)$, the initial wave packet would have evolved to a superposition of $|i\alpha\rangle$ and $|-i\alpha\rangle$.

In general, the states at instants $t = \pi j/(k\chi)$, $1 \leqslant j \leqslant k-1$ for a given k, are superpositions of k wave packets.

2.4 Signatures of Revivals in Expectation Values of Observables

We now proceed to examine the manner in which fractional revivals are manifested in distinctive ways in the expectation values of the physical observables pertaining to a system, continuing to use for this purpose [19] the model considered in the preceding section: the evolution of an initial CS $|\alpha\rangle$ under the Hamiltonian (2.7). The relevant observables in this case are the field quadratures give by the operators

$$x = (a + a^\dagger)/\sqrt{2}, \quad p = -i(a - a^\dagger)/\sqrt{2}. \tag{2.15}$$

Clearly, the expectation values of x and p alone do not carry the complete information contained in the wave function. Higher moments of these observables and their combinations are needed to 'understand' the system completely. In practice, only the mean and a few higher moments of the relevant observables can be measured experimentally. But even this yields sufficient information about wave packet revivals. We define the c-number function

$$\alpha(t) = \langle\psi(t)|a|\psi(t)\rangle = \langle\alpha|e^{iHt/\hbar}\, a\, e^{-iHt/\hbar}|\alpha\rangle. \tag{2.16}$$

Since $a|\alpha\rangle = \alpha|\alpha\rangle$, we have $\alpha(0) \equiv \alpha$. Simplifying the right-hand side of Eq. (2.16), we get

$$\alpha(t) = \alpha\, e^{-|\alpha|^2(1-\cos 2\chi t)} \left\{\cos\left(|\alpha|^2 \sin(2\chi t)\right) - i \sin\left(|\alpha|^2 \sin(2\chi t)\right)\right\}. \quad (2.17)$$

As expected, $\alpha(t)$ is a periodic function of time with period π/χ. It is convenient to introduce the notation

$$\alpha = \alpha_1 + i\alpha_2 = (x_0 + ip_0)/\sqrt{2} \quad (2.18)$$

and

$$\nu = |\alpha|^2 = \frac{1}{2}(x_0^2 + p_0^2). \quad (2.19)$$

x_0 and p_0 represent the respective locations of the centers of the initial Gaussian wave packet corresponding to the CS $|\alpha\rangle$ in the x and p quadratures. The expectation values of x and p at any time t are then found to be

$$\langle x(t)\rangle = e^{-\nu(1-\cos 2\chi t)} \{x_0 \cos(\nu \sin 2\chi t) + p_0 \sin(\nu \sin 2\chi t)\}, \quad (2.20)$$

$$\langle p(t)\rangle = e^{-\nu(1-\cos 2\chi t)} \{-x_0 \sin(\nu \sin 2\chi t) + p_0 \cos(\nu \sin 2\chi t)\}. \quad (2.21)$$

We digress briefly to make an instructive comparison between the expressions in Eqs. (2.20) and (2.21), on the one hand, and the solutions for $x(t)$ and $p(t)$ *if* the system is a *classical* one, governed by the classical counterpart of the normal-ordered Hamiltonian, namely,

$$H_{\rm cl} = \frac{1}{4}(x^2 + p^2)^2. \quad (2.22)$$

Although the equations of motion corresponding to $H_{\rm cl}$ are nonlinear, it is evident that $(x^2 + p^2)$ is a constant of the motion, so that the phase trajectories are circles. The frequency of the periodic motion is, however, dependent on the initial conditions (equivalently, on the amplitude of the motion), being equal to $\nu = \frac{1}{2}(x_0^2 + p_0^2)$. As is well known, this is a characteristic feature of nonlinear oscillators. Turning to the quantum mechanical case, we note that the solutions for $\langle x(t)\rangle$ and $\langle p(t)\rangle$ are more complicated than the classical ones for $x(t)$ and $p(t)$ under $H_{\rm cl}$. This is a direct consequence of the quantum mechanical nature of the system, over and above the nonlinearity of H. Interestingly, the expressions for $\langle x(t)\rangle$ and $\langle p(t)\rangle$ can be formally cast in classical terms, as follows. We define the classical dynamical variables

$$X = \langle x\rangle\, e^{\nu(1-\cos 2\chi t)}, \quad P = \langle p\rangle\, e^{\nu(1-\cos 2\chi t)}, \quad (2.23)$$

and re-parametrize time by $\tau = \sin(2\chi t)$. These are clearly a non-canonical pair. The initial values of X and P remain x_0 and p_0, respectively. Equations (2.20) and

(2.21) can then be re-written in the suggestive form

$$\left.\begin{aligned} X &= x_0 \cos \nu\tau + p_0 \sin \nu\tau, \\ P &= -x_0 \sin \nu\tau + p_0 \cos \nu\tau. \end{aligned}\right\} \tag{2.24}$$

But these are the solutions to the system of equations

$$dX/d\tau = \nu P,\ dP/d\tau = -\nu X, \tag{2.25}$$

describing a nonlinear oscillator of frequency

$$\nu = \frac{1}{2}(x_0^2 + p_0^2), \tag{2.26}$$

in terms of the transformed variables (X, P) and the re-parametrized time τ. At the level of the first moments, therefore, the system is effectively a nonlinear oscillator after a suitable transformation of the relevant variables, together with a re-parametrization of the time.

As mentioned earlier, the higher moments of x and p also carry considerable information about the state of the system. These higher moments can be expressed as functions of time using the general result

$$\langle a^{\dagger r}\, a^{r+s}\rangle = \alpha^s\, \nu^r e^{-\nu\,(1-\cos\, 2s\chi t)}\, \exp\{-i\chi[s(s-1)+2rs]\,t - i\nu\, \sin\, 2s\chi t\}\,. \tag{2.27}$$

Here, r and s are non-negative integers. For the second moments, we obtain the expressions

$$\begin{aligned} 2\langle x^2(t)\rangle = 1 + x_0^2 + p_0^2 + e^{-\nu\,(1-\cos\, 4\chi t)}\, \big\{&(x_0^2 - p_0^2)\, \cos\,(2\chi t + \nu\, \sin\, 4\chi t) \\ &+ 2x_0 p_0\, \sin\,(2\chi t + \nu\, \sin\, 4\chi t)\big\}, \end{aligned} \tag{2.28}$$

$$\begin{aligned} 2\langle p^2(t)\rangle = 1 + x_0^2 + p_0^2 - e^{-\nu\,(1-\cos\, 4\chi t)}\, \big\{&(x_0^2 - p_0^2)\, \cos\,(2\chi t + \nu\, \sin\, 4\chi t) \\ &+ 2x_0 p_0\, \sin\,(2\chi t + \nu\, \sin\, 4\chi t)\big\}. \end{aligned} \tag{2.29}$$

The expressions for the third and fourth moments of x and p are relatively more complicated. From the foregoing, it is straightforward to compute the variance, skewness and excess of kurtosis (departure from Gaussianity) of the field quadratures.

Two points are worth mentioning. The higher the order of the moment, the more rapid is its variation in time, the highest frequency in the kth moment being $2k\chi$. In all the expectation values involved, the time variation depends crucially on $\exp\{-\nu(1 - \cos\, 2k\chi t)\}$ (where $k = 1, 2, \ldots$).

In contrast to the case when ν is sufficiently small, this exponential acts a strong damping term for large values of ν, *except when* $\cos\,(2m\chi t)$ *is near unity*. This happens precisely at revivals, i.e., when $t = n\pi/\chi$, an integer multiple of $T_{\rm rev}$. But

it also happens in the kth moment (and *not* in the lower moments) at the instants of fractional revival, namely, $t = (n + j/k)T_{\rm rev}$. Thus, by setting ν at a suitably large value, we can control the time variation of the moments such that they remain essentially static, but burst into rapid oscillations at specific instants of time before settling down to quiescence.

Owing to an obvious symmetry of H, the moments of x and p behave in a similar manner, especially if we start with the symmetric initial condition $x_0 = p_0$. For very small values ($\ll 1$) of x_0 and p_0 (i.e., of ν), the nonlinearity of H does not play a significant role, and the behavior of the system is akin to that of a simple oscillator. For larger values of ν, however, the dynamical behavior is very interesting. For sufficiently large values of ν, it is evident that, except for times close to integer multiples of $T_{\rm rev}$, $\langle x(t)\rangle$ and $\langle p(t)\rangle$ essentially remain static at the value zero. As the instant of revival is approached and crossed, the rest of the closed 'phase trajectory' in the ($\langle x(t)\rangle$, $\langle p(t)\rangle$ 'phase plane' is rapidly traversed and the representative point returns to the origin. Thus, these expectation values bear very clearly discernable signatures of revivals.

Fractional revivals, however, are not captured by the first moments $\langle x(t)\rangle$ and $\langle p(t)\rangle$. Higher moments are required for this purpose. For instance, the appearance of the fractional revival at $t = (n + \frac{1}{2})T_{\rm rev}$ between two successive revivals, corresponding to the initial wave packet reconstituting itself into two separate similar wave packets, is mirrored in the second moments. It is found that the uncertainty product $\Delta x\ \Delta p$ returns at every revival to its initial minimum value $\frac{1}{2}\hbar$, increasing in value between revivals. As before, for sufficiently large values of ν, the uncertainty product remains essentially static at the approximate value $(\frac{1}{2} + \nu)\hbar$ for most of the time, but changes extremely rapidly near revivals, and *also* near the fractional revivals occurring mid-way between revivals. During the latter, the uncertainty product drops to smaller values, although it does not reach the minimum value $\frac{1}{2}\hbar$. Thus, there is an important difference in the manner in which the uncertainty product behaves near revivals, as opposed to its behavior near fractional revivals.

The fractional revivals occurring at $t = (n + \frac{1}{3})T_{\rm rev}$ and $t = (n + \frac{2}{3})T_{\rm rev}$, at which the initial wave packet comprises a superposition of three separate wave packets, are detectable in the third moments of x and p, or, equivalently, in the skewness of each of these quadratures. Similarly, the fourth moments of x and p (i.e., the excess of kurtosis of each quadrature) capture the appearance of four superposed similar wave packets. Broadly speaking, for sufficiently large ν, all these quantities remain almost static near specific values most of the time, and vary rapidly near revivals and specific fractional revivals.

2.5 Effect of an Imperfectly Coherent Initial State

We have considered in the foregoing the revivals and fractional revivals of an initial coherent state as it evolves under the Kerr Hamiltonian. It is relevant to ask how these phenomena are affected or altered in the case of an initial field state that deviates

from perfect coherence in a manner that can be specified quantitatively and tuned accordingly. A suitable candidate in this case is the PACS, obtained by repeated addition of photons to a CS (Eq. 1.8). The analysis that follows is of more than merely theoretical interest.

The normalized m-PACS $|\alpha, m\rangle$ can be written as

$$|\alpha, m\rangle = \frac{(a^\dagger)^m|\alpha\rangle}{\sqrt{\langle\alpha|\, a^m a^{\dagger m}|\alpha\rangle}} = \frac{(a^\dagger)^m|\alpha\rangle}{\sqrt{m!\, L_m(-\nu)}}, \tag{2.30}$$

where m is a positive integer, $\nu = |\alpha|^2$ as before, and $L_m(-\nu)$ is the Laguerre polynomial of order m. As already stated in Chap. 1, for $m = 0$, we recover the CS $|\alpha\rangle$. With increase in m, the extent of departure of a PACS from ideal coherence becomes more pronounced. Further, unlike the CS, a PACS exhibits phase-squeezing and sub-Poissonian photon number statistics [20]. This implies that the standard deviation of the photon number operator N behaves asymptotically like $\langle\mathsf{N}\rangle^{\frac{1}{2}-\beta_m}$ $(0 < \beta_m < \frac{1}{2})$ rather than $\langle\mathsf{N}\rangle^{\frac{1}{2}}$, where β_m depends on m.

The dynamics of the moments of the self-adjoint operators x and p, as the initial PACS evolves under the Kerr-like Hamiltonian, may be understood as follows. It is convenient to use the notation

$$\langle x(t)\rangle_m = \langle\alpha,\ m|\, e^{iHt/\hbar}\, x\, e^{-iHt/\hbar}|\alpha,\ m\rangle, \tag{2.31}$$

with an analogous definition of $\langle p(t)\rangle_m$. As H is a function of N, its mean $\langle\mathsf{N}\rangle_m$ and all its higher moments, and the sub-Poissonian statistics of the photon number, remain unchanged in time. We recall that, at the level of the first moments, the dynamical equations in the case of an initial CS are those of a classical nonlinear oscillator, with a certain re-parametrization of time. In contrast, for $m > 0$, the dynamical behavior of $\langle x(t)\rangle_m$ and and $\langle p(t)\rangle_m$ is very different even for small values of m. The revival time itself does not change. However, between two successive revivals, the evolution of these observables is strikingly different from the case corresponding to $m = 0$. Thus, for instance, even a small departure from Poissonian number statistics of the initial field state, subsequently leads to different phase squeezing properties. The expectation values of the field quadratures in $|\alpha, m\rangle$ (i.e., their initial values) are found [21] to be given by

$$\langle x(0)\rangle_m = \frac{L_m^1(-\nu)}{L_m(-\nu)}\, x_0, \quad \langle p(0)\rangle_m = \frac{L_m^1(-\nu)}{L_m(-\nu)}\, p_0 \tag{2.32}$$

where $L_m^1(-\nu) = d\, L_{m+1}(-\nu)/d\nu$ is an associated Laguerre polynomial, $x_0 = \sqrt{2}\,\mathrm{Re}\,\alpha$, and $p_0 = \sqrt{2}\,\mathrm{Im}\,\alpha$. Analogous to the variables X and P defined in Eq. (2.23) in the case of the CS, we now define

$$\left.\begin{aligned} X_m(t) &= \langle x(t)\rangle_m\, e^{\nu\,(1-\cos 2\chi t)}, \\ P_m(t) &= \langle p(t)\rangle_m\, e^{\nu\,(1-\cos 2\chi t)}. \end{aligned}\right\} \tag{2.33}$$

(Thus X_0 and P_0 are just the quantities X and P of Eq. (2.23).) The explicit solutions for $X_m(t)$ and $P_m(t)$ can then be written compactly as

$$\left.\begin{aligned} X_m(t) &= x_0\,\mathrm{Re}\,z_m(t) + p_0\,\mathrm{Im}\,z_m(t), \\ P_m(t) &= p_0\,\mathrm{Re}\,z_m(t) - x_0\,\mathrm{Im}\,z_m(t), \end{aligned}\right\} \tag{2.34}$$

where

$$z_m(t) = \frac{L_m^1(-\nu\, e^{2i\chi t})}{L_m(-\nu)}\, e^{i\,(2m\chi t + \nu\,\sin 2\chi t)}. \tag{2.35}$$

A number of important differences can be seen between these results and those corresponding to $m = 0$. We first observe that the modulus $|z_m|$ varies with t, in contrast to $|z_0(t)| \equiv 1$. (Note further that $z_m(0) = L_m^1(-\nu)/L_m(-\nu) \neq 1$ when $m \neq 0$.) The time dependence of X_m and P_m involves the sines and cosines of the set of arguments $(2\chi\, lt + \nu\,\sin 2\chi t)$, where $l = m, \ldots, 2m$. Hence, apart from the presence of higher harmonics, the arguments have secular (linear) terms in t added to the original factor $\nu\,\sin 2\chi t$. This is an important difference, since we can no longer regard the time dependence as that of an effective nonlinear oscillator by means of a re-parametrization of the time, in contrast to the case of an initial field which has ideal coherence.

From Eqs. (2.33)–(2.35), explicit solutions for $\langle x(t)\rangle_m$ and $\langle p(t)\rangle_m$ can be obtained readily. Once again, the appearance of the overall factor $\exp\{-\nu\,(1 - \cos 2\chi t)\}$ in these solutions implies that, for sufficiently large values of ν, the expectation values remain essentially static around the value zero. Rapid variations only arise close to revivals. Clear signatures of revivals at integer multiples of T_{rev} are again manifest in the mean values of the field quadratures. With increase in the departure from coherence of the initial field state, $\langle x(t)\rangle_0$ shows increasingly rapid oscillatory behavior in the vicinity of revivals. The range over which the expectation value varies also increases for larger values of m.

Here also, fractional revivals occur between two successive revivals. These are at instants $(n + j/k)T_{\mathrm{rev}}$ where $k = 2, 3, \ldots$ and $j = 1, 2, \ldots, (k-1)$. For a given value of k, these fractional revivals are reflected in the rapid pulsed variation of the kth moments of x and p, and not in the lower moments. However, in the case of an initial PACS, an important observation is that even for relatively small values of $m > 0$, signatures of fractional revivals appear for values of ν that are not large. This is not true if the initial state is a CS.

A remark is in order here. Corresponding to an initial PACS, consider the fractional revival at $\frac{1}{2}T_{\mathrm{rev}}$. The overlap between the two spatially separated sub-packets that comprise the wave packet at this instant can be easily seen to decrease considerably with increase in the value of m. In principle, therefore the PACS is a better candidate for carrying out logic gate operations, treating the two sub-packets as constituting a single qubit, with labels $|0\rangle$ and $|1\rangle$, respectively [22]. This feature holds similarly at the instant $t = \frac{1}{4}T_{\mathrm{rev}}$, where the overlap between the four sub-packets is much smaller than in the case of an initial CS at this instant. With increase in the value of

m, the decrease in the overlap of the sub-packets is pronounced even for relatively small values of ν.

Likewise, the fractional revival at $\frac{1}{2}T_{\rm rev}$ manifests itself in the uncertainty product $\Delta x \Delta p$ through oscillations whose frequency and amplitude increase quite rapidly with increasing m. This effect gets blurred for larger values of the parameter ν, corresponding to which these oscillations are relatively insensitive to the value of m. Similar signatures of all kth order fractional revivals can be identified in the case of initial states $|\alpha, m\rangle$, even for relatively small values of ν. From the foregoing, it is evident that, in principle, the distinctive signatures of the wave packet revival phenomena manifested in the dynamics of appropriate observables can serve to identify departure from ideal coherence of the initial field state.

2.6 Revivals in Single-Mode Systems: A Tomographic Approach

When a single-mode radiation field propagates through a Kerr-like medium with Hamiltonian $H = \hbar\chi a^{\dagger 2}a^2$, the field tomogram corresponding to various instants of time could possibly provide picturesque signatures of full and fractional revivals. In what follows we address the problem of identifying the occurrence of the revival phenomena, through tomograms. We recall from Chap. 1 that the tomogram is a collection of probability distributions $\omega(X_\theta, \theta)$ corresponding to the rotated quadrature operators $\mathbb{X}_\theta = (ae^{-i\theta} + a^\dagger e^{i\theta})/\sqrt{2}$. For each θ,

$$\int_{-\infty}^{\infty} {\rm d}X_\theta\, \omega(X_\theta, \theta) = 1. \tag{2.36}$$

In the case of the single-mode system, the tomogram is given by

$$\omega(X_\theta, \theta) = \langle X_\theta, \theta|\, \rho |X_\theta, \theta\rangle. \tag{2.37}$$

Here ρ is the density matrix, and $\mathbb{X}_\theta|X_\theta, \theta\rangle = X_\theta|X_\theta, \theta\rangle$. It is evident that for a pure state $|\psi\rangle$, $\omega(X_\theta, \theta) = |\langle X_\theta, \theta|\psi\rangle|^2$. For numerical computations, the tomogram of a normalized pure state $|\psi\rangle$, which can be expanded in the photon number basis $\{|n\rangle\}$ as $\sum_{n=0}^{\infty} c_n|n\rangle$, is given by [23]

$$\omega(X_\theta, \theta) = \frac{e^{-X_\theta^2}}{\sqrt{\pi}} \left| \sum_{n=0}^{\infty} \frac{c_n e^{-in\theta}}{\sqrt{n!}2^{\frac{n}{2}}} H_n(X_\theta) \right|^2, \tag{2.38}$$

where $H_n(X_\theta)$ is the Hermite polynomial. In this expression, c_n alone is a function of time.

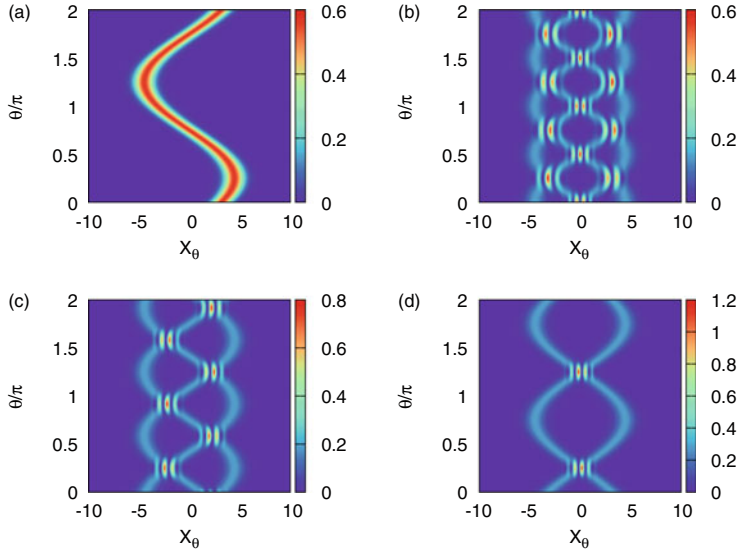

Fig. 2.1 Tomograms of an initial CS for a Kerr Hamiltonian with $\alpha = \sqrt{10}e^{i\pi/4}$ at instants **a** 0 and $T_{\rm rev}$, **b** $T_{\rm rev}/4$, **c** $T_{\rm rev}/3$, and **d** $T_{\rm rev}/2$. This was first reported for $\alpha = \sqrt{20}e^{i\pi/4}$ in [24]

For the system under consideration, it has been shown in Ref. [24] that, if the initial state of the field is a CS, the tomogram at the instants of fractional revivals is made of distinct strands. This is in contrast to blurred patterns comprising the tomogram at other generic instants. The number ℓ of distinct strands in the tomogram corresponds to an ℓ-subpacket fractional revival. ($\ell = 1$ for a full revival.) Figure 2.1a–d[1] depict the cases $\ell = 1, 4, 3$ and 2, respectively. We note that if ℓ is sufficiently large (e.g., $\ell \geqslant 5$ for $|\alpha| \approx 3$), quantum interference effects will blur the appearance of individual strands.

We next consider the cubic effective Hamiltonian

$$H' = \chi_2 \, a^{\dagger 3} a^3 = \chi_2 \, \mathsf{N}(\mathsf{N}-1)(\mathsf{N}-2), \tag{2.39}$$

where χ_2 is a constant with appropriate dimensions. It can be verified easily that an initial CS or 1-PACS under the Hamiltonian H' revives fully at instants $t = nT_{\rm rev}$ where $T_{\rm rev} = \pi/\chi_2$. Of direct interest to us is the qualitative appearance of tomograms at instants $T_{\rm rev}/\ell$ where ℓ is a positive integer. The optical tomograms for different values of ℓ are shown in Fig. 2.2a–i.[2] It is evident that the tomograms at $t = T_{\rm rev}$ and $T_{\rm rev}/3$ are similar to each other. This is in sharp contrast to the earlier case, where

[1] For figures similar to Fig. 2.1a–d, but for different values of the parameters, see *Visualizing revivals and fractional revivals in a Kerr medium using an optical tomogram*, Rohith and Sudheesh [24].

[2] Figures 2.2, 2.3, 2.4, 2.5, 2.6 and 2.7 are reproduced from *Signatures of nonclassical effects in optical tomograms*, Sharmila et al. [25] with permission from IOP Publishing.

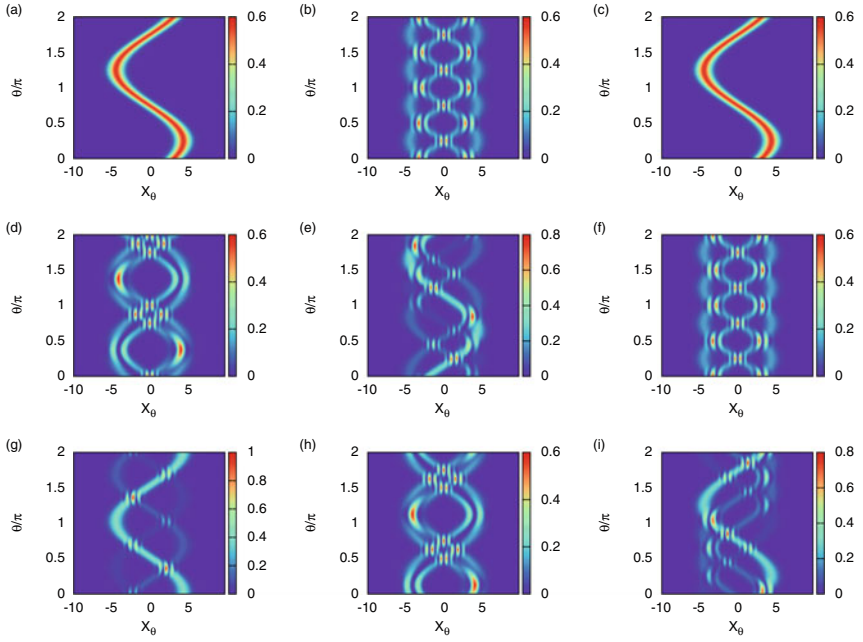

Fig. 2.2 Tomograms of an initial CS for a cubic Hamiltonian with $\alpha = \sqrt{10}e^{i\pi/4}$ at instants **a** 0 and $T_{\rm rev}$, **b** $T_{\rm rev}/2$, **c** $T_{\rm rev}/3$, **d** $T_{\rm rev}/4$, **e** $T_{\rm rev}/5$, **f** $T_{\rm rev}/6$, **g** $T_{\rm rev}/9$, **h** $T_{\rm rev}/12$, and **i** $T_{\rm rev}/15$. Figures are reproduced from [25]

the Kerr-like Hamiltonian governed the temporal evolution of the system (Eq. 2.7). The full revival at $T_{\rm rev}/3$ is a consequence of the fact that $n(n-1)(n-2)/3$ is an even integer for all integers n. Hence, corresponding to an initial state $|\psi(0)\rangle = \sum_{m=0}^{\infty} c_n|n\rangle$, the state at instant $T_{\rm rev}/3$ is

$$|\psi(T_{\rm rev}/3)\rangle = U(T_{\rm rev}/3)|\psi(0)\rangle = \sum_{n=0}^{\infty} e^{-i\pi n(n-1)(n-2)/3} c_n|n\rangle = |\psi(0)\rangle. \quad (2.40)$$

Likewise, the tomograms at the instants $T_{\rm rev}/2$ and $T_{\rm rev}/6$ are similar, and have four strands each. This follows from the fact that $n(n-1)(n-2)/2$ and $n(n-1)(n-2)/6$ are integers with the same parity.

We now examine the situation that arises if there is more than one time scale in the Hamiltonian. Consider the Hamiltonian

$$H_1 = (\chi_1 a^{\dagger 2} a^2 + \chi_2 a^{\dagger 3} a^3), \quad (2.41)$$

where χ_1, χ_2 are positive constants. For irrational χ_1/χ_2, revivals are absent. The generic tomogram obtained at any instant, is blurred. (See Fig. 2.3 for an initial CS

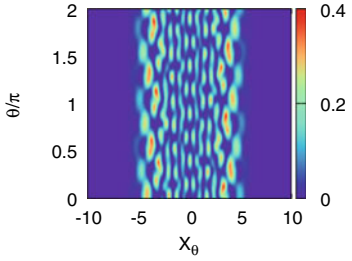

Fig. 2.3 Tomogram of an initial CS at $t = \pi/\chi_2$ for $\alpha = \sqrt{10}e^{i\pi/4}$, $\chi_1 = 1$ and $\chi_2 = 10^{-7}/\sqrt{2}$. This figure is reproduced from [25]

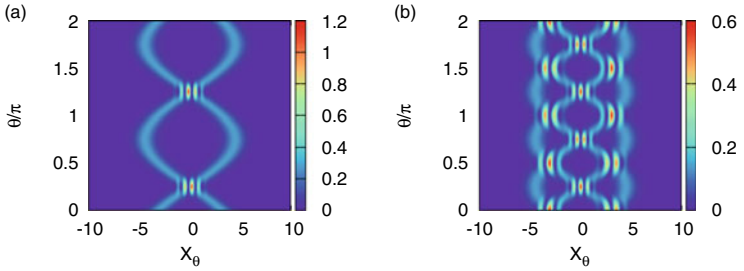

Fig. 2.4 Tomograms of an initial CS at $t = T_{\rm rev}/2$ for $\alpha = \sqrt{10}e^{i\pi/4}$, $\chi_1 = 1$ and **a** $\chi_2 = 2.048 \times 10^{-7}$, **b** $\chi_2 = 1.024 \times 10^{-7}$. Figures are reproduced from [25]

with $\alpha = \sqrt{10}\, e^{i\pi/4}$, $\chi_1 = 1$ and $\chi_2 = 10^{-7}/\sqrt{2}$, at $t = \pi/\chi_2$.) When the ratio χ_1/χ_2 is a rational number, revivals occur at $T_{\rm rev}/\pi$ (equal to the LCM of $1/\chi_1$ and $1/\chi_2$).

As before, fractional revivals occur at instants $T_{\rm rev}/\ell$ but the corresponding tomogram patterns depend sensitively on the ratio χ_1/χ_2. While we naively expect that, for a given ℓ, the tomogram will have ℓ strands due to the presence of the Kerr term in H_1, the additional cubic term however, allows for other possibilities. This is illustrated in Fig. 2.4 for an initial CS with $\alpha = \sqrt{10}\, e^{i\pi/4}$. For instance, at $T_{\rm rev}/2$, apart from the two-strand tomogram (Fig. 2.4a) for $\chi_1 = 1$ and $\chi_2 = 2.048 \times 10^{-7}$, one of the other possibilities is the four-strand tomogram (Fig. 2.4b) for $\chi_1 = 1$ and $\chi_2 = 1.024 \times 10^{-7}$. Such additional possibilities can be explained on a case by case basis. They arise because of the periodicity properties of the unitary time evolution operator at relevant instants of time. Thus the 'naive' conclusion that an ℓ-subpacket fractional revival is associated *solely* with an ℓ-strand tomogram does not hold good in cases where there is an interplay between different time scales.

The sensitivity to the ratio χ_1/χ_2 noted above could, in principle, be of significance in understanding the role of higher-order susceptibilities through experiments. However, while for our computations we have scaled χ_1 to unity, in practice, the susceptibility parameter is numerically small for a Kerr medium. As a consequence, field damping occurs on a much shorter time scale than $T_{\rm rev}$. It is therefore quite difficult, experimentally, to sustain the field revival phenomena, even till the instant $T_{\rm rev}$. Although still in a nascent stage, such studies are now being carried out [26] by

engineering an artificial Kerr medium with sufficiently high susceptibility, in which collapses and revivals of a coherent state can be observed. Further, experiments [27, 28] have been performed in circuit QED to implement Kerr-type nonlinearities in single-mode and bipartite systems. The coherence time of the microwave cavity in circuit QED has also increased significantly, to the order of milliseconds [29]. It should therefore be possible to experimentally identify the subtle effects arising due to higher-order nonlinearities through tomographic signatures, as we have pointed out in the foregoing.

2.7 Decoherence Effects

We now proceed to investigate the effect of an external environment. Specifically, we wish to examine the decoherence effects that set in due to the interaction between the field state and the environment. As a simple example, we consider the state at $T_{\rm rev}/2$, of an initial CS evolving under the Hamiltonian H_1. The field is allowed to interact with the environment. The procedure employed here is similar to that in [24], where the Kerr Hamiltonian governed the evolution. This facilitates comparison between the two cases.

Two commonly used models of decoherence are amplitude decay and phase damping. In the former, the master equation is given by

$$\frac{\mathrm{d}\varrho}{\mathrm{d}\tau} = -\Gamma(a^\dagger a\varrho - 2a\varrho a^\dagger + \varrho a^\dagger a). \tag{2.42}$$

Here ϱ denotes the density matrix, Γ is the rate of loss of photons and the time parameter τ is reckoned from the instant $T_{\rm rev}/2$. The solution to Eq. (2.42) is [30]

$$\varrho(\tau) = \sum_{n,n'=0}^{\infty} \varrho_{n,n'}(\tau)|n\rangle\left\langle n'\right|, \tag{2.43}$$

with matrix elements given by

$$\varrho_{n,n'}(\tau) = e^{-\Gamma\tau(n+n')} \sum_{r=0}^{\infty} \binom{n+r}{r}^{1/2} \binom{n'+r}{r}^{1/2} (1-e^{-2\Gamma\tau})^r \varrho_{n+r,n'+r}(0). \tag{2.44}$$

Tomograms corresponding to this choice of state for different parameter values and $\Gamma\tau = 1$ are shown in Fig. 2.5a, b. It can be verified that $\varrho \to |0\rangle\langle 0|$ in the limit $\Gamma\tau \to \infty$, as expected. The purity $\mathrm{Tr}\,\varrho^2$ initially decreases from unity (corresponding to the initial pure state), and subsequently rises back to unity when $\Gamma\tau \approx 4.5$ (Fig. 2.5c). The extent of the loss of purity depends on the numerical value of χ_1/χ_2. Additionally, this ratio could give rise to new features in the decoherence phenomenon, due to the

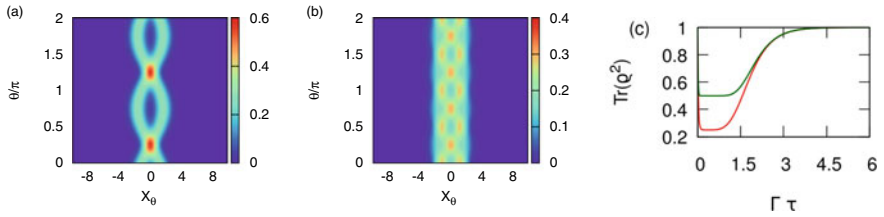

Fig. 2.5 Tomograms for an initial CS at $T_{\rm rev}/2$ in the amplitude decay model, for $\alpha = \sqrt{10}\, e^{i\pi/4}$, $\Gamma\tau = 1$, $\chi_1 = 1$ and **a** $\chi_2 = 2.048 \times 10^{-7}$, **b** $\chi_2 = 1.024 \times 10^{-7}$. **c** Tr ϱ^2 versus $\Gamma\tau$ for $\chi_1 = 1$ and $\chi_2 = 2.048 \times 10^{-7}$ (green), $\chi_2 = 1.024 \times 10^{-7}$ (red). Figures are reproduced from [25]

possibility of appearance of several distinct tomograms at $T_{\rm rev}/2$ which are sensitive to this ratio, as explained earlier.

If we consider dissipation through the phase damping model, the master equation [30] is given by

$$\frac{d\overline{\varrho}}{d\tau} = -\Gamma_p(\mathsf{N}^2\overline{\varrho} - 2\mathsf{N}\overline{\varrho}\mathsf{N} + \overline{\varrho}\mathsf{N}^2), \tag{2.45}$$

where $\overline{\varrho}$ is the density matrix in this model and Γ_p is the decoherence rate. The solution to this master equation [30] can again be expressed in the form given in Eq. (2.43), with matrix elements

$$\overline{\varrho}_{n,n'}(\tau) = e^{-\Gamma_p\tau(n-n')^2}\overline{\varrho}_{n,n'}(0). \tag{2.46}$$

It is obvious that, as $\Gamma_p\tau \to \infty$, the off-diagonal terms of the density matrix vanish, while all diagonal terms do not change from their initial values $\overline{\varrho}_{n,n}(0)$. In contrast to the case of amplitude damping, as $\Gamma_p\tau \to \infty$, the state remains mixed. Further, the differences between tomograms with different strand structures disappear faster than in the case of amplitude damping. The effect of phase damping is seen in Fig. 2.6a, b at $\Gamma_p\tau = 0.1$ for two such ratios. The differences reduce with increase in $\Gamma_p\tau$ till at $\Gamma_p\tau = 1$ they are barely visible.

2.8 A Tomographic Approach to the Double-Well BEC System

We begin by defining tomograms for bipartite systems. Recall that rotated quadratures are defined for a bipartite system comprising subsystems A and B as

$$\mathbb{X}_{\theta_a} = (a^\dagger e^{i\theta_a} + a e^{-i\theta_a})/\sqrt{2}, \qquad \mathbb{X}_{\theta_b} = (b^\dagger e^{i\theta_b} + b e^{-i\theta_b})/\sqrt{2}. \tag{2.47}$$

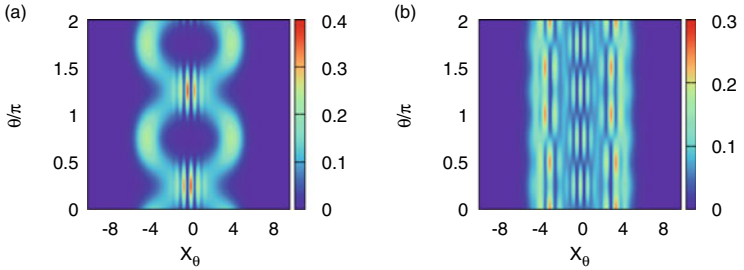

Fig. 2.6 Tomograms of an initial CS at $T_{\rm rev}/2$ in the phase damping model for $\alpha = \sqrt{10}\, e^{i\pi/4}$, $\Gamma_p \tau = 0.1$, $\chi_1 = 1$ and **a** $\chi_2 = 2.048 \times 10^{-7}$, **b** $\chi_2 = 1.024 \times 10^{-7}$. Figures are reproduced from [25]

Here $(a, a^\dagger)$ and $(b, b^\dagger)$ are the particle annihilation and creation operators corresponding to A and B, respectively. The bipartite tomogram is

$$\omega(X_{\theta_a}, \theta_a; X_{\theta_b}, \theta_b) = \langle X_{\theta_a}, \theta_a; X_{\theta_b}, \theta_b | \rho_{AB} | X_{\theta_a}, \theta_a; X_{\theta_b}, \theta_b \rangle, \tag{2.48}$$

where ρ_{AB} is the bipartite density matrix and $\mathbb{X}_{\theta_i} | X_{\theta_i}, \theta_i \rangle = X_{\theta_i} | X_{\theta_i}, \theta_i \rangle$ $(i = a, b)$. We shall denote $|X_{\theta_a}, \theta_a\rangle \otimes |X_{\theta_b}, \theta_b\rangle$ by $|X_{\theta_a}, \theta_a; X_{\theta_b}, \theta_b\rangle$. The tomogram satisfies the normalization condition,

$$\int_{-\infty}^{\infty} \mathrm{d}X_{\theta_a} \int_{-\infty}^{\infty} \mathrm{d}X_{\theta_b} \omega(X_{\theta_a}, \theta_a; X_{\theta_b}, \theta_b) = 1 \tag{2.49}$$

for each θ_a and θ_b.

As in the earlier case, we consider a pure state $|\psi\rangle$ expanded in the Fock basis sets $\{|m\rangle\}, \{|n\rangle\}$ corresponding to A and B, respectively, as $|\psi\rangle = \sum_{m,n=0}^{\infty} c_{mn} |m; n\rangle$, where $|m; n\rangle \equiv |m\rangle \otimes |n\rangle$. The procedure used in deriving Eq. (2.38) in the single-mode example illustrated earlier can be extended in a straightforward manner to generic bipartite systems whose subsystems are infinite dimensional. We then obtain

$$\omega(X_{\theta_a}, \theta_a; X_{\theta_b}, \theta_b) = \frac{e^{-X_{\theta_a}^2 - X_{\theta_b}^2}}{\pi} \left| \sum_{m,n=0}^{\infty} \frac{c_{mn} e^{-i(m\theta_a + n\theta_b)}}{(m! n! 2^{m+n})^{1/2}} H_m(X_{\theta_a}) H_n(X_{\theta_b}) \right|^2. \tag{2.50}$$

The reduced tomograms corresponding respectively to the subsystems A and B are given by

$$\omega_A(X_{\theta_a}, \theta_a) = \langle X_{\theta_a}, \theta_a | \rho_A | X_{\theta_a}, \theta_a \rangle = \int_{-\infty}^{\infty} \omega(X_{\theta_a}, \theta_a; X_{\theta_b}, \theta_b) \mathrm{d}X_{\theta_b} \tag{2.51}$$

for any fixed value of θ_b, and

$$\omega_B(X_{\theta_b}, \theta_b) = \langle X_{\theta_b}, \theta_b | \rho_B | X_{\theta_b}, \theta_b \rangle = \int_{-\infty}^{\infty} \omega(X_{\theta_a}, \theta_a; X_{\theta_b}, \theta_b) \mathrm{d}X_{\theta_a} \tag{2.52}$$

for any fixed value of θ_a. The reduced density matrix ρ_A [respectively, ρ_B] is given by $\mathrm{Tr}_B\,(\rho_{AB})$ [resp., $\mathrm{Tr}_A\,(\rho_{AB})$].

The specific model we now consider is the Bose–Einstein condensate in a double-well potential. The effective Hamiltonian of this bipartite system is [31]

$$H_{\mathrm{BEC}} = \omega_0 \mathsf{N}_{\mathrm{tot}} + \omega_1 (a^\dagger a - b^\dagger b) + u_0 \mathsf{N}_{\mathrm{tot}}^2 - \lambda (a^\dagger b + a b^\dagger), \tag{2.53}$$

setting $\hbar = 1$, and where ω_0, ω_1, u_0 and λ are positive constants. In this case, $(a, a^\dagger)$ and $(b, b^\dagger)$ are the boson annihilation and creation operators for the condensate atoms in the two wells, satisfying $[a, a^\dagger] = [b, b^\dagger] = 1, [a, b] = 0$, etc. $\mathsf{N}_{\mathrm{tot}} = (a^\dagger a + b^\dagger b)$ and u_0 is the nonlinearity strength. It can be readily seen that $[H_{\mathrm{BEC}}, \mathsf{N}_{\mathrm{tot}}] = 0$. We denote by $|\alpha_A\rangle$ [respectively, $|\alpha_B\rangle$] the CS formed from the condensate corresponding to subsystem A [resp., B] and by $|\alpha_A, 1\rangle$ [resp., $|\alpha_B, 1\rangle$] a 1-boson-added CS corresponding to A [resp., B]. The initial states are direct product states $|\alpha_A\rangle \otimes |\alpha_B\rangle$ (denoted by $|\Psi_{00}\rangle$), $|\alpha_A, 1\rangle \otimes |\alpha_B, 1\rangle$ (denoted by $|\Psi_{11}\rangle$) and $|\alpha_A, 1\rangle \otimes |\alpha_B\rangle$ (denoted by $|\Psi_{10}\rangle$).

The state at any time $t > 0$ is, in general, entangled. In [31] it has been shown that, corresponding to the initial state $|\Psi_{00}\rangle$,

$$|\Psi_{00}(t)\rangle = e^{-\frac{1}{2}(|\alpha_A|^2 + |\alpha_B|^2)} \sum_{p,q=0}^{\infty} \frac{(\alpha(t))^p (\beta(t))^q}{\sqrt{p!q!}} e^{-it[\omega_0(p+q) + u_0(p+q)^2]} |p; q\rangle. \tag{2.54}$$

Here, $|p; q\rangle$ denotes $|p\rangle \otimes |q\rangle$ where $\{|p\rangle\}$, $\{|q\rangle\}$ are the boson number basis sets of A and B respectively, and

$$\left.\begin{aligned} \alpha(t) &= \alpha_A \cos(\lambda_1 t) + i[(\lambda\alpha_B - \omega_1\alpha_A)/\lambda_1] \sin(\lambda_1 t), \\ \beta(t) &= \alpha_B \cos(\lambda_1 t) + i[(\lambda\alpha_A + \omega_1\alpha_B)/\lambda_1] \sin(\lambda_1 t), \end{aligned}\right\} \tag{2.55}$$

with $\lambda_1 = (\omega_1^2 + \lambda^2)^{1/2}$. A similar procedure has been used to obtain [25] the states $|\Psi_{10}(t)\rangle$, $|\Psi_{11}(t)\rangle$ and the expression for the density matrix corresponding to the direct product $|\alpha_A, m_1\rangle \otimes |\alpha_B, m_2\rangle$ of generic boson-added coherent states (m_1 and m_2 are positive integers). The revivals and fractional revivals that occur during temporal evolution, corresponding to all the three initial states have been investigated. For illustrative purposes, we describe the results corresponding to the initial state $|\Psi_{00}\rangle$ below.

Full and fractional revivals occur, with a revival time $T_{\mathrm{rev}} = \pi/u_0$, provided $\omega_0 = m u_0$ and $\lambda_1 = m' u_0$, where m, m' are integers and $(m + m')$ is odd. This is a consequence of the periodicity property of $e^{-iu_0 N_{\mathrm{tot}}^2 t}$ for special values of t. For the

initial state $|\Psi_{00}\rangle$, the state at time $t = \pi/(su_0)$ is

$$|\Psi_{00}(\pi/su_0)\rangle = \sum_{j=0}^{s-1} f_j \left|\alpha(\pi/su_0)e^{-i\pi(m+2j)/s}\right\rangle \otimes \left|\beta(\pi/su_0)e^{-i\pi(m+2j)/s}\right\rangle \tag{2.56}$$

if s is an even integer, and

$$|\Psi_{00}(\pi/su_0)\rangle = \sum_{j=0}^{s-1} g_j \left|\alpha(\pi/su_0)e^{-i\pi(m+2j+1)/s}\right\rangle \otimes \left|\beta(\pi/su_0)e^{-i\pi(m+2j+1)/s}\right\rangle \tag{2.57}$$

if s is an odd integer. Here $\alpha(\pi/su_0)$ and $\beta(\pi/su_0)$ can be read off from Eq. (2.55), and f_j, g_j are known Fourier coefficients. In this bipartite system the tomogram is a 4-dimensional hypersurface. We therefore consider appropriate sections to identify and examine nonclassical effects. The 2-dimensional $(X_{\theta_b}, X_{\theta_a})$ section, for specific values of θ_a and θ_b, is a natural choice for our purpose. In contrast to the single-mode case where strands appear in the tomograms, these sections are characterized by 'blobs' at the instants of fractional revivals. The number of blobs gives the number of sub-packets in the corresponding state. We have also used a direct product of truncated coherent states (TCS) [32] instead of $|\Psi_{00}\rangle$, to examine subsequent revivals and fractional revivals. The TCS is defined as

$$|\alpha\rangle_{\rm TCS} = \sum_{n=0}^{N_{\rm max}} \frac{\alpha^n}{\sqrt{n!}}|n\rangle \Big/ \Big(\sum_{n=0}^{N_{\rm max}} \frac{|\alpha|^{2n}}{n!}\Big)^{1/2} \tag{2.58}$$

where $N_{\rm max}$ is a sufficiently large but finite integer. We have verified that the results in this case agree with those corresponding to the initial state $|\Psi_{00}\rangle$. Figure 2.7a–d are tomograms corresponding to different fractional revivals for the initial state $|\Psi_{00}\rangle$ with $\theta_a = \theta_b = 0$, $\omega_0 = 10$, $\omega_1 = 3$, $\lambda = 4$, $u_0 = 1$, and $\alpha_A = \alpha_B = \sqrt{10}$. At the instants $T_{\rm rev}/4$, $T_{\rm rev}/3$ and $T_{\rm rev}$ (Fig. 2.7a, b, d), there are 4 blobs, 3 blobs and 1 blob, respectively, in the corresponding tomograms, along with interference patterns. In Fig. 2.7c, blobs are absent due to interference effects that arise because α_A and α_B have been chosen to be real numbers. It then follows from Eq. (2.56) that the state of the system at $t = \frac{1}{2}T_{\rm rev}$ can be expanded in terms of superpositions of direct products of CS corresponding to A and B as

$$|\Psi_{00}\left(\frac{1}{2}T_{\rm rev}\right)\rangle = \frac{(1-i)}{2}\left|\frac{-2i}{\sqrt{10}}\right\rangle \otimes \left|\frac{-14i}{\sqrt{10}}\right\rangle + \frac{(1+i)}{2}\left|\frac{2i}{\sqrt{10}}\right\rangle \otimes \left|\frac{14i}{\sqrt{10}}\right\rangle \tag{2.59}$$

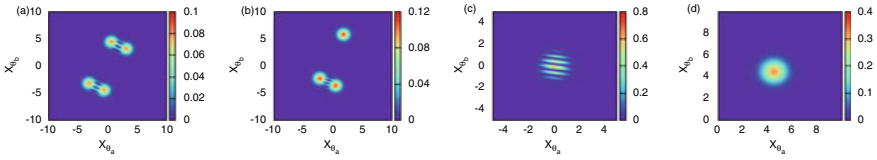

Fig. 2.7 Sections of the optical tomogram for $\theta_a = \theta_b = 0$ at instants **a** $T_{\rm rev}/4$, **b** $T_{\rm rev}/3$, **c** $T_{\rm rev}/2$, and **d** $T_{\rm rev}$. $\alpha_A = \alpha_B = \sqrt{10}$, and initial state $|\Psi_{00}\rangle$. Figures are reproduced from [25]

A simple calculation now gives

$$|\Psi_{00}(X_{A0}, X_{B0})|^2 = |\langle X_{A0}, 0; X_{B0}, 0|\Psi_{00}(T_{\rm rev}/2)\rangle|^2$$
$$= \frac{e^{-(X_{A0}^2+X_{B0}^2)}}{\pi}\left\{1 - \frac{1}{\sqrt{5}}\sin\left[4(X_{A0} + 7X_{B0})\right]\right\}, \qquad (2.60)$$

where $X_{A0} \equiv X_{\theta_a}(\theta_a = 0)$ and $X_{B0} \equiv X_{\theta_b}(\theta_b = 0)$.

It can be now easily argued that if α_A and α_B are general complex numbers, along with the interference pattern two blobs also would appear in the tomogram at $t = \frac{1}{2}T_{\rm rev}$. The analysis corresponding to the initial states $|\Psi_{11}\rangle$ and $|\Psi_{10}\rangle$ yields results similar to those mentioned above.

To conclude this chapter: Wave packet revival phenomena have been investigated for many decades now, and interesting results on full and fractional revivals in different physical systems have been reported in the literature. The manner in which tomograms can be exploited to capture various features of revivals, however, is a recent advance. In principle, this technique could be useful in extracting information about the state of a quantum mechanical system directly from its tomograms, circumventing the procedure for explicitly constructing the density matrix. Likewise, while the Talbot effect has been investigated in considerable detail over several years, its application to quantum information processing is relatively recent, and interesting possibilities in this regard are being explored.

References

1. H.F. Talbot, Philos. Mag. **9**, 401 (1836)
2. M.V. Berry, S. Klein, J. Mod. Opt. **43**, 2139 (1996)
3. M.V. Berry, I. Marzoli, W. Schleich, Phys. World **14**, 39 (2001)
4. R.W. Robinett, Phys. Rep. **392**, 1 (2004)
5. K. Pelka, J. Graf, T. Mehringer, J. von Zanthier, Opt. Express **26**, 15009 (2018)
6. D. Bigourd, B. Chatel, W.P. Schleich, B. Girard, Phys. Rev. Lett. **100**, 030202 (2008)
7. I. Vidal, S.B. Cavalcanti, E.J.S. Fonseca, J.M. Hickmann, Phys. Rev. A **78**, 033829 (2008)
8. X.-B. Song, H.-B. Wang, J. Xiong, K. Wang, X. Zhang, K.-H. Luo, L.-A. Wu, Phys. Rev. Lett. **107**, 033902 (2011)
9. O.J. Farías, F. de Melo, P. Milman, S.P. Walborn, Phys. Rev. A **91**, 062328 (2015)
10. G.S. Agarwal, J. Banerji, Phys. Rev. A **57**, 3880 (1998)

11. R. Bluhm, V.A. Kostelecky, Phys. Rev. A **50**, R4445 (1994); Phys. Lett. A **200**, 308 (1995)
12. V.P. Gutschick, M.M. Nieto, Phys. Rev. D **22**, 403 (1980)
13. J. Gea-Banacloche, Phys. Rev. Lett. **65**, 3385 (1990)
14. S.J.D. Phoenix, P.L. Knight, Phys. Rev. A **44**, 6023 (1991)
15. I.Sh. Averbukh, N.F. Perelman, Phys. Lett. A **139**, 449 (1989)
16. S. Seshadri, S. Lakshmibala, V. Balakrishnan, J. Stat. Phys. **101**, 213 (2000)
17. R.W. Robinett, Am. J. Phys. **68**, 410 (2000)
18. P. Tombesi, H.P. Yuen, *Coherence and Quantum Optics*, vol. V, ed. by L. Mandel, E. Wolf (Plenum, New York, 1984), p. 751
19. C. Sudheesh, S. Lakshmibala, V. Balakrishnan, Phys. Lett. A **329**, 14 (2004)
20. G.S. Agarwal, K. Tara, Phys. Rev. A **43**, 492 (1991)
21. C. Sudheesh, S. Lakshmibala, V. Balakrishnan, Europhys. Lett. **71**, 744 (2005)
22. E.A. Shapiro, M. Spanner, M.Yu. Ivanov, Phys. Rev. Lett. **91**, 237901 (2003)
23. S.N. Filippov, V.I. Man'ko, Phys. Scr. **83**, 058101 (2011)
24. M. Rohith, C. Sudheesh, Phys. Rev. A **92**(5), 053828 (2015). https://doi.org/10.1103/PhysRevA.92.053828
25. B. Sharmila, K. Saumitran, S. Lakshmibala, V. Balakrishnan, J. Phys. B At. Mol. Opt. **50**(4), 045501 (2017). https://doi.org/10.1088/1361-6455/aa51a4
26. G. Kirchmair, B. Vlastakis, Z. Leghtas, S.E. Nigg, H. Paik, E. Ginossar, M. Mirrahimi, L. Frunzio, S.M. Girvin, R.J. Schoelkopf, Nature **495**, 205 (2013)
27. Z. Leghtas, S. Touzard, I.M. Pop, A. Kou, B. Vlastakis, A. Petrenko, K.M. Sliwa, A. Narla, S. Shankar, M.J. Hatridge, M. Reagor, L. Frunzio, R.J. Schoelkopf, M. Mirrahimi, M.H. Devoret, Science **347**, 853 (2015)
28. E.T. Holland, B. Vlastakis, R.W. Heeres, M.J. Reagor, U. Vool, Z. Leghtas, L. Frunzio, G. Kirchmair, M.H. Devoret, M. Mirrahimi, R.J. Schoelkopf, Phys. Rev. Lett. **115**, 180501 (2015)
29. M. Reagor, W. Pfaff, C. Axline, R.W. Heeres, N. Ofek, K. Sliwa, E. Holland, C. Wang, J. Blumoff, K. Chou, M.J. Hatridge, L. Frunzio, M.H. Devoret, L. Jiang, R.J. Schoelkopf, Phys. Rev. B **94**, 014506 (2016)
30. A. Biswas, G.S. Agarwal, Phys. Rev. A **75**, 032104 (2007)
31. L. Sanz, M.H.Y. Moussa, K. Furuya, Ann. Phys. (N.Y.) **321**, 1206 (2006)
32. L.-M. Kuang, F.-B. Wang, Y.-G. Zhou, J. Mod. Opt. **41**, 1307 (1994)

Chapter 3
Tomographic Approach to Squeezing

3.1 Introduction

In this chapter, we examine the squeezing properties of a quantum state directly from tomograms. In contrast to the revival phenomena discussed in Chap. 2, there is no classical analog of squeezing. It stems from the uncertainty principle, which puts a lower bound on the product of the variances $(\Delta A)^2$ and $(\Delta B)^2$ of two non-commuting hermitian observables A and B in any state: if the commutator $[A, B] = iC$, then $(\Delta A)^2(\Delta B)^2 \geqslant \frac{1}{4}|\langle C\rangle|^2$. The state is said to be squeezed in A (respectively, in B) if $(\Delta A)^2$ (respectively, $(\Delta B)^2$) $< \frac{1}{2}|\langle C\rangle|$.

In the case of optical states, for instance, the uncertainty principle places a lower bound $(= \frac{1}{4})$ on the product of the variances of the quadrature operators X and P. A coherent state (CS) is an example of a quantum state in which the uncertainty product reaches its lower bound, and each of the variances $(\Delta X)^2 = (\Delta P)^2 = \frac{1}{2}$ in convenient units. However, if even a single photon is added to the CS, the resulting 1-photon added coherent state (1-PACS) has very different properties. For instance, it is an example of squeezed light. Generalizing X and P to the pair of operators $A_\varphi = (ae^{i\varphi} + a^\dagger e^{-i\varphi})/\sqrt{2}$ and $B_\varphi = (ae^{i\varphi} - a^\dagger e^{-i\varphi})/i\sqrt{2}$ which also satisfy $[A_\varphi, B_\varphi] = i$ for any value of the parameter φ, it can be shown that the variance of A_φ in the m-photon added CS $|\alpha, m\rangle$ is given by [1]

$$(\Delta A_\varphi)^2 = \left\{ \nu \left[L_m^2(-\nu)L_m(-\nu) - \left(L_m^1(-\nu)\right)^2 \right] \cos\, 2(\delta + \varphi) - \nu \left(L_m^1(-\nu)\right)^2 \right.$$
$$\left. - \frac{1}{2}\left(L_m(-\nu)\right)^2 + (m+1)L_{m+1}(-\nu)L_m(-\nu) \right\} \Big/ \left(L_m(-\nu)\right)^2, \quad (3.1)$$

where $\nu = |\alpha|^2$, $\alpha = \nu^{1/2}e^{i\delta}$, L_m is the Laguerre polynomial of order m, and L_m^1, L_m^2 are associated Laguerre polynomials. Setting the phases such that $\delta + \varphi = \pi$, squeezing in A_φ to the extent of nearly 50% can be obtained for a range of values of ν, if m is non-zero.

© The Author(s), under exclusive license to Springer Nature Switzerland AG 2022

S. Lakshmibala and V. Balakrishnan, *Nonclassical Effects and Dynamics of Quantum Observables*, SpringerBriefs in Physics,
https://doi.org/10.1007/978-3-031-19414-6_3

Diverse squeezed states of light have been examined in the literature [2]. These could be either finite or infinite superpositions of photon number states. An example of the former is the state $|\psi\rangle = (\sqrt{3}|0\rangle + |1\rangle)/2$, while an example of the latter is the squeezed vacuum. The role played by the squeezed vacuum in gravitational-wave detectors has also provided considerable impetus to the production and detection of various forms of squeezed light [3]. An important reason for the current interest in squeezed light is its use in quantum information processing and quantum metrology. A detailed review of the generation and detection of squeezed light and its applications may be found in [4].

Higher-order squeezing was first proposed in [5]. A state is said to be squeezed in the operator A to order q $(= 1, 2, \ldots)$ if, the mean $\langle(\delta A)^{2q}\rangle$ obtained in that state, is less than the corresponding value for a CS. Here, $\delta A = A - \langle A\rangle$. In the X quadrature, this condition becomes

$$\langle(\delta X)^{2q}\rangle < 2^{-q}(2q-1)!! \tag{3.2}$$

Another type of higher-order squeezing, namely, amplitude-squared squeezing, was first defined in [6], and subsequently generalized in [7] to qth-power amplitude-squeezing. (Amplitude-squared squeezing corresponds to the case $q = 2$.) One defines the pair of quadrature variables

$$Z_1 = (a^q + a^{\dagger q})/\sqrt{2},\ \ Z_2 = (a^q - a^{\dagger q})/i\sqrt{2}\ \ \ (q = 1,\ 2,\ 3, \ldots). \tag{3.3}$$

The generalized uncertainty principle now reads

$$(\Delta Z_1)^2\,(\Delta Z_2)^2 \geqslant \frac{1}{4}\,|\langle\,[Z_1, Z_2]\,\rangle|^2\,. \tag{3.4}$$

The state is said to be qth-power amplitude-squeezed in the variable Z_1 if

$$(\Delta Z_1)^2 < \frac{1}{2}\,|\langle\,[Z_1\,,\ Z_2]\,\rangle|\,. \tag{3.5}$$

A quantifier of the extent of qth-power amplitude-squeezing in Z_1 is given by the quantity

$$D_q = \frac{(\Delta Z_1)^2 - \frac{1}{2}\langle F_q(\mathsf{N})\rangle}{\frac{1}{2}\langle F_q(\mathsf{N})\rangle}, \tag{3.6}$$

where N is the number operator $a^\dagger a$, and $F_q(\mathsf{N})$ is the commutator $[a^q\,,\ a^{\dagger q}]$, a polynomial of order $(q-1)$ in N given by

$$F_q(\mathsf{N}) = q!\,\left\{1 + \sum_{n=1}^{q-1} \tbinom{q}{n} \tfrac{1}{n!}\,\mathsf{N}(\mathsf{N}-1)\cdots(\mathsf{N}-(n-1))\right\}. \tag{3.7}$$

The expression for D_q in Eq. (3.6) can be rewritten in terms of a^q and $a^{\dagger q}$ as

$$D_q = \frac{2\left\{\text{Re}\,\langle a^{2q}\rangle - 2\,(\text{Re}\,\langle a^q\rangle)^2 + \langle a^{\dagger q}\,a^q\rangle\right\}}{\langle F_q(\mathsf{N})\rangle}. \tag{3.8}$$

It is straightforward to see that a state is qth-power amplitude-squeezed in Z_1 if $-1 \leqslant D_q < 0$. An analogous criterion holds for squeezing in Z_2. It is evident that D_q can be used to quantify the extent of squeezing at any instant during the temporal evolution of a system, by calculating the required expectation values in the state of the system at that instant. This exercise has been carried out, for instance, in estimating the squeezing properties of an initial CS or PACS propagating through a Kerr medium [8]. While D_q and other similar quantifiers can be employed to calculate the extent of squeezing and higher-order squeezing of a known state, most often it would be useful to read off the squeezing properties directly from the quadrature tomogram, avoiding reconstruction of the density matrix altogether. We discuss this in a subsequent section. We turn now to another aspect of squeezing, namely, the tomographic entropic squeezing.

3.2 Entropic Squeezing from Optical Tomograms

Inspired by the Shannon entropy for classical probability distributions, the tomographic information entropy for a single-mode system for a specified value of θ is analogously given by

$$S(\theta) = -\int \omega(X_\theta, \theta)\ln\left[\omega(X_\theta, \theta)\right] dX_\theta \tag{3.9}$$

where $\omega(X_\theta, \theta) = \langle X_\theta, \theta|\,\rho\,|X_\theta, \theta\rangle$, as defined in Eq. (2.37). This information entropy can be computed readily from the tomogram. It is straightforward to extend this definition to a bipartite system AB. The tomographic entropy of the subsystem A for any specific value of θ_b is

$$S_A(\theta_a) = -\int \omega(X_{\theta_a}, \theta_a)\ \ln\left[\omega(X_{\theta_a}, \theta_a)\right] dX_{\theta_a}, \tag{3.10}$$

where

$$\omega(X_{\theta_a}, \theta_a) = \int \omega(X_{\theta_a}, \theta_a, X_{\theta_b}, \theta_b)\, dX_{\theta_b}. \tag{3.11}$$

S_A is independent of the value of θ_b chosen, and

$$\int \omega(X_{\theta_a}, \theta_a)\, dX_{\theta_a} = 1. \tag{3.12}$$

A similar definition can be given for the entropy of subsystem B.

There exists an extensive literature on information entropy, its generalizations, entropic uncertainty relations, and their applications, particularly in quantum cryptography (see, for instance, [9]). In what follows, we merely draw attention to the aspects of relevance to the squeezing properties of a state. We first consider single-mode systems. Analogous to the Shannon entropy, the entropies S_X and S_P associated with position and momentum respectively of a quantum system are expressed in terms of the conjugate wave functions $\psi(x)$ and $\widetilde{\psi}(p)$ as $S_X = -\int |\psi(x)|^2 \log |\psi(x)|^2 dx$ and $S_P = -\int |\widetilde{\psi}(p)|^2 \log |\widetilde{\psi}(p)|^2 dp$. The idea that their sum satisfies a bound that is tighter than the bound in terms of the product of variances was first conjectured in the context of the many-worlds interpretation of quantum mechanics, propounded in 1957 by Everett in his doctoral thesis, and published subsequently in [10]. Shortly thereafter, also in 1957, this conjecture was corroborated from a mathematical point of view and the bound on the sum of entropies was proposed in general for a function and its Fourier transform in [11]. The standard uncertainty principle (originally due to Heisenberg, and formalized by Kennard and Robertson) can be derived from this entropic principle, but not *vice versa*. This elevates the entropic uncertainty relation to a status higher than that of the standard principle in terms of products of variances. The formal rigorous proofs were provided subsequently in [12] and independently in [13], where it was established that

$$S_X + S_P \geqslant 1 + \ln \pi. \tag{3.13}$$

An elegant argument proving that 'variance squeezing' is always accompanied by a corresponding entropy reduction below the vacuum level entropy, even for non-Gaussian states (both pure and mixed), is given in [14].

The proposal to use entropy as a measure of uncertainty for discrete spectra, taking into account the uncertainty in the measuring device as well, was made in [15]. This was followed by an extension of the idea to systems with both discrete and continuous spectra such as angle and angular momentum, position and linear momentum, etc., in [16]. New bounds have also been obtained on the sums of the entropies of conjugate observables, taking into account the effect of the entropy before measurement (see, for instance, [17]).

We now illustrate, with representative single-mode field states, some results on variance squeezing and entropic squeezing deduced directly from optical tomograms. We ignore the measurement device and the entropy of the system before measurement. The states considered are the ECS, OCS and their Janus-faced partners, and the YSS, defined in Chap. 1. Their tomograms [18] are presented in Fig. 3.1.[1] It follows from the definitions of these states that, for sufficiently large values of $|\alpha|$, the tomograms for the ECS, the OCS and the YSS are identical (Fig. 3.1f). The Janus-faced nature of partner states is also revealed in the tomograms. As expected,

[1] For figures similar to Figs. 3.1, 3.2 and 3.3, but for different values of the parameters, see "*Estimation of nonclassical properties of multiphoton coherent states from optical tomograms*", Laha et al. [18].

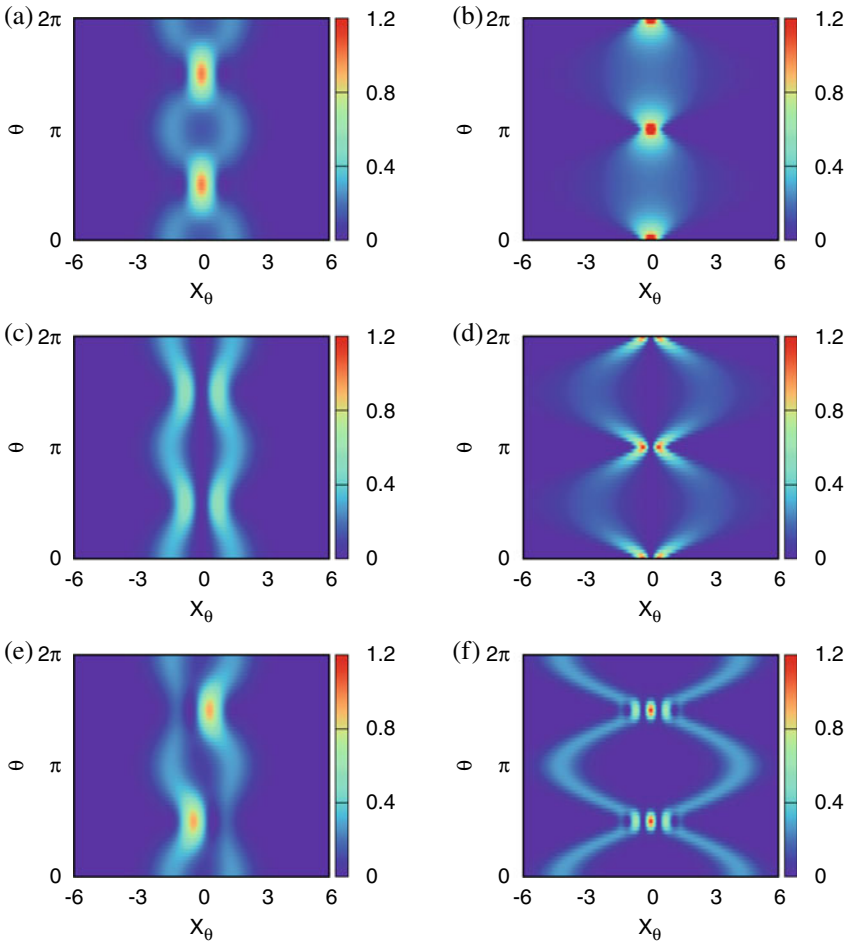

Fig. 3.1 Tomograms for **a** the ECS, **b** the squeezed vacuum state, **c** the OCS, **d** the Yuen state and **e** the YSS with $\alpha = \xi = 1$ and **f** the ECS/OCS/YSS with $|\alpha|^2 = 9$. The tomograms for (**a**)–(**e**) with $\alpha = \xi = 1/\sqrt{2}$, and for **f** with $|\alpha|^2 = 10$ are reported in [18]

the tomograms for the ECS and the squeezed vacuum state (Fig. 3.1a, b) (respectively, the OCS and the Yuen state (Fig. 3.1c, d)) are very similar, apart from a phase shift. For sufficiently large values of $|\alpha|$, the tomograms corresponding to the ECS and the OCS, which are superpositions of two CS, are two-stranded. As expected, this feature holds for the YSS as well (Fig. 3.1f). It is therefore evident that it is not possible to identify the state uniquely by merely inspecting the tomogram.

In Fig. 3.2, the entropic squeezing properties of the foregoing single-mode states are shown as a function of the state parameter, namely, $|\alpha|$ for the cat states and $|\xi|$ for the squeezed vacuum and the Yuen state. The entropy corresponding to the ECS, the OCS and the YSS is squeezed in the momentum quadrature, for a range of

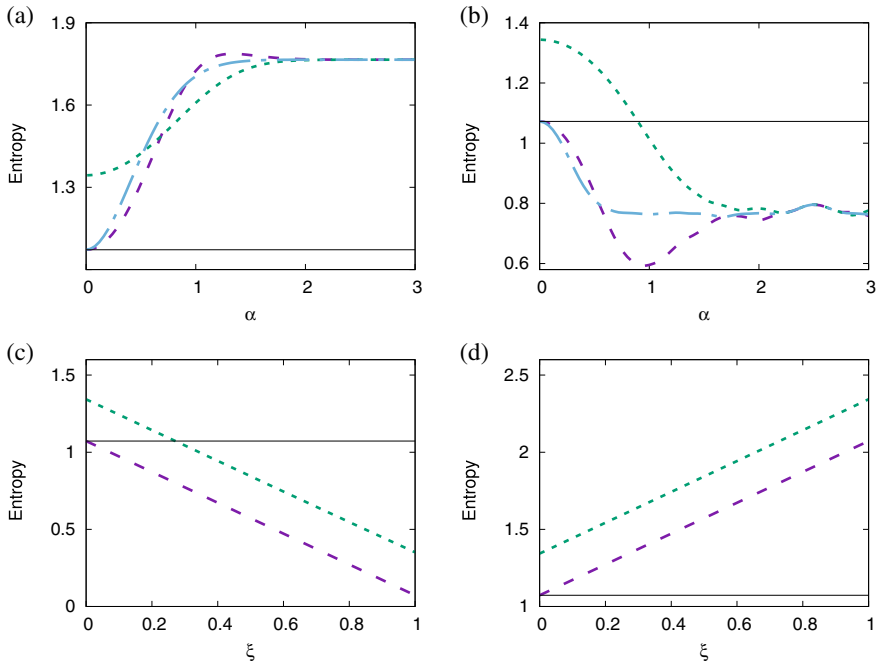

Fig. 3.2 Tomographic entropy as a function of the state parameter. Top panel: for the ECS (violet), the OCS (green) and the YSS (blue). Bottom panel: for the squeezed vacuum (violet) and the Yuen state (green). The first and the second columns respectively correspond to $\theta = n\pi$ and $n\pi + \frac{1}{2}\pi$, where $n = 0, 1, 2, \ldots$. The horizontal lines denote the value below which entropic squeezing occurs. For similar figures with $\theta = 0$ and $\frac{1}{2}\pi$, see [18]

parameter values (Fig. 3.2a, b). In contrast, the tomographic entropy, as a function of $|\xi|$ for the Janus-faced partners of the ECS and OCS, exhibits squeezing in the X quadrature and not in P (Fig. 3.2c, d), consistent with the phase shift between the corresponding tomograms.

3.3 Quadrature and Higher-Order Squeezing from Optical Tomograms

As a first step toward estimating the extent of quadrature squeezing and higher-order squeezing, we need to calculate the normal-ordered moments from optical tomograms. An elegant procedure to carry this out in the case of infinite dimensional single-mode systems is provided in detail in [19]. A brief outline of this procedure [20] is given below. The starting point is the expansion of any normal-ordered operator F in the form

$$F = \sum_{k,l=0}^{\infty} F_{k,l} a^{\dagger k} a^{l}. \tag{3.14}$$

Here the coefficients $F_{k,l}$ are given by

$$F_{k,l} = \sum_{s=0}^{\{k,l\}} \frac{(-1)^s}{s!\sqrt{(k-s)!(l-s)!}} \langle k-s|\, F\, |l-s\rangle, \tag{3.15}$$

where $\{k, l\}$ denotes $\min(k, l)$. Equation (3.15) is verified as follows. Using Eq. (3.14) for the matrix element $\langle p|\, F\, |q\rangle$ and substituting the result in Eq. (3.15), we get

$$F_{k,l} = \sum_{s=0}^{\{k,l\}} \sum_{u=0}^{\{k-s,l-s\}} \frac{(-1)^s}{s!u!} F_{k-s-u,l-s-u}. \tag{3.16}$$

Replacing u with $u' = s + u$, interchanging the order of the sums, and using the fact that

$$\sum_{s=0}^{k} \frac{(-1)^s}{s!(k-s)!} = \delta_{k,0}, \tag{3.17}$$

Equation (3.16) reduces to an identity, verifying Eq. (3.15). The projection operator $|k\rangle\langle l|$ may be expanded in the form

$$|k\rangle\langle l| = (k!l!)^{-1/2} \sum_{u=0}^{\infty} \frac{(-1)^u}{u!} a^{\dagger k+u} a^{l+u}. \tag{3.18}$$

Using $F = \sum_{k,l=0}^{\infty} |l\rangle\langle k|\ \mathrm{Tr}(|k\rangle\langle l|\, F)$ and Eq. (3.18), we see that

$$F = \sum_{k,l=0}^{\infty} A_{k,l} \mathrm{Tr}\,(a^{\dagger k} a^{l} F), \tag{3.19}$$

where

$$A_{k,l} = \sum_{s=0}^{\{k,l\}} \frac{(-1)^s}{s!\sqrt{(k-s)!(l-s)!}} |l-s\rangle\langle k-s|\,. \tag{3.20}$$

We now consider the special case when F is the density operator ρ. Using Eqs. (3.19) and (3.20), the relation

$$\langle X_\theta, \theta|m\rangle\langle n|X_\theta, \theta\rangle = \frac{e^{-X_\theta^2}}{\sqrt{\pi}} \frac{e^{-i(m-n)\theta}}{\sqrt{m!n!}\sqrt{2^{m+n}}} H_m(X_\theta) H_n(X_\theta) \tag{3.21}$$

as well as the identity

$$H_{k+l}(X_\theta) = \sum_{s=0}^{\{k,l\}} \frac{(-2)^s k!l! H_{k-s}(X_\theta) H_{l-s}(X_\theta)}{s!(k-s)!(l-s)!}, \tag{3.22}$$

satisfied by the Hermite polynomials, we can show that

$$\begin{aligned} \omega(X_\theta, \theta) &= \langle X_\theta, \theta | \, \rho | X_\theta, \theta \rangle \\ &= \frac{e^{-X_\theta^2}}{\sqrt{\pi}} \sum_{k,l=0}^{\infty} \frac{e^{i(k-l)\theta}}{\sqrt{2^{k+l}} k!l!} H_{k+l}(X_\theta) \mathrm{Tr}\,(a^{\dagger k} a^l \rho). \end{aligned} \tag{3.23}$$

Using the orthonormality property of the Hermite polynomials together with the identity $\sum_{u=0}^{n} e^{2\pi i u s/(n+1)} = (n+1)\delta_{s,0}$ in Eq. (3.23), we obtain

$$\begin{aligned} \langle a^{\dagger k} a^l \rangle = \mathrm{Tr}\,(a^{\dagger k} a^l \rho) = C_{kl} \sum_{m=0}^{k+l} e^{-i(k-l)m\pi/(k+l+1)} \\ \times \int_{-\infty}^{\infty} dX_\theta \; \omega\big(X_\theta, m\pi/(k+l+1)\big) H_{k+l}\,(X_\theta)\,, \end{aligned} \tag{3.24}$$

where

$$C_{kl} = \frac{k!l!}{(k+l+1)!\sqrt{2^{k+l}}}.$$

This form of the average is convenient for numerical computations from the tomogram. It is evident, here, that we are required to consider $(k+l+1)$ values of the tomogram variable θ in order to compute a moment of order $(k+l)$ from a single tomogram. Thus, the extents of squeezing and higher-order squeezing are obtained from $(k+l+1)$ probability distributions $\omega(X_\theta)$ corresponding to these values of θ. This procedure can be extended in a straightforward manner to multimode systems.

Using this procedure, we have examined the quadrature squeezing properties of the single-mode states discussed earlier in this chapter. The results are as follows: Similar to the tomographic entropy the variance in P corresponding to the ECS and the YSS is squeezed for $0 < |\alpha| < 1.5$. The squeezed vacuum and the Yuen states exhibit squeezing in the X quadrature for $0 < |\xi| < 1$ and $0.5 < |\xi| < 1$, respectively. The OCS does not exhibit squeezing in either quadrature. Comparing with the plots on entropic squeezing of these states in Fig. 3.2, it is clear that these results are consistent with the conclusion that the extent of entropic squeezing does not reflect quadrature squeezing alone, but also includes other nonclassical effects. Using Eq. (3.24), the extent of higher-order squeezing can be computed numerically in a similar fashion from the tomograms.

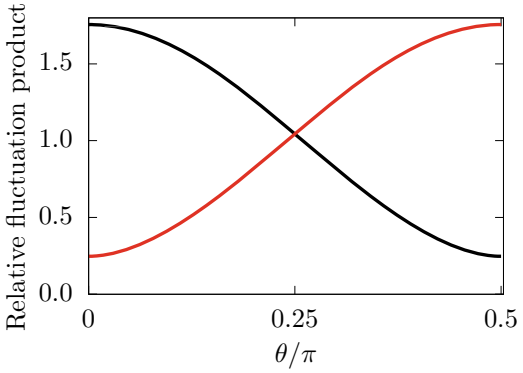

Fig. 3.3 Relative fluctuation product between the ECS and the squeezed vacuum as a function of θ, for $\alpha = \xi = 1/\sqrt{2}$. The black curve corresponds to $(\Delta X_\theta)_{\rm ECS}(\Delta X_{\theta+\frac{1}{2}\pi})_{\rm SQV}$, and the red curve to $(\Delta X_\theta)_{\rm SQV}(\Delta X_{\theta+\frac{1}{2}\pi})_{\rm ECS}$. For a similar figure with $\alpha = \xi = 1$, see [18]

The product of the relative fluctuations of Janus-faced partners exhibits specific symmetry properties. It is easy to see that for fixed values of $|\alpha|$ and $|\xi|$, the product of variances $(\Delta X_\theta)^2_{\rm ECS}(\Delta X_{\theta+\pi/2})^2_{\rm SQV}$ (the subscript SQV standing for the squeezed vacuum state) can be expressed in the form $A + B\cos 2\theta + C\cos^2 2\theta$, while the product $(\Delta X_\theta)^2_{\rm SQV}(\Delta X_{\theta+\pi/2})^2_{\rm ECS}$ has the form $A - B\cos 2\theta + C\cos^2 2\theta$, where A, B, and C are real positive constants. As a consequence of this, the square roots of these products display the 'up-down' symmetry manifest in Fig. 3.3. A similar symmetry is seen in the relative fluctuation product corresponding to the OCS and the Yuen state.

We conclude this analysis with a word of caution on two-mode squeezing. For our purpose, we consider the Caves–Schumacher and the pair-coherent states introduced in Chap. 1. A straightforward extension of Eq. (3.13) leads to

$$S_{AB}(\theta_a, \theta_b) + S_{AB}(\theta_a + \tfrac{1}{2}\pi, \theta_b + \tfrac{1}{2}\pi) \geqslant 2\,\ln(e\pi). \tag{3.25}$$

A naive extrapolation suggests that, if $S_{AB}(\theta_a, \theta_b)$ or $S_{AB}(\theta_a + \frac{1}{2}\pi, \theta_b + \frac{1}{2}\pi)$ is less than $\ln(e\pi)$, the two-mode state shows entropic squeezing. This conclusion is incorrect. In Fig. 3.4a, b, the two-mode entropy $S_{AB}(\theta_a, \theta_b)$ is plotted against the state parameter r. For $0 < r \leqslant 1$, in neither state is the two-mode entropy $S_{AB}(\theta_a, \theta_b)$ less than $\ln(e\pi)$. However, the two-mode variance shows evidence of squeezing, as in Fig. 3.4c, d. The naive extrapolation referred to above does not take into account the correlations between the two modes.

In the next chapter, we shall discuss the procedure to extract entanglement indicators for bipartite systems from optical tomograms.

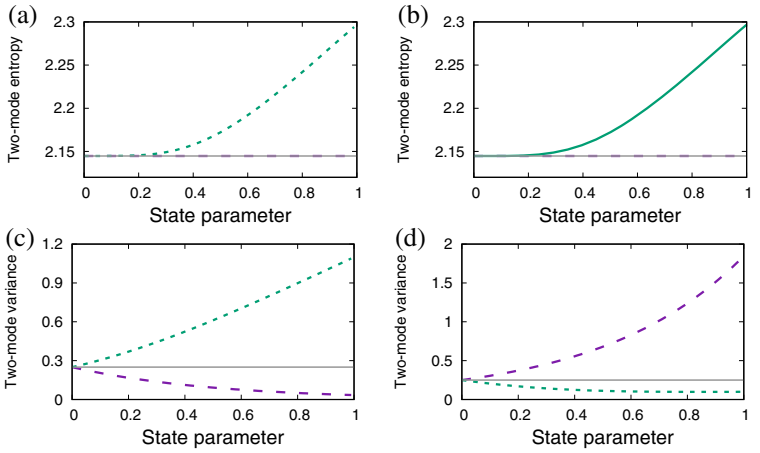

Fig. 3.4 Two-mode tomographic entropy (top panel) and variance (bottom panel) as a function of the state parameter for the Caves–Schumacher state (violet) and the pair coherent state (green). The first and the second columns correspond to $\theta_1 = \theta_2 = 0$ and $\frac{1}{2}\pi$ respectively. The horizontal lines denote the value below which squeezing occurs

References

1. G.S. Agarwal, K. Tara, Phys. Rev. A **43**, 492 (1991)
2. V.V. Dodonov, J. Opt. B Quant. Semiclass. Opt. **4**, R1 (2002)
3. L. Barsotti, J. Harms, R. Schnabel, Rep. Prog. Phys. **82**, 016905 (2019)
4. A.I. Lvovsky, *Photonics: Scientific Foundations, Technology and Applications*, vol. 1, ed. by D.L. Andrews (Wiley, New York, 2015), p. 121
5. C.K. Hong, L. Mandel, Phys. Rev. A **32**, 974 (1985)
6. M. Hillery, Phys. Rev. A **36**, 3796 (1987)
7. Z. Zhang, L. Xu, J. Chai, F. Li, Phys. Lett. A **150**, 27 (1990)
8. C. Sudheesh, S. Lakshmibala, V. Balakrishnan, J. Opt. B Quant. Semiclass. Opt. **7**, S728 (2005)
9. P.J. Coles, M. Berta, M. Tomamichel, S. Wehner, Rev. Mod. Phys. **89**, 015002 (2017)
10. H. Everett, *The Many-Worlds Interpretation of Quantum Mechanics*, ed. by B.S. Dewitt, N. Graham (Princeton University Press, Princeton, 1973), p. 52
11. L.L. Hirschman, Am. J. Math. **79**, 152 (1957)
12. I. Bialynicki-Birula, J. Mycielski, Commun. Math. Phys. **44**, 129 (1975)
13. W. Beckner, Ann. Math. **102**, 159 (1975)
14. A. Orłowski, Phys. Rev. A **56**, 2545 (1997)
15. D. Deutsch, Phys. Rev. Lett. **50**, 631 (1983)
16. M.H. Partovi, Phys. Rev. Lett. **50**, 1883 (1983)
17. R.L. Frank, E.H. Lieb, Ann. Henri Poincaré **13**, 1711 (2012)
18. P. Laha, S. Lakshmibala, V. Balakrishnan, J. Mod. Opt. **65**(12), 1466–1478 (2018). https://doi.org/10.1103/PhysRevA.92.053828
19. A. Wünsche, Phys. Rev. A **54**, 5291 (1996)
20. B. Sharmila, K. Saumitran, S. Lakshmibala, V. Balakrishnan, J. Phys. B At. Mol. Opt. **50**, 045501 (2017)

Chapter 4
Entanglement at Avoided Level Crossings

4.1 Introduction

Extensive investigations have been carried out on the manner in which the entanglement of a composite system changes as the parameters of the system are varied, both when the system is static and when it undergoes unitary evolution in time. In this chapter we focus on the former situation, and specifically examine systems where, with the variation of an appropriate parameter, some of the energy levels move close to each other and then move apart, avoiding level crossing. Studies on a range of topics from quantum critical phenomena [1, 2] to Berry phases [3] indicate that standard entanglement measures extremize at an avoided crossing. Avoided crossings are indicative of phase transitions which bring about changes in the quantum correlations in physical systems [4, 5]. This aspect has been examined widely, both in theoretical models and in experiments [6–11].

Numerous investigations on the occurrence or otherwise of energy-level crossings have been reported in the literature. The arguments in favour of the no-crossing rule [12], and its rigorous proof [13], were initially discussed primarily by molecular chemists in the context of the energy surfaces of electronic energy levels. In its original form, the rule essentially disallows crossings between the potential energy surfaces of the ground state and electronic excited states with the same symmetry, as a parameter of the system is varied. In essence, for a system with no symmetry at least two parameters must be varied to create a degeneracy.

From the point of view of semiclassical physics, more insights into level crossing were obtained by quantizing the energy levels corresponding to the phase space tori on which the classical trajectories of a Hamiltonian system lie. In particular, a naive application of the Einstein–Brillouin–Keller (EBK) quantization procedure [14] predicted that, for a Hamiltonian with a single parameter, these quantum energy levels could cross each other as the parameter was varied. However, this is only an approximate scheme (correct to $\mathcal{O}(\hbar)$), and hence in practice one expects to have an energy gap between adjacent levels for all values of the parameter.

© The Author(s), under exclusive license to Springer Nature Switzerland AG 2022

S. Lakshmibala and V. Balakrishnan, *Nonclassical Effects and Dynamics of Quantum Observables*, SpringerBriefs in Physics,
https://doi.org/10.1007/978-3-031-19414-6_4

In general, at an avoided crossing, apart from interchanges in the nature of the relevant eigenstates, new levels may also be involved, leading to permanent changes in the energy eigenstates. In strongly driven nonlinear quantum wells, avoided crossings can either lead to temporary changes in the Floquet states or (under specific conditions) delocalize them permanently, with higher harmonic generation [15]. The detailed dynamics of stimulated Raman adiabatic passage of a particle in an infinite square well subjected to two sequential laser pulses has revealed that a transition of the particle from one Floquet eigenstate to another at an isolated crossing corresponds to breaking a symmetry locally in the chaotic region of the corresponding classical phase space [16]. Since the level spacings and their probability distribution [17] are affected by the crossings, the latter also play an important role in understanding the nature of quantum chaos (see, for instance, [18]).

Connections between level repulsion as a signature of quantum chaos, avoided level crossing with changes in a single parameter, and the manner in which entanglement captures these changes, have been examined in considerable detail in the Ising model with a tilted magnetic field [19]. An interesting offshoot in the applications of avoided crossings is the attempt to obtain a tripartite entangled state, the so-called W state, as a superposition of levels that develop at avoided crossings [20].

As already mentioned, level crossings may be expected to occur in systems described by Hamiltonians with more than one parameter, or by time-dependent Hamiltonians. An early seminal result [21, 22] is that, for non-adiabatic changes in the parameter, two instantaneous levels can undergo an avoided crossing and, as a consequence, non-adiabatic tunneling between them can occur. Such intersections of energy surfaces provide the key to understanding ultrafast radiationless reactions [23].

In the light of the foregoing, a pertinent question is whether tomograms can capture entanglement changes at avoided crossings. As a first step, the question that needs to be addressed is whether qualitative signatures of bipartite entanglement are present in tomograms. This has been answered in the affirmative in Ref. [24]. These authors have examined the entangled output state when an ECS or an OCS is passed through one input port (say A) and no photon (the vacuum state $|0\rangle$) through the other input port (say B), of a 50% lossless beamsplitter as in Fig. 4.1. (Recall that the ECS and OCS are linear combinations of two CS $|\alpha\rangle$ and $|-\alpha\rangle$, with $\alpha = |\alpha|e^{i\delta}$.) The beamsplitter action itself is given by the unitary transformation

$$U_{\rm BS} = e^{\pi(a^\dagger b - a b^\dagger)/4}. \tag{4.1}$$

It is verified easily that unless the input state is a factored product of two CS, the output state is entangled. The entanglement is quantified by the subsystem von Neumann entropy (SVNE), defined in terms of the reduced density matrix ρ_i $(i = 1, 2)$ of either subsystem at the output port, as $-\mathrm{Tr}\,(\rho_i \log \rho_i)$. For $|\alpha|^2 < 10$, it has been shown that, corresponding to an input factored state of an ECS and the vacuum state, the SVNE increases from a near-zero value and saturates to its maximum possible value $(\log_2 2) = 1$, at $|\alpha|^2 \approx 6$. In contrast, if the input state is an unentangled product of

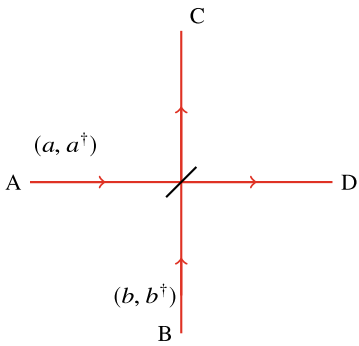

Fig. 4.1 Beamsplitter with input ports A, B and output ports C, D. $(a, a^\dagger)$, $(b, b^\dagger)$ are the photon destruction and creation operator pairs for light through the respective input ports

an OCS with the vacuum state, the output state is maximally entangled for all values of $|\alpha|^2$ in this range.

What has been exploited in Ref. [24] is the fact that a measurement in one output port will affect the state in the other, if the two-mode output is entangled. Denoting by (X_{θ_c}, θ_c) and (X_{θ_d}, θ_d) the tomogram variables for the output ports C and D respectively, it is evident that for an unentangled output, the reduced tomogram corresponding to C will be unaltered in form with variations in θ_d, and *vice versa*. In the case considered, it has been established that the reduced tomogram has a double-strand structure if $|\delta - \theta_d|$ is $\pi/2$ or $3\pi/2$, and is single-stranded for all other values except $\pi/2, 3\pi/2$, and values in their neighbourhood. (Here, δ is the phase of α.) This also shows that, apart from avoiding reconstruction of the density matrix to deduce whether a generic state is entangled or not, the number of homodyne measurements needed for the purpose is also significantly reduced.

4.2 Entanglement Indicators from Optical and Qubit Tomograms

The next issue to be addressed is whether the relevant tomograms reveal enhanced entanglement at avoided crossings, and whether it is possible to define tomographic entanglement indicators (TEIs) that quantify the extent of entanglement. It turns out that these questions can also be answered in the affirmative. In this section and the subsequent sections of this chapter, we introduce a number of bipartite entanglement quantifiers, and assess their merits in detail.

The procedure involves the identification of appropriate correlators that can be extracted from the tomogram. These quantities carry information (directly or indirectly) on the nature of bipartite entanglement in quantum systems [25]. Some of these correlators are suggested by their counterparts that are used extensively in image processing in classical systems. When they are employed to assess quantum entanglement, the results need to be compared with those obtained from standard measures such as the SVNE. This would give us some idea of the extent to which

correlations arise due to inherently quantum effects. In bipartite systems, certain correlators can be calculated from appropriate tomographic sections corresponding to definite values of θ_a and θ_b. In general, the performance of the correlator in assessing the degree of entanglement depends on the specific section that is selected. An appropriate average over the results obtained by using a sufficiently large number of such sections could also be used to estimate the overall entanglement. In what follows, we define these correlators and the entanglement indicators that can be calculated from them.

We begin with the concept of mutual information which has its origins in classical probability theory. The mutual information [26] between two continuous random variables X and Y can be expressed in terms of the Kullback–Leibler divergence D_{KL} [27] between their joint probability density $p_{XY}(x, y)$ and the product of the corresponding marginal densities $p_X(x) = \int p_{XY}(x, y)\mathrm{d}y$ and $p_Y(y) = \int p_{XY}(x, y)\mathrm{d}x$, as [28]

$$D_{\mathrm{KL}}[p_{XY} : p_X p_Y] = \int \mathrm{d}x \int \mathrm{d}y \; p_{XY}(x, y) \; \log_2 \frac{p_{XY}(x, y)}{p_X(x) p_Y(y)}. \tag{4.2}$$

We can now extrapolate the above to the quantum situation, bearing in mind that the optical tomograms are continuous probability distributions. Our starting point is the quantity

$$\varepsilon_{\mathrm{TEI}}(\theta_a, \theta_b) = S_A(\theta_a) + S_B(\theta_b) - S_{AB}(\theta_a, \theta_b), \tag{4.3}$$

where the two-mode tomographic entropy $S_{AB}(\theta_a, \theta_b)$ is expressed in terms of the two-mode tomogram $\omega(X_{\theta_a}, \theta_a; X_{\theta_b}, \theta_b)$ by

$$\begin{aligned} S_{AB}(\theta_a, \theta_b) = -\int_{-\infty}^{\infty} \mathrm{d}X_{\theta_a} \int_{-\infty}^{\infty} \mathrm{d}X_{\theta_b} \, \omega(X_{\theta_a}, \theta_a; X_{\theta_b}, \theta_b) \\ \times \log_2 \, \omega(X_{\theta_a}, \theta_a; X_{\theta_b}, \theta_b), \end{aligned} \tag{4.4}$$

and the tomographic entropies corresponding to the two subsystems are given, following Eq. (3.10), by

$$S_A(\theta_a) = -\int_{-\infty}^{\infty} \mathrm{d}X_{\theta_a} \omega_A(X_{\theta_a}, \theta_a) \log_2 \, \omega_A(X_{\theta_a}, \theta_a) \tag{4.5}$$

and similarly for $S_B(\theta_b)$. It can be identified that $\varepsilon_{\mathrm{TEI}}(\theta_a, \theta_b)$ defined in Eq. (4.3) is just the mutual information in the context of optical tomograms, since

$$\varepsilon_{\mathrm{TEI}}(\theta_a, \theta_b) = D_{\mathrm{KL}} \left[\omega(X_{\theta_a}, \theta_a; X_{\theta_b}, \theta_b) : \omega_A(X_{\theta_a}, \theta_a) \omega_B(X_{\theta_b}, \theta_b) \right]. \tag{4.6}$$

An alternative indicator is provided by the Bhattacharyya distance $D_{\rm B}$ [29] between p_{XY} and $p_X p_Y$, defined as

$$D_{\rm B}[p_{XY} : p_X p_Y] = -\log_2 \left\{ \int \mathrm{d}x \int \mathrm{d}y \, [p_{XY}(x, y) p_X(x) p_Y(y)]^{1/2} \right\}. \tag{4.7}$$

By invoking Jensen's inequality we can see that $D_{\rm B} \leqslant \frac{1}{2} D_{\rm KL}$. Hence $D_{\rm B}$ gives us an approximate estimate (actually, an underestimate) of the mutual information. Based on this quantity, an entanglement indicator that is the analog of Eq. (4.6) can be defined as follows:

$$\varepsilon_{\rm BD}(\theta_a, \theta_b) = D_{\rm B} \left[\omega(X_{\theta_a}, \theta_a; X_{\theta_b}, \theta_b) : \omega_A(X_{\theta_a}, \theta_a) \, \omega_B(X_{\theta_b}, \theta_b) \right]. \tag{4.8}$$

A popular candidate used in defining an entanglement measure, which has its origins in quantum physics, is the inverse participation ratio (IPR). Introduced in [30], the IPR is meant to quantify the extent of spatial delocalization of atomic vibrations, in a given eigenbasis $\{|\psi_i\rangle\}$ of a disordered system. Defined as $\sum_r |\psi_i(r)|^4$ where r labels the lattice sites, the IPR reveals that the localization tends to be greatest at high frequencies and near band edges. In an early paper [31] in which the average moments corresponding to eigenfunctions of a particle in a random potential near the mobility edge were examined, the IPR was used to assess delocalization. In simple terms, if the system considered is a lattice with N_0 sites, and the wave function corresponding to the ith eigenstate spreads over m sites with equal amplitude, then $|\psi_i(r)|^2 = 1/m$ on these sites, and vanishes elsewhere. For normalized wave functions this implies that the corresponding IPR is $1/m$. This is interpreted as the reciprocal of the number of orbitals contributing to the state. If the state is confined to a single orbital, the IPR is equal to its maximum value of unity. In general, as $N_0 \to \infty$, the IPR tends to zero. In the context of complex quantum systems, a generalized version of entanglement has been examined, and the purity of the system compared with delocalization measures such as the IPR [32]. For a bipartite CV system, the IPR is defined as

$$\eta_{AB}(\theta_a, \theta_b) = \int_{-\infty}^{\infty} \mathrm{d}X_{\theta_a} \int_{-\infty}^{\infty} \mathrm{d}X_{\theta_b} \left[\omega(X_{\theta_a}, \theta_a; X_{\theta_b}, \theta_b) \right]^2. \tag{4.9}$$

The corresponding IPR for subsystem A is given by

$$\eta_A(\theta_a) = \int_{-\infty}^{\infty} \mathrm{d}X_{\theta_a} \left[\omega_A(X_{\theta_a}, \theta_a) \right]^2, \tag{4.10}$$

and a similar definition holds for subsystem B. The entanglement indicator in this case is given by

$$\varepsilon_{\rm IPR}(\theta_a, \theta_b) = 1 + \eta_{AB}(\theta_a, \theta_b) - \eta_A(\theta_a) - \eta_B(\theta_b). \tag{4.11}$$

Another classical correlator in terms of which an entanglement indicator can be defined is the Pearson correlation coefficient (PCC) between two random variables X and Y [33]. It turns out, however, that this correlator is only very moderately effective in assessing entanglement. It primarily captures linear correlations between two states, as it is defined solely in terms of the variances and covariance of conjugate pairs of dynamical variables. In atomic systems such as hydrogen, for instance, the spreads in appropriate conjugate variables can be used to obtain a rough estimate of the entanglement between the electron in a specific state of orbital angular momentum and the proton [34, 35]. Further, in recent experiments on generating and testing the entanglement in certain CV systems, variances of appropriate quantities alone have been used [36]. We define this entanglement indicator below.

The Pearson correlation coefficient between two random variables X and Y is

$$\mathrm{PCC}(X, Y) = \frac{\mathrm{Cov}\,(X, Y)}{(\Delta X)(\Delta Y)}, \tag{4.12}$$

where the standard deviations of X and Y are denoted by ΔX and ΔY respectively. Their covariance is denoted by $\mathrm{Cov}\,(X, Y)$. We now define an entanglement indicator in terms of $\mathrm{PCC}\,(X_{\theta_a}, X_{\theta_b})$ calculated for fixed values of θ_a and θ_b. A simple definition of a non-negative quantity that could serve to assess entanglement is given by

$$\varepsilon_{\mathrm{PCC}}(\theta_a, \theta_b) = |\mathrm{PCC}\,(X_{\theta_a}, X_{\theta_b})|. \tag{4.13}$$

We emphasize that this indicator is not, in general, a reliable one for determining the extent of bipartite entanglement in the quantum context.

Corresponding to each of the ε-indicators defined above in terms of specific tomographic sections (i.e., specific choices of θ_a and θ_b), we can also define entanglement indicators that are independent of such choices. We shall refer to these as ξ-indicators. In each case, the latter is obtained by averaging over an adequate number of values of the corresponding ε-indicator. We recall that in the double-well BEC system, the indicator ξ_{TEI} was obtained by averaging over 25 such sections spread out uniformly in the range $[0, \pi)$. While the number of sections that need to be considered for obtaining reliable averaged quantities, will vary depending on the system considered, this procedure can be used to calculate ξ_{IPR}, ξ_{PCC} and ξ_{BD}, respectively from $\varepsilon_{\mathrm{IPR}}$, $\varepsilon_{\mathrm{PCC}}$ and $\varepsilon_{\mathrm{BD}}$.

4.3 Entanglement Indicators and Squeezing in Spin Systems

The entanglement indicators for spin-$\frac{1}{2}$ systems (or two-level atoms) can be extracted from appropriate tomograms. For instance, denoting the energy eigenstates of a two-level atom by $|g\rangle$ (the ground state) and $|e\rangle$ (the excited state), the relevant observables are [37]

$$\left.\begin{aligned}\sigma_x &= \tfrac{1}{2}(|e\rangle\langle g| + |g\rangle\langle e|),\\ \sigma_y &= \tfrac{1}{2}i(|g\rangle\langle e| - |e\rangle\langle g|),\\ \sigma_z &= \tfrac{1}{2}(|e\rangle\langle e| - |g\rangle\langle g|).\end{aligned}\right\} \tag{4.14}$$

Let $\sigma_z|m\rangle = m|m\rangle$. We define the state $|\vartheta, \varphi, m\rangle = U(\vartheta, \varphi)|m\rangle$, where

$$U(\vartheta, \varphi) = \begin{pmatrix} \cos\left(\frac{\vartheta}{2}\right) e^{i\varphi/2} & \sin\left(\frac{\vartheta}{2}\right) e^{i\varphi/2} \\ -\sin\left(\frac{\vartheta}{2}\right) e^{-i\varphi/2} & \cos\left(\frac{\vartheta}{2}\right) e^{-i\varphi/2} \end{pmatrix}. \tag{4.15}$$

Denoting (ϑ, φ) by the unit vector $\mathbf{n}$, a two-level tomogram is given by

$$\omega(\mathbf{n}, m) = \langle \mathbf{n}, m|\, \rho_{\mathrm{S}}|\mathbf{n}, m\rangle \tag{4.16}$$

where ρ_{S} is the density matrix. Analogous to optical tomograms, a complete set of basis states exist for each value of $\mathbf{n}$. It is straightforward to define (by drawing parallels with optical tomograms) both bipartite atomic tomograms and corresponding entanglement indicators, by appropriate adaptation of definitions in the CV case, as shown below. (Integrals of course, are replaced by appropriate sums.)

The definitions can be extended to bipartite entanglement in multipartite systems, in a straightforward manner [38]. The bipartite spin tomogram is given by

$$\omega(\mathbf{n}_A, m_A; \mathbf{n}_B, m_B) = \langle \mathbf{n}_A, m_A; \mathbf{n}_B, m_B|\rho_{AB}|\mathbf{n}_A, m_A; \mathbf{n}_B, m_B\rangle, \tag{4.17}$$

where ρ_{AB} is the bipartite density matrix, $\sigma_{iz}|m_i\rangle = m_i|m_i\rangle$ $(i = A, B)$, and $|\mathbf{n}_A, m_A; \mathbf{n}_B, m_B\rangle$ stands for $|\mathbf{n}_A, m_A\rangle \otimes |\mathbf{n}_B, m_B\rangle$. The normalization condition is given by

$$\sum_{m_A}\sum_{m_B} \omega(\mathbf{n}_A, m_A; \mathbf{n}_B, m_B) = 1 \tag{4.18}$$

for each $\mathbf{n}_A$ and $\mathbf{n}_B$. The reduced tomograms for the subsystems A and B are

$$\omega_A(\mathbf{n}_A, m_A) = \langle \mathbf{n}_A, m_A|\rho_A|\mathbf{n}_A, m_A\rangle = \sum_{m_B} \omega(\mathbf{n}_A, m_A; \mathbf{n}_B, m_B) \tag{4.19}$$

for any fixed value of $\mathbf{n}_B$, and

$$\omega_B(\mathbf{n}_B, m_B) = \langle \mathbf{n}_B, m_B|\rho_B|\mathbf{n}_B, m_B\rangle = \sum_{m_A} \omega(\mathbf{n}_A, m_A; \mathbf{n}_B, m_B) \tag{4.20}$$

for any fixed value of $\mathbf{n}_A$. The reduced density matrices ρ_A and ρ_B are given by $\mathrm{Tr}_B\,(\rho_{AB})$ and $\mathrm{Tr}_A\,(\rho_{AB})$, respectively.

In contrast to optical tomograms, the spin tomograms are more conveniently plotted as color maps. Each map represents a (9×4) matrix. This is because the

nine possibilities xx, xy, etc., are marked on the vertical axis. Here, the first (resp. second) label refers to subsystem A (resp. B). The four outcomes corresponding to each basis are 00, 01, 10 and 11, where 0 and 1 refer to $m = -\frac{1}{2}$ and $m = +\frac{1}{2}$ respectively.

The simplest spin tomograms correspond to a bipartite spin coherent state, parametrized by angles θ, ϕ (where $0 \leqslant \theta \leqslant \pi,\ 0 \leqslant \phi < 2\pi$), given by

$$\begin{aligned}&\left[\cos(\theta/2)\,|\uparrow\rangle_A + e^{i\phi}\ \sin(\theta/2)\,|\downarrow\rangle_A\right]\\ &\quad\otimes\left[\cos(\theta/2)\,|\uparrow\rangle_B + e^{i\phi}\ \sin(\theta/2)\,|\downarrow\rangle_B\right].\end{aligned} \tag{4.21}$$

Figure 4.2a–d[1] show the tomograms for four different values of θ and ϕ. The bipartite tomographic entropy and the entanglement indicators for spin/qubit systems can now be defined analogous to those given earlier for CV systems. In this case, the entropy is

$$\begin{aligned}S(\mathbf{n}_A, \mathbf{n}_B) = &-\sum_{m_A}\sum_{m_B}\omega(\mathbf{n}_A, m_A; \mathbf{n}_B, m_B)\\ &\times \log_2\,\omega(\mathbf{n}_A, m_A; \mathbf{n}_B, m_B).\end{aligned} \tag{4.22}$$

The tomographic entropy for a specific subsystem is

$$S(\mathbf{n}_i) = -\sum_{m_i}\omega_i(\mathbf{n}_i, m_i)\log_2\left[\omega_i(\mathbf{n}_i, m_i)\right]\ \ (i = A, B). \tag{4.23}$$

Analogous to the case of CV systems, correlators and entanglement indicators can be defined for specific tomographic sections, or by using the averaging prescription given earlier. The latter provides section-independent indicators. These are described below. The mutual information is

$$\varepsilon_{\mathrm{TEI}}(\mathbf{n}_A, \mathbf{n}_B) = S(\mathbf{n}_A) + S(\mathbf{n}_B) - S(\mathbf{n}_A, \mathbf{n}_B), \tag{4.24}$$

and is expressed in terms of the Kullback–Leibler divergence as

$$\varepsilon_{\mathrm{TEI}}(\mathbf{n}_A, \mathbf{n}_B) = D_{\mathrm{KL}}\left[\omega(\mathbf{n}_A, m_A; \mathbf{n}_B, m_B) : \omega_A(\mathbf{n}_A, m_A)\omega_B(\mathbf{n}_B, m_B)\right]. \tag{4.25}$$

In the spin basis, the IPR for the bipartite system is defined as

$$\eta_{AB}(\mathbf{n}_A, \mathbf{n}_B) = \sum_{m_A}\sum_{m_B}\left[\omega(\mathbf{n}_A, m_A; \mathbf{n}_B, m_B)\right]^2. \tag{4.26}$$

[1] Figure 4.2 is reproduced from *Tomographic entanglement indicators from NMR experiments*, Sharmila et al. [39] with permission from AIP Publishing.

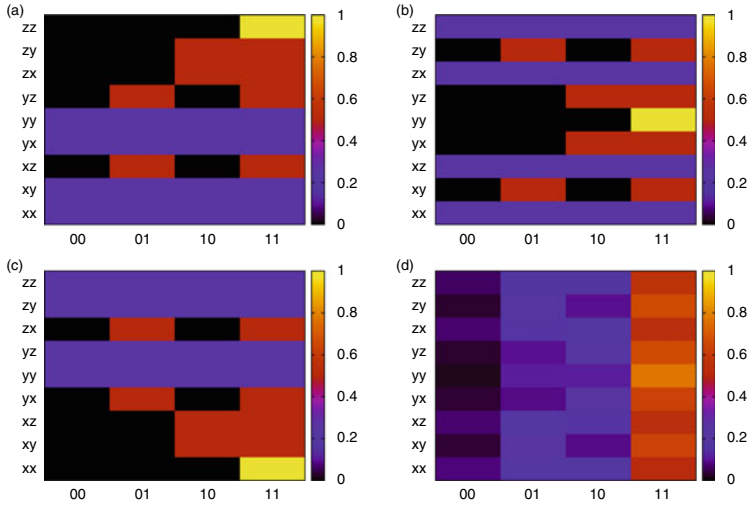

Fig. 4.2 Tomograms of spin coherent states with (θ, ϕ) equal to **a** $(0, 0)$, **b** $(\pi/2, \pi/2)$, **c** $(\pi/2, 0)$, and **d** $(\pi/3, \pi/3)$. The bases are denoted by x, y and z and the outcomes by 0 and 1. Figures are reproduced from [39]

The IPR for each subsystem is

$$\eta_i(\mathbf{n}_i) = \sum_{m_i} [\omega_i(\mathbf{n}_i, m_i)]^2 \quad (i = A, B). \tag{4.27}$$

The corresponding entanglement indicator

$$\varepsilon_{\text{IPR}}(\mathbf{n}_A, \mathbf{n}_B) = 1 + \eta_{AB}(\mathbf{n}_A, \mathbf{n}_B) - \eta_A(\mathbf{n}_A) - \eta_B(\mathbf{n}_B). \tag{4.28}$$

The Pearson correlation coefficient $\text{PCC}(m_A, m_B)$ is now calculated for specific values of $\mathbf{n}_A$ and $\mathbf{n}_B$. An entanglement indicator based on this coefficient in the case of qubit systems is

$$\varepsilon_{\text{PCC}}(\mathbf{n}_A, \mathbf{n}_B) = |\text{PCC}(m_A, m_B)|. \tag{4.29}$$

It is expected that $\varepsilon_{\text{PCC}}(\mathbf{n}_A, \mathbf{n}_B)$ will only capture the effect of linear correlations, as in the context of CV systems.

We now move on to revisit the Bhattacharyya distance in the spin context. Analogous to Eq. (4.8), a straightforward definition of the corresponding entanglement indicator is

$$\varepsilon_{\text{BD}}(\mathbf{n}_A, \mathbf{n}_B) = D_{\text{B}}[\omega(\mathbf{n}_A, m_A; \mathbf{n}_B, m_B) : \omega_A(\mathbf{n}_A, m_A)\omega_B(\mathbf{n}_B, m_B)]. \tag{4.30}$$

The mean values of $\varepsilon_{\rm TEI}$, $\varepsilon_{\rm IPR}$, $\varepsilon_{\rm PCC}$ and $\varepsilon_{\rm BD}$ obtained by averaging over the 9 possible values corresponding to the 3 orthogonal vectors for each of the $\mathbf{n}_i$, $i = A, B$, provide section-independent indicators, as before. These will be denoted by $\xi_{\rm TEI}$, $\xi_{\rm IPR}$, $\xi_{\rm PCC}$ and $\xi_{\rm BD}$, respectively.

As mentioned in Chap. 1, in generic multipartite spin systems comprising entangled subsystems, spin squeezing is related to the entanglement [40]. A commonly used procedure in the literature to quantify spin squeezing is given in [41]. This is outlined below. Consider a collection of N subsystems each having spin equal to half. The reference state for spin squeezing is the spin coherent state created out of these N spins. Its variance can be seen to be equal to $N/4$. If one of the components orthogonal to the mean spin vector of the system has a variance less than $N/4$, squeezing occurs.

For illustrative purposes, consider $N = 2$. The mean spin vector in this case is $\mathbf{v}_{\rm s}(t) = \langle \mathbf{J}_2(t)\rangle/|\langle \mathbf{J}_2(t)\rangle|$ where

$$\mathbf{J}_2 = (\sigma_{Ax} + \sigma_{Bx})\mathbf{e}_x + (\sigma_{Ay} + \sigma_{By})\mathbf{e}_y + (\sigma_{Az} + \sigma_{Bz})\mathbf{e}_z. \tag{4.31}$$

Here, $\langle \mathcal{O}(t)\rangle = {\rm Tr}_{AB}\,[\rho_{AB}(t)\mathcal{O}]$ for any operator $\mathcal{O}$, and $\rho_{AB}(t)$ is the density matrix of the full system at time t. We consider an ensemble of vectors $\{\mathbf{v}_\perp\}$ each of which satisfies $\mathbf{v}_\perp \cdot \mathbf{v}_s = 0$ at each instant. Then,

$$(\Delta\ \mathbf{J}_2{\cdot}\mathbf{v}_\perp)^2 = \langle(\mathbf{J}_2{\cdot}\mathbf{v}_\perp)^2\rangle \tag{4.32}$$

is first calculated as a function of time. The next part of the procedure is to identify the corresponding minimum variance $(\Delta J_{\rm min})^2$ at every such instant. This quantifies the extent of spin squeezing as a function of time.

Another procedure is to estimate squeezing from tomograms alone, as described in Chap. 3 for CV systems. The outcomes of both the methods will be the same. This reaffirms the utility of tomograms. In the latter case, variances are calculated from any spin tomogram by expressing $(\Delta\ \mathbf{J}_2{\cdot}\mathbf{v}_\perp)^2$ in terms of quantities that are readily obtained from the latter. For this, we note that if we use the commutator algebra for spins, $(\mathbf{J}_2{\cdot}\mathbf{v}_\perp)^2$ involves either terms that are linear in the σ's, such as σ_{By}, or are products such as $\sigma_{Ay}\sigma_{Bx}$. The required expectation values can be readily obtained. As an example, we have $\langle\sigma_{Ax}\rangle = \sum_{m_A,m_B} m_A\,\omega(\mathbf{e}_x, m_A; \mathbf{e}_y, m_B)$, while $\langle\sigma_{Ax}\sigma_{By}\rangle = \sum_{m_A,m_B} m_A m_B\,\omega(\mathbf{e}_x, m_A; \mathbf{e}_y, m_B)$.

The foregoing procedure for estimating spin squeezing can also be extended to estimate second-order squeezing. The relevant object in this case is the expectation value of the dyad $\mathbf{J}_2\mathbf{J}_2$ instead of $\langle\mathbf{J}_2\rangle$. In general, the former is not a null tensor. The orthogonality condition is now given by $\langle\mathcal{J}\rangle = 0$, where

$$\mathcal{J} = \frac{1}{2}\left(\mathbf{u}_\perp \cdot \mathbf{J}_2\mathbf{J}_2 \cdot \mathbf{v}_\perp + \mathbf{v}_\perp \cdot \mathbf{J}_2\mathbf{J}_2 \cdot \mathbf{u}_\perp\right). \tag{4.33}$$

$\mathbf{u}_\perp$ and $\mathbf{v}_\perp$ are analogous to the vector $\mathbf{v}_\perp$ in the previous case. As a consequence of the symmetrization with respect to $\mathbf{u}_\perp$ and $\mathbf{v}_\perp$ in Eq. (4.33), $\mathcal{J}$ is real. To compute the

extent of squeezing, a set of several different pairs $(\mathbf{u}_\perp, \mathbf{v}_\perp)$ for which $\langle \mathcal{J}(t) \rangle = 0$, are considered. For each such pair, the variance $(\Delta \mathcal{J})^2$ is computed, and from this the minimum variance $(\Delta \mathcal{J})^2_{\rm min}$ is obtained. Since the corresponding variance of the spin coherent state, obtained by minimizing with respect to θ and ϕ is $= 0.125$, any state is second-order squeezed if its variance is less than this value.

Returning to the problem at hand, we proceed to consider avoided energy level crossings in generic CV and HQ models, in the following two sections. The details of these investigations are presented in Ref. [25].

4.4 Bipartite CV Models and Avoided Level Crossings

We begin with an estimate of the performance of the various entanglement indicators near avoided energy-level crossings in the double-well BEC system. We recall that (setting $\hbar = 1$) the Hamiltonian for this system is given by Eq. (2.53), namely,

$$H_{\rm BEC} = \omega_0 \mathsf{N}_{\rm tot} + \omega_1 (a^\dagger a - b^\dagger b) + u_0 \mathsf{N}_{\rm tot}^2 - \lambda (a^\dagger b + a b^\dagger), \tag{4.34}$$

where $(a, a^\dagger)$ and $(b, b^\dagger)$ are the respective boson annihilation and creation operators of the atoms in the two wells A and B. $\mathsf{N}_{\rm tot} = (a^\dagger a + b^\dagger b)$, and u_0 is the strength of both the inter-atomic and intra-atomic nonlinear interactions. The energy spectrum is bounded from below, as only positive values of u_0 are considered. The linear interaction strength is λ, and ω_1 is the strength of the population imbalance between the two wells. The unitary transformation $V = e^{\kappa_0 (a^\dagger b - b^\dagger a)/2}$ with $\kappa_0 = \tan^{-1}(\lambda/\omega_1)$ gives

$$V^\dagger H_{\rm BEC} V = \widetilde{H}_{\rm BEC} = \omega_0 \mathsf{N}_{\rm tot} + \lambda_1 (a^\dagger a - b^\dagger b) + u_0 \mathsf{N}_{\rm tot}^2, \tag{4.35}$$

where $\lambda_1 = (\lambda^2 + \omega_1^2)^{1/2}$. $\widetilde{H}_{\rm BEC}$ and $\mathsf{N}_{\rm tot}$ have a complete set of common eigenstates, as they commute with each other. These are [42] the factored product states $|k\rangle \otimes |N-k\rangle \equiv |k; N-k\rangle$, $N = 0, 1, 2, \ldots$ being the eigenvalue of $\mathsf{N}_{\rm tot}$. The boson number state is denoted by $|k\rangle$, k taking values from 0 to N for a given N. It can be verified that the eigenstates of $H_{\rm BEC}$ are given by

$$|\psi_{N,k}\rangle = V |k; N-k\rangle. \tag{4.36}$$

The corresponding eigenvalues are

$$E(N,k) = \omega_0 N + \lambda_1 (2k - N) + u_0 N^2. \tag{4.37}$$

In the numerical analysis that follows we set $\omega_0 = 1$, $u_0 = 1$.

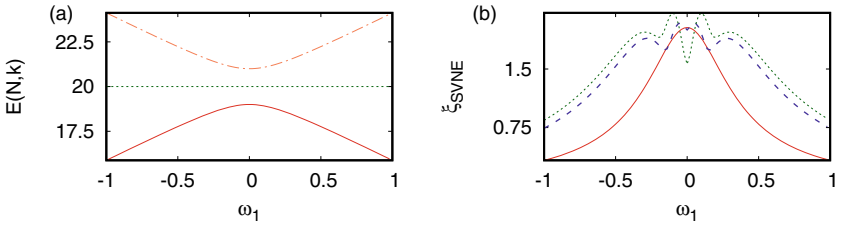

Fig. 4.3 **a** $E(N, k)$ versus ω_1 for $N = 4$ and $k = 0, 2, 4$ in the BEC model. **b** ξ_{SVNE} versus ω_1 for $N = 4$, $k = 0, 1, 2$. The curves correspond to $k = 0$ (red), 1 (blue), 2 (green) and 4 (orange). $\lambda = 0.25$. Figures are reproduced from [25]

Figure[2] 4.3a is a plot of $E(N = 4, k)$ versus ω_1 for $k = 0, 2, 4$, with $\lambda = 0.25$. $E(N, N - k)$ is the reflection of $E(N, k)$ about the value $\omega_0 N + u_0 N^2$. At $\omega_1 = 0$, there are avoided energy-level crossings. The entanglement measure which is used in the analysis to set the reference level is ξ_{SVNE}. Since $|\psi_{N,k}\rangle$ is a bipartite pure state, $\xi_{\text{SVNE}} = -\text{Tr}(\rho_i \log_2 \rho_i)$, where ρ_i is the density matrix corresponding to either subsystem A or B.

In Fig. 4.3b, plots of ξ_{SVNE} corresponding to the state $|\psi_{4,k}\rangle$ for $k = 0, 1, 2$ are shown. It is clear that the states $|\psi_{4,3}\rangle$ and $|\psi_{4,1}\rangle$ have the same ξ_{SVNE}, as also the states $|\psi_{4,4}\rangle$ and $|\psi_{4,0}\rangle$. This feature can be traced to the $k \leftrightarrow N - k$ symmetry. Close to the avoided energy-level crossing there is considerable entanglement, and ξ_{SVNE} has a local extremum at $\omega_1 = 0$.

Figure 4.4 depicts tomographic sections $\theta_a = 0$, $\theta_b = \frac{1}{2}\pi$, corresponding to $|\psi_{4,k}\rangle$ for $k = 0, 1, 2$ and $\omega_1 = 0, 0.1, 1$. It is evident from these sections that, for fixed ω_1, the qualitative features of the tomograms change considerably as k is varied. The top panel reveals nonlinear correlations between X_{θ_a} and X_{θ_b}. Compare, for instance, the sections in the top right and left corners. The former section corresponds to a probability distribution that is symmetric about the origin, and is essentially unimodal. Further, the annular structures are diminished in magnitude. The latter section is more correlated.

This is consistent with the inference on the extent of entanglement that we can draw from Fig. 4.3b, by comparing ξ_{SVNE} corresponding to $k = 0$ and $k = 2$ at $\omega_1 = 0$. Similar conclusions can be drawn by examining the sections in the bottom panel, and comparing the conclusions drawn with those from the entanglement trends in Fig. 4.3b. It can be verified that for generic cases, ε_{TEI} and ξ_{TEI} are better entanglement indicators than ε_{PCC} and ξ_{PCC}. It can be verified that for generic eigenstates of H_{BEC}, the indicators ξ_{TEI} and ξ_{IPR} follow the trends in ξ_{SVNE} reasonably well. This is illustrated in Fig. 4.5 for the eigenstate $|\psi_{4,2}\rangle$.

A procedure carried out in [25] to quantify the performance of the tomographic entanglement indicators involves evaluating the Pearson correlation coef-

[2] Figures 4.3, 4.4, 4.5 and 4.6 are reproduced from *Signatures of avoided energy-level crossings in entanglement indicators obtained from quantum tomograms*, Sharmila et al. [25] with permission from IOP Publishing.

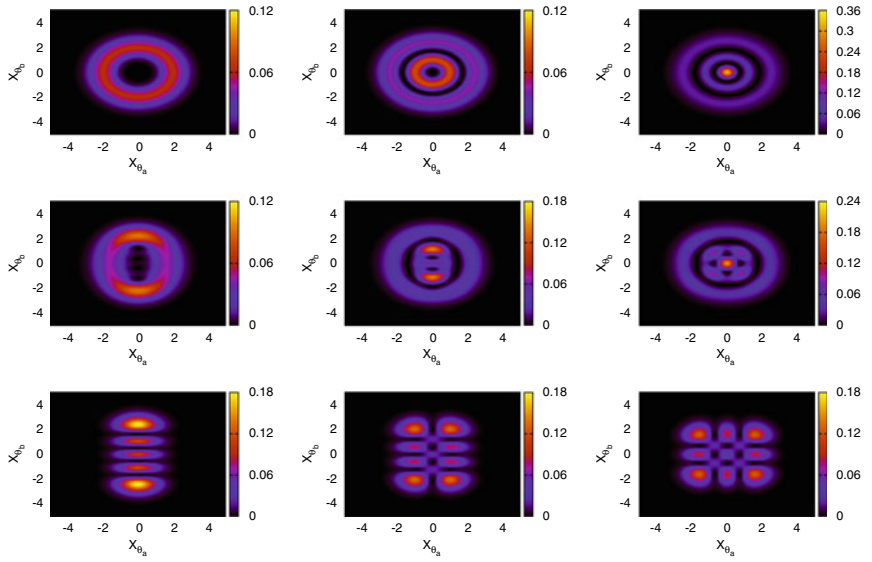

Fig. 4.4 $\theta_a = 0, \theta_b = \pi/2$ slice of the tomogram for $N = 4$ in the BEC model. Left to right, $k = 0$, 1 and 2. Top to bottom, $\omega_1 = 0$, 0.1 and 1. Figures are reproduced from [25]

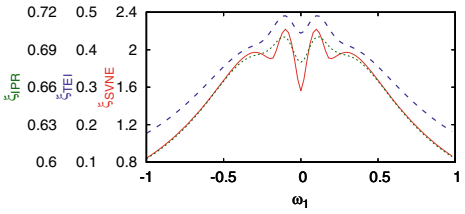

Fig. 4.5 ξ_{SVNE} (red), ξ_{TEI} (blue) and ξ_{IPR} (green) versus ω_1, for the state $|\psi_{4,2}\rangle$ in the BEC model. This figure is reproduced from [25]

ficient between each indicator and ξ_{SVNE}, for several eigenstates. This reveals the following: (a) All three indicators, namely, ξ_{IPR}, ξ_{TEI} and ξ_{BD}, perform well in this model. (b) They fare better with increasing N. (c) As expected, the performance of any ε-indicator depends on the specific tomographic section. (d) ξ_{PCC} itself does not perform well. (e) Further, the efficacy of all the indicators decreases as λ increases. We emphasize that, on the whole, ξ_{IPR} fares better than the other tomographic indicators, in the sense that it is closest to ξ_{SVNE}. This fact is consistent with conclusions [43] drawn about the relation between the Hamming distance [44] and the efficacy of ξ_{IPR}. The Hamming distance between two bipartite qudits $|u_1\rangle \otimes |u_2\rangle$ and $|v_1\rangle \otimes |v_2\rangle$ is maximum (equal to 2) when $\langle u_i|v_i\rangle = 0$ $(i = 1, 2)$. A straightforward extension of this concept to CV systems, implies that the Hamming distance between $|k_1; N - k_1\rangle$ and $|k_2; N - k_2\rangle$ is 2 since these states are Hamming-uncorrelated, if $k_1 \neq k_2$. It has been demonstrated [32] that participation ratios are good quantifiers of entanglement between superpositions of Hamming-uncorrelated states in spin systems. We see that the eigenstates $|\psi_{N,k}\rangle$ are superpositions of the states $\{|j; N - j\rangle\}$ which

are Hamming-uncorrelated for different values of j. Hence, $\xi_{\rm IPR}$ fares well as an entanglement indicator even for larger values of λ.

We now summarize the results of investigations on another CV model, namely, a multilevel atom (modeled by an anharmonic oscillator) that is linearly coupled with strength g to a radiation field of frequency ω_F. In this case the precise nature of the nonlinearity is different from that of the double-well BEC system. This model has been extensively investigated in [45]. The effective Hamiltonian is given by

$$H_{\rm AF} = \omega_F a^\dagger a + \omega_A b^\dagger b + \gamma {b^\dagger}^2 b^2 + g(a^\dagger b + a b^\dagger). \tag{4.38}$$

The constants ω_A and γ are strictly positive, for stability. $(a, a^\dagger)$ and $(b, b^\dagger)$ are the annihilation and creation operators for the field mode and the oscillator mode, respectively. As before, $\mathsf{N}_{\rm tot} = a^\dagger a + b^\dagger b$ and $[H_{\rm AF}, \mathsf{N}_{\rm tot}] = 0$. This system displays rich entanglement dynamics during unitary evolution. We will discuss this aspect in detail in a subsequent chapter. In the context of avoided energy-level crossings, however, it suffices to state that, in this model, investigations of the performance of entanglement indicators carried out along lines similar to those on the BEC system lead to the same conclusions. With an increase in γ, the efficacy of all the indicators is marginally decreased.

4.5 Avoided Crossings in Multipartite HQ Systems: The Tavis–Cummings Model

In order to get a complete picture of the quality of tomographic indicators in the absence of temporal evolution of the system considered, we now examine a generic hybrid quantum system comprising several qubits interacting with each other and also with an external field with inherent nonlinearities. Two well known examples of such systems are two-level atoms with nearest-neighbor couplings interacting with quantized light in the presence of a Kerr-like nonlinearity, and a superconducting chain of M qubits interacting with an external microwave field with frequency Ω_F (see [46, 47]). In the literature, Tavis–Cummings models [48] are used to describe such systems. The Hamiltonian for superconducting qubits subject to the external field mentioned above is given (for $\hbar = 1$) by

$$\begin{aligned} H_{\rm TC} = {} & \Omega_F a^\dagger a + \chi {a^\dagger}^2 a^2 + \sum_{p=1}^{M} \Omega_p \sigma_{pz} + \Lambda(a^\dagger \sigma_p^- + a\sigma_p^+) \\ & + \sum_{p=1}^{M-1} \Lambda_s \left(\sigma_p^- \sigma_{(p+1)}^+ + \sigma_{(p+1)}^- \sigma_p^+ \right). \end{aligned} \tag{4.39}$$

Here, χ is the strength of the field nonlinearity, Λ is the coupling strength between the field and each of the M qubits, $\sigma_p^\pm$ are the ladder operators of the pth qubit, and Λ_s is

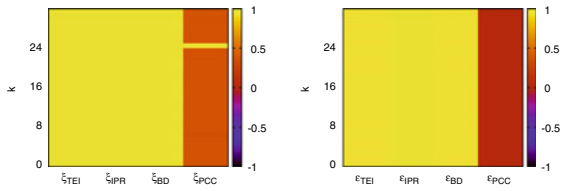

Fig. 4.6 Correlation of ξ_{SVNE} with ξ-indicators (left) and with ε-indicators for the slice corresponding to $\theta = \pi/2$ for the field, and the σ_x basis for each qubit (right) for different values of Λ. The figures are for the eigenstates $|\psi_{5,6,k}\rangle$, $0 \leqslant k \leqslant 2^5 - 1$ in Case (i) in the Tavis–Cummings model. Figures are reproduced from [25]

the strength of the interaction between nearest-neighbor qubits. $\Omega_p = (\Delta_p^2 + \epsilon^2)^{1/2}$ is the energy difference between the two levels of the pth qubit, where Δ_p is the inherent excitation gap and ϵ is the detuning of the external magnetic flux from the flux quantum $h/(2e)$. The experimentally relevant parameter values, namely, $\Omega_F/(2\pi) = 7.78\,\text{GHz}$ and $\epsilon/(2\pi) = 4.62\,\text{GHz}$, are used in numerical computations. The level separations Δ_p of the individual qubits are drawn from a Gaussian distribution, whose mean $\langle\Delta\rangle/(2\pi) = 5.6\,\text{GHz}$ and standard deviation is $0.2\,\langle\Delta\rangle$. The bipartite system in this case, has the field subsystem and another subsystem comprising all the qubits. The performance of each entanglement indicator is assessed by calculating the Pearson correlation coefficient between the indicator and the SVNE, both in the absence and in the presence of disorder. Since this facilitates obtaining a clear picture about their performance, we explain this calculation in some detail in what follows.

First, we observe that the total number operator

$$\mathcal{N}_{\text{tot}} = a^\dagger a + \sum_{p=1}^{M} \sigma_p^+ \sigma_p^-, \tag{4.40}$$

commutes with H_{TC}. For each value of Λ, numerical solutions for the complete set $\{|\psi_{M,N,k}\rangle\}$ of common eigenstates of $\mathcal{N}_{\text{tot}}$ and H_{TC} are obtained. Here $N = 0, 1, \ldots$ is the eigenvalue of $\mathcal{N}_{\text{tot}}$ and $k = 0, 1, \ldots, 2^M - 1$. Three cases are of relevance. (i) $\Lambda_s = \chi = 0$, (ii) $\Lambda_s/(2\pi) = 1\,\text{MHz}$, $\chi = 0$ and (iii) $\Lambda_s/(2\pi) = \chi/(2\pi) = 1\,\text{MHz}$. In the computation, $\Lambda/(2\pi)$ is varied from -1.2 to $1.3\,\text{MHz}$ in steps of $0.025\,\text{MHz}$. For illustrative purposes, the correlation between the indicators and ξ_{SVNE} in Case (i) are shown in Fig. 4.6. The corresponding Pearson correlation coefficients are, correct to two decimal places, 0.97 for ε_{TEI}, 0.99 for ε_{IPR}, and 0.97 for ε_{BD}. (The accuracy of the ε-indicators depends, of course, on the basis chosen.) Averaging over the ε-indicators, the corresponding ξ-indicators are obtained. The PCC in this case is 0.99, which implies that these indicators follow ξ_{SVNE} very closely. Similar investigations carried out in the other two cases corroborate these results.

The role of disorder is examined by setting $\Lambda/(2\pi)$ equal to $1.2\,\text{MHz}$, and then changing the strength of the disorder in Ω_p by varying the standard deviation of Δ_p from 0 to $0.2\,\langle\Delta\rangle$ in steps of $2 \times 10^{-4}\,\langle\Delta\rangle$. Calculation of the entanglement

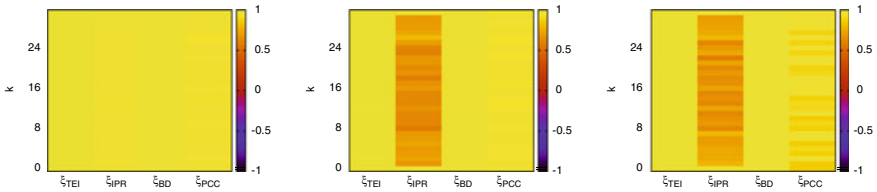

Fig. 4.7 Correlation between ξ_{SVNE} and ξ-indicators for different values of disorder strength and eigenstates $|\zeta_{5,6,k}\rangle\, 0 \leqslant k \leqslant 2^5 - 1$. Left to right, Cases (i), (ii) and (iii) respectively in the Tavis–Cummings model

indicators for each disorder strength in Ω_p, reveals that ξ_{TEI} and ξ_{BD} are significantly closer to ξ_{SVNE}, and hence are more accurate indicators of entanglement, than ξ_{IPR} and ξ_{PCC} (see Fig. 4.7).

In summary, an investigation of the merits of various tomographic entanglement indicators reveals that in generic bipartite CV systems where total number is conserved, the nonlinear correlation between the quadratures of the subsystems are reliable quantifiers of bipartite entanglement. In the case of energy eigenstates which are superpositions of Hamming-uncorrelated states, both ξ_{IPR} and ε_{IPR} perform very well near avoided crossings. Again, in the vicinity of avoided crossings, both ξ_{TEI} and ξ_{BD} are also reliable indicators that closely follow the SVNE. As $\langle \mathsf{N}_{\text{tot}} \rangle$ increases, all entanglement indicators seem to perform better. Similar conclusions can be drawn from investigations on generic HQ systems. The advantages of using these indicators to assess entanglement are evident, as they do not depend on a knowledge of the density matrix. In Chap. 5, we examine the performance of tomographic entanglement indicators during temporal evolution of bipartite CV systems.

References

1. G. Vidal, J.I. Latorre, E. Rico, A. Kitaev, Phys. Rev. Lett. **90**, 227902 (2003)
2. M. Vojta, Rep. Prog. Phys. **66**, 2069 (2003)
3. S. Oh, Z. Huang, U. Peskin, S. Kais, Phys. Rev. A **78**, 062106 (2008)
4. P. Cejnar, J. Jolie, Phys. Rev. E **61**, 6237 (2000)
5. W.D. Heiss, J. Phys. A Math. Theor. **45**, 444016 (2012)
6. M.S. Santhanam, V.B. Sheorey, A. Lakshminarayan, Phys. Rev. E **77**, 026213 (2008)
7. M.S. Santhanam, V.B. Sheorey, A. Lakshminarayan, Pramana **48**, 439 (1997)
8. M. Pyzh, S. Krönke, C. Weitenberg, P. Schmelcher, New J. Phys. **20**, 015006 (2018)
9. J.M. Hutson, E. Tiesinga, P.S. Julienne, Phys. Rev. A **78**, 052703 (2008)
10. C. Dembowski, H.-D. Gräf, H.L. Harney, A. Heine, W.D. Heiss, H. Rehfeld, A. Richter, Phys. Rev. Lett. **86**, 787 (2001)
11. I. Barke, F. Zheng, T.K. Rügheimer, F.J. Himpsel, Phys. Rev. Lett. **97**, 226405 (2006)
12. F. Hund, Z. Phys. **40**, 742 (1927)
13. J. von Neumann, E.P. Wigner, Z. Phys. **30**, 467 (1929)
14. A.M.O. de Almeida, *Hamiltonian Systems—Chaos and Quantization* (Cambridge University Press, Cambridge, 2011)
15. T. Timberlake, L.E. Reichl, Phys. Rev. A **59**, 2886 (1999)

16. K. Na, L.E. Reichl, Phys. Rev. A **78**, 063405 (2004)
17. O. Bohigas, M.J. Giannoni, C. Schmit, Phys. Rev. Lett. **52**, 1 (1984)
18. F. Haake, *Quantum Signatures of Chaos* (Springer, Berlin, 2010)
19. J. Karthik, A. Sharma, A. Lakshminarayan, Phys. Rev. A **75**, 022304 (2007)
20. D. Bruß, N. Datta, A. Ekert, L.C. Kwek, C. Macchiavello, Rev. Mod. Phys. **68**, 985 (1996)
21. C. Zener, Proc. R. Soc. Lond. Ser. A **137**, 696 (1932)
22. L.D. Landau, E.M. Lifshitz, *Quantum Mechanics*, 2nd edn. (Pergamon Press, Oxford, 1965)
23. D.R. Yarkony, Rev. Mod. Phys. **68**, 985 (1996)
24. M. Rohith, C. Sudheesh, J. Opt. Soc. Am. B **33**, 126 (2016)
25. B. Sharmila, S. Lakshmibala, V. Balakrishnan, J. Phys. B At. Mol. Opt. Phys. **53**(24), 245502 (2020). https://doi.org/10.1088/1361-6455/abc07e
26. T.M. Cover, J.A. Thomas, *Elements of Information Theory* (Wiley-Interscience, Hoboken, 2006)
27. S. Kullback, R.A. Leibler, Ann. Math. Stat. **22**, 79 (1951)
28. C. Bishop, *Pattern Recognition and Machine Learning* (Springer, New York, 2006)
29. T. Kailath, IEEE Trans. Commun. Technol. **15**, 52 (1967)
30. R.J. Bell, P. Dean, Discuss. Faraday Soc. **50**, 55 (1970)
31. F. Wegner, Z. Phys. B **36**, 209 (1980)
32. L. Viola, W.G. Brown, J. Phys. A Math. Theor. **40**, 8109 (2007)
33. R. Smith, Stat **4**, 291 (2015)
34. P. Tommasini, E. Timmermans, Am. J. Phys. **66**, 881 (1998)
35. S. Qvarfort, S. Bose, A. Serafini, New J. Phys. **22**, 093062 (2020)
36. G. Masada, A. Furusawa, Nanophotonics **5**, 469 (2016)
37. R.T. Thew, K. Nemoto, A.G. White, W.J. Munro, Phys. Rev. A **66**, 012303 (2002)
38. A. Ibort, V.I. Man'ko, G. Marmo, A. Simoni, F. Ventriglia, Phys. Scr. **79**, 065013 (2009)
39. B. Sharmila, V.R. Krithika, S. Pal, T.S. Mahesh, S. Lakshmibala, V. Balakrishnan, J. Chem. Phys. **156**(15), 154102 (2022). https://doi.org/10.1063/5.0087032
40. J. Ma, X. Wang, C.P. Sun, F. Nori, Phys. Rep. **509**, 89 (2011)
41. M. Kitagawa, M. Ueda, Phys. Rev. A **47**, 5138 (1993)
42. L. Sanz, M.H.Y. Moussa, K. Furuya, Ann. Phys. (N.Y.) **321**, 1206 (2006)
43. B. Sharmila, S. Lakshmibala, V. Balakrishnan, Quantum Inf. Process. **18**, 236 (2019)
44. C.A. Trugenberger, Phys. Rev. Lett. **87**, 067901 (2001)
45. G.S. Agarwal, R.R. Puri, Phys. Rev. A **39**, 2969 (1989)
46. P. Macha, G. Oelsner, J.-M. Reiner, M. Marthaler, S. André, G. Schön, U. Hübner, H.-G. Meyer, E. Il'ichev, A.V. Ustinov, Nat. Commun. **5**, 5146 (2014)
47. D.S. Shapiro, P. Macha, A.N. Rubtsov, A.V. Ustinov, Photonics **2**, 449 (2015)
48. M. Tavis, F.W. Cummings, Phys. Rev. **170**, 379 (1968)

Chapter 5
Dynamics and Entanglement Indicators in Bipartite CV Systems

5.1 Introduction

The manner in which the degree of entanglement changes with time in CV, spin and HQ systems has been investigated in considerable detail in the literature, using standard entanglement measures. Interesting aspects of the dynamics include collapse and revival of the entanglement [1], a feature which is somewhat similar (but not identical) to the revivals and fractional revivals in single-mode systems (discussed in Chap. 2), entanglement sudden death and birth (see, for instance, [2]), and entanglement collapse over relatively long times to a constant non-zero value [3]. In this chapter we discuss interesting features of the entanglement in model CV systems during dynamical evolution, with a focus on the performance of the tomographic entanglement indicators. With this in mind, we consider two bipartite models introduced earlier, namely, a multilevel atom interacting with a radiation field [4], and the double-well BEC which was examined in earlier chapters in the context of both revivals and avoided energy-level crossings (see Sects. 2.8 and 4.4). In Chap. 4, we have established that close to avoided energy-level crossings, both ξ_{IPR} and ξ_{TEI} are reliable entanglement indicators. In the present chapter, we will evaluate the performance of ξ_{IPR} and ξ'_{TEI} in this regard. The latter is a modification of ξ_{TEI}; since the procedure used to obtain it is computationally less intensive than that for evaluating ξ_{TEI}, as explained below, it is worth examining it in detail.

We first note that the generalized eigenstates of conjugate pairs of quadrature operators form a pair of mutually unbiased bases [5], since

$$\left|\langle X_\theta, \theta | X_{\theta+\pi/2}, \theta + \pi/2\rangle\right|^2 = 1/(2\pi\hbar) > 0. \tag{5.1}$$

We recall that, by estimating a specific ε-indicator in several sets of mutually unbiased bases, and averaging over these values, we obtain the corresponding ξ-indicator (see Chap. 4). The ξ'_{TEI} indicators, on the other hand, are calculated by restricting the average to just the dominant values of $\varepsilon_{\text{TEI}}(\theta_a, \theta_b)$. In practice, in most cases, instead of averaging over 100 values of $\varepsilon_{\text{TEI}}(\theta_a, \theta_b)$ to obtain ξ_{TEI}, it suffices to average over

© The Author(s), under exclusive license to Springer Nature Switzerland AG 2022

S. Lakshmibala and V. Balakrishnan, *Nonclassical Effects and Dynamics of Quantum Observables*, SpringerBriefs in Physics,
https://doi.org/10.1007/978-3-031-19414-6_5

only those values that exceed the mean by one standard deviation. This yields ξ'_{TEI}. We will show in subsequent sections, by comparing its performance with both ξ_{SVNE} and ξ_{SLE}, that ξ'_{TEI} is as efficient as ξ_{TEI} in estimating the entanglement dynamics in CV systems.

Before proceeding with the assessment of tomographic entanglement indicators, in the next section we set the stage by describing the rich entanglement dynamics in the bipartite model of atom-field interaction mentioned above. Following this, we examine the efficacy of tomographic indicators in this case. Subsequently, we revisit the dynamics of the double-well BEC to assess their performance in this system as well.

5.2 The Bipartite Atom-Field Interaction Model Revisited

5.2.1 Time Evolution

We recall that the Hamiltonian of a system comprising a multilevel atom modeled as an anharmonic oscillator (with Kerr-like nonlinearity) interacting with a single-mode radiation field is given by Eq. (4.38), namely,

$$H_{\text{AF}} = \omega_F a^\dagger a + \omega_A b^\dagger b + \gamma {b^\dagger}^2 b^2 + g(a^\dagger b + a b^\dagger). \tag{5.2}$$

$(a, a^\dagger)$ are photon annihilation and creation operators, $(b, b^\dagger)$ are the atomic ladder operators, and the total number operator $\mathsf{N}_{\text{tot}} = a^\dagger a + b^\dagger b$ commutes with H_{AF}. The Hamiltonian is not symmetric in the two modes, even when $\omega_F = \omega_A$. The Fock basis is the set of product states $|n'\rangle_F \otimes |n\rangle_A \equiv |n'; n\rangle$ where n' and n are the eigenvalues of $a^\dagger a$ and $b^\dagger b$, respectively. The eigenvalues and eigenfunctions of H_{AF} can be found explicitly if either $\gamma = 0$ or $g = 0$. In the absence of the anharmonicity parameter γ, H_{AF} is essentially linear in each of the subsystem variables, and can be diagonalized in terms of linear combinations of the original ladder operators, resulting in periodic exchange of energy between the two modes. If $g = 0$, a closed-form expression can be derived (as a superposition of the product basis states mentioned above) for the wave function at any instant of time. Such a closed form solution can still be obtained even when $g \neq 0$, provided the frequencies of the two oscillators differ sufficiently in numerical value. In this case, an effective Hamiltonian for the system can be written solely in terms of the field modes. This Hamiltonian is of the form $\overline{\omega} a^\dagger a + \overline{\chi} {a^\dagger}^2 a^2$ (with an inherent Kerr-like nonlinearity), where $\overline{\chi} = \gamma g^4/(\omega_F - \omega_A)^4$ and $\overline{\omega} = \omega_F - g^2/(\omega_F - \omega_A)$. It is to be noted that this is essentially the Hamiltonian examined in Chap. 2. A rich spectrum of changes in the entanglement can be seen as a function of time, based on the value of the ratio γ/g and the specific nature of the initial state.

A convenient choice of basis is given by $|N - n; n\rangle \equiv |N - n\rangle_F \otimes |n\rangle_A$, where N denotes the eigenvalues of N_{tot}. For each given value of N, the Hamiltonian H_{AF} can be diagonalized in the space spanned by the states $|N - n; n\rangle$, where

$n = 0, 1, 2, \ldots N$. The density operators corresponding to the full system and the reduced density operator corresponding to the field can be computed numerically, at various instants of time. An extensive investigation of the dynamics [4] reveals that a variety of phenomena can occur, depending on the initial state chosen and the interplay between the strengths of the nonlinearity and the field-atom coupling. We summarize below the important results obtained.

(a) The sub-Poissonian nature of the field state is evident from the negativity of the Mandel Q parameter, defined as

$$Q = \frac{\langle a^{\dagger 2} a^2 \rangle - \langle a^\dagger a \rangle^2}{\langle a^\dagger a \rangle}. \tag{5.3}$$

(b) For weak nonlinearity ($\gamma/g \ll 1$) it has been shown that, when the atom is initially in the ground state and the field is initially either in a Fock state or in a CS, collapses and near-revivals of the mean photon number occur almost periodically in time. The near-revival time is $\approx 2\pi/\gamma$ (initial Fock state) and $\approx 4\pi/\gamma$ (initial CS). (It is a general feature [6] that the revival time is inversely proportional to the coefficient of the term in the Hamiltonian that is quadratic in the quantum numbers concerned.) The foregoing is to be contrasted with the dynamics of the Jaynes-Cummings model where the revival phenomenon is absent if the initial state of the field is a Fock state.

(c) As the strength of the nonlinearity is increased ($\gamma/g \gg 1$), collapses and revivals gradually become less discernible.

These features follow from approximate analytical expressions obtained in closed form in [4] for the wave function $|\psi(t)\rangle$ at any time t. We outline this instructive procedure briefly, before we proceed to assess the performance of entanglement indicators in this model. To begin with, one defines the operators $\mathsf{a} = (a + b)/\sqrt{2}$ and $\mathsf{b} = -i(a - b)/\sqrt{2}$ satisfying $[\mathsf{a}, \mathsf{a}^\dagger] = [\mathsf{b}, \mathsf{b}^\dagger] = 1$, $\mathsf{a}^\dagger\mathsf{a} + \mathsf{b}^\dagger\mathsf{b} = a^\dagger a + b^\dagger b = \mathsf{N}_{\rm tot}$. The Hamiltonian $H_{\rm AF}$ can then be written as $H_{\rm S} + H'$, where the 'secular' part is

$$H_{\rm S} = \omega_F \mathsf{N}_{\rm tot} + g(\mathsf{a}^\dagger\mathsf{a} - \mathsf{b}^\dagger\mathsf{b}) + (\gamma/8)[3\mathsf{N}_{\rm tot}{}^2 - 2\mathsf{N}_{\rm tot} - (\mathsf{a}^\dagger\mathsf{a} - \mathsf{b}^\dagger\mathsf{b})^2], \tag{5.4}$$

and H' contains nonresonant terms which oscillate with much higher frequencies, and can therefore be dropped. In what follows, we will work with $H_{\rm S}$ alone. Let $|j\rangle_{\mathsf{a}}$ and $|k\rangle_{\mathsf{b}}$ be eigenstates of $\mathsf{a}^\dagger\mathsf{a}$ and $\mathsf{b}^\dagger\mathsf{b}$, respectively, and let $|j\rangle_{\mathsf{a}} \otimes |k\rangle_{\mathsf{b}} \equiv \parallel j; k\rangle\rangle$. It can then be shown that

$$H_{\rm S} \parallel N - p; p\rangle\rangle = \Omega_0(N, p) \parallel N - p; p\rangle\rangle, \tag{5.5}$$

where

$$\Omega_0(N, p) = \omega_F N + (\gamma/8)[(3\,N^2 - 2N) - (N - 2p)^2] + g(N - 2p). \tag{5.6}$$

The time evolution is investigated by first relating the Fock states corresponding to $(a, a^\dagger)$ and $(b, b^\dagger)$, on the one hand, with those of $(\mathsf{a}, \mathsf{a}^\dagger)$ and $(\mathsf{b}, \mathsf{b}^\dagger)$, on the other. For this purpose, we recall that the generator of the state $|n; m\rangle$ is given by $G(\alpha, \beta) = \mathrm{e}^{\alpha a^\dagger + \beta b^\dagger}$. That is,

$$G(\alpha, \beta)|0; 0\rangle \equiv |\alpha; \beta\rangle = \sum_{m,n=0}^{\infty} \frac{\alpha^n \beta^m}{\sqrt{n!\, m!}} |n; m\rangle \quad (\alpha, \beta \in \mathbb{C}). \tag{5.7}$$

Likewise, the generator of the state $\| n; m\rangle\!\rangle$ is given by $\overline{G}(u, v) = \mathrm{e}^{u\mathsf{a}^\dagger + v\mathsf{b}^\dagger}$. Then,

$$\overline{G}(u, v) \, \| 0; 0\rangle\!\rangle \equiv \| u; v\rangle\!\rangle = \sum_{m,n=0}^{\infty} \frac{u^n v^m}{\sqrt{n!\, m!}} \, \| n; m\rangle\!\rangle, \quad (u, v \in \mathbb{C}). \tag{5.8}$$

From the fact that $\| 0; 0\rangle\!\rangle = |0; 0\rangle$ and the commutation relations between the operators, it follows that

$$\overline{G}(u, v) = G\big((u + iv)/\sqrt{2}, (u - iv)/\sqrt{2}\big). \tag{5.9}$$

Inserting the expansions 5.7 and 5.8 in Eq. 5.9 and equating coefficients of $u^n v^m$, we get on simplification

$$\| \alpha; \beta\rangle\!\rangle = |(\alpha + i\beta)/\sqrt{2}\,; (\alpha - i\beta)/\sqrt{2}\rangle. \tag{5.10}$$

Using Eqs. 5.5, 5.6 and 5.10, we can now obtain an expression for the time-dependent wave function

$$|\psi(t)\rangle = \mathrm{e}^{-iH_s t/\hbar} |\alpha; \beta\rangle \tag{5.11}$$

corresponding to an initial state $|\alpha; \beta\rangle$. After some simplification, we find

$$|\psi(t)\rangle = \mathrm{e}^{-(|\alpha|^2 + |\beta|^2)/2} \sum_{N=0}^{\infty} \sum_{p=0}^{N} \mathrm{e}^{-i\Omega_0(N,p)t} \frac{(-i)^p (\alpha - \beta)^p (\alpha + \beta)^{N-p}}{2^{N/2} \sqrt{p!\,(N-p)!}} \, \| N - p; p\rangle\!\rangle. \tag{5.12}$$

Average values such as the mean photon number can now be calculated directly from this expression for the wave function at all times. The role played by different initial states of the radiation field on the subsequent dynamics can also be investigated readily. In particular, setting $\beta = 0$ in the expression above, i.e., taking the atom to be initially in the ground state, we find that at $t = 4\pi r/\gamma$ (where r is an integer),

$$\begin{aligned} |\psi(4\pi r/\gamma)\rangle &= \| \, (-1)^r \alpha \mathrm{e}^{-4\pi i r g/\gamma}/\sqrt{2}\,; -(-1)^r i\alpha \mathrm{e}^{4\pi i r g/\gamma}/\sqrt{2}\rangle\!\rangle \\ &= |(-1)^r \sqrt{2}\,\alpha \cos(4\pi r g/\gamma)\,; -(-1)^r i\sqrt{2}\,\alpha \sin(4\pi r g/\gamma)\rangle. \end{aligned} \tag{5.13}$$

It follows that, at the instants $t = 4\pi r/\gamma$, the field is in a CS with an amplitude depending on $\cos(4\pi r g/\gamma)$. This establishes the occurrence of approximate revivals

of an initial coherent state in the case of weak nonlinearity. The corresponding expression for the mean photon number at any time t is found to be

$$\langle a^{\dagger}a\rangle = \tfrac{1}{2}|\alpha|^2\big[1+\cos(2gt)\exp\{-2|\alpha|^2\sin^2(\gamma t/4)\}\big]. \tag{5.14}$$

The envelope function is therefore $\exp\{-2|\alpha|^2\sin^2(\gamma t/4)\}$, and the maximum of the first revival of the mean photon number occurs at $t = 4\pi/\gamma$. A similar analysis when the radiation field is initially in a Fock state shows that the wave function undergoes revivals, and that the maximum of the mean photon number occurs at the instant $t = 2\pi/\gamma$. Numerical estimates of the revival times agree with the aforementioned predictions both for an initial Fock state and for an initial CS. In the latter case, however, the detailed behavior of the oscillations close to revivals differs from the analytical predictions based on the secular approximation. The maximum of the revival of the mean photon number, for instance, does not attain the value $|\alpha|^2$. For completeness, we mention that the authors of [4] have also obtained a closed-form expression for the mean photon number in an improved approximation if the atom and the field are initially in number states. When the field is initially in a CS, the mean photon number at time t is obtained by summing up an appropriate series, and the agreement between the numerical results and the analytical predictions is very reasonable. The approximation discussed here is evidently not valid in the case of strong nonlinearity and it can be seen that the revival phenomenon is generically absent.

5.2.2 Entanglement Dynamics

We now proceed to examine how the field-atom entanglement changes with time, starting from an initial unentangled state. For sufficiently small non-zero values of the ratio γ/g, a phenomenon akin to collapses and near-revivals of the entanglement could occur over certain intervals of time. It is important to note that the system does not return to its unentangled initial state at any subsequent time, as the revivals are only approximate ones, and the entanglement is never strictly zero. This is not surprising, as there is more than one time scale governing the evolution. However, it is to be noted that while this is a generic feature, specific models can be constructed to display entanglement sudden death, as mentioned earlier. As in the case of the revival phenomena described in Chap. 2, relevant observables (in this case, the two-mode quadrature variables) mimic these features of the entanglement. Such near-revivals in entanglement are unambiguously seen for sufficiently small values of the ratio γ/g, in the plots of the SVNE ($-\mathrm{Tr}\,(\rho_i \ln \rho_i)$) and the SLE ($1-\mathrm{Tr}\,(\rho_i^2)$) (where the subscript i represents either the field or the atom), as functions of scaled time gt for

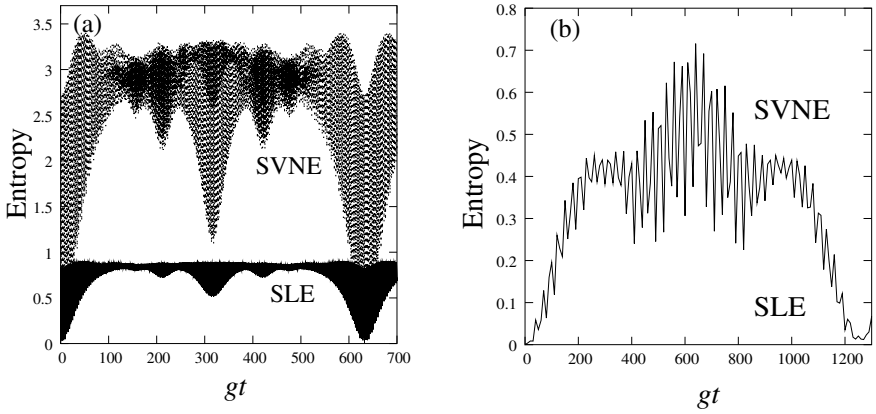

Fig. 5.1 SVNE and SLE versus gt with $\gamma/g = 10^{-2}$ for **a** an initial Fock state $|10\,;\,0\rangle$ and **b** an initial coherent state $|\alpha\,;\,0\rangle$ with $|\alpha|^2 = 1$. These figures are reproduced from [1]

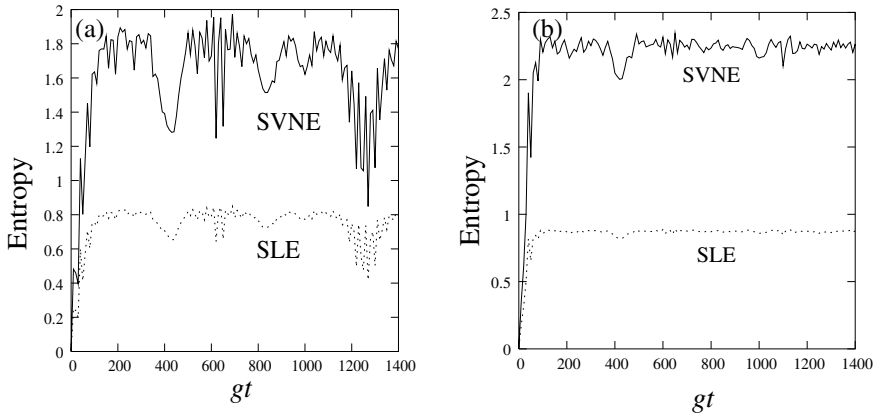

Fig. 5.2 SVNE and SLE versus gt for an initial state $|(\alpha, 5)\,;\,0\rangle$ for **a** $|\alpha|^2 = 1$ and **b** $|\alpha|^2 = 5$ ($\gamma/g = 10^{-2}$). These figures are reproduced from [1]

different initial states. This is evident from plots of SLE and SVNE versus scaled time for $\omega_F = \omega_A = 1$, $\gamma = 1$ and $g = 100$ (see Figs. 5.1 and 5.2).[1]

If the atom is initially in the ground state, and the field is either a 10-photon state (Fig. 5.1a) or a CS with $|\alpha|^2 = 1$ (Fig. 5.1b), the entropies return periodically to values close to their original ones. In contrast, if the initial state of the field is a PACS, the extent of revival is significantly reduced (Figs. 5.2a, b). With an increase in the value of $|\alpha|^2$, the oscillations die down, and near-saturation of the entropies sets in.

[1] Figs. 5.1–5.2 are reproduced from *Wave packet dynamics of entangled two-mode states*, Sudheesh et al. [1] with permission from IOP Publishing.

Two comments are in order: First, it can be verified that the dynamics as revealed by the SVNE and SLE can be captured effectively in the manner in which the two-mode quadrature variables $(x_A + x_B)/2$ and $(p_A + p_B)/2$, (where $x_A = (a + a^\dagger)/\sqrt{2}$, $p_A = -i(a - a^\dagger)/\sqrt{2}$, $x_B = (b + b^\dagger)/\sqrt{2}$ and $p_B = -i(b - b^\dagger)/\sqrt{2}$) vary with time. Second, for sufficiently strong nonlinearity, the revival phenomenon is absent. This is also borne out in the dynamics of the relevant observables. Thus, treating these observables (more accurately, their expectation values and higher moments) as dynamical variables in an appropriate phase space, the tools of classical dynamical systems theory can be applied to understand their ergodicity properties. This reveals a rich spectrum of behavior, which will be discussed in the sequel.

5.2.3 *Tomographic Entanglement Indicators During Time Evolution*

In order to assess the quality of ξ'_{TEI} as an entanglement indicator, we consider initial states of the full system that are unitarily evolving pure states, which are either product states or entangled states. In the former case, we consider the atom to be in its ground state $|0\rangle$ and the field to be in either a CS or an m-PACS, initially. In the latter case, we consider two states, namely, the binomial state $|\psi_{\text{bin}}\rangle$ and the two-mode squeezed state $|\zeta\rangle$. We recall from Chap. 1 that $|\psi_{\text{bin}}\rangle = 2^{-N/2} \sum_{n=0}^{N} \binom{N}{n}^{1/2} |N-n; n\rangle$, where N is a non-negative integer and $|N-n; n\rangle$ is the product state corresponding to the field and the atom in the number states $|N-n\rangle$ and $|n\rangle$ respectively. Similarly, $|\zeta\rangle = \mathrm{e}^{\zeta^* ab - \zeta a^\dagger b^\dagger} |0; 0\rangle$, where $\zeta \in \mathbb{C}$ and $|0; 0\rangle$ is the product state corresponding to $N = 0, n = 0$. The procedure involves numerically generating the field tomograms at many instants of time, and then calculating the corresponding ξ'_{TEI} from the tomogram at each instant. Since this is only for the purpose of demonstration, known states or density operators suffice. The corresponding SVNE and SLE, and from these the differences

$$d_1(t) = |\xi_{\text{SVNE}} - \xi'_{\text{TEI}}|, \quad d_2(t) = |\xi_{\text{SLE}} - \xi'_{\text{TEI}}|, \tag{5.15}$$

are computed. From Fig. 5.3a[2] corresponding to an initial two-mode squeezed state, and Fig. 5.3b where the initial state is an unentangled product of a CS and the atomic ground state, the following observation can be made. Independent of the parameter values and the precise nature of the initial state, the indicator ξ'_{TEI} is in much better agreement with ξ_{SLE} than with ξ_{SVNE} over the time interval considered (2000 instants, separated for numerical computations by a time step $0.2\,\pi/g$). Hence, in the analysis that follows, we choose ξ_{SLE} as the reference entanglement indicator.

Further, a comparison between $d_2(t)$ and the difference

$$\Delta(t) = |\xi_{\text{SVNE}} - \xi_{\text{SLE}}|. \tag{5.16}$$

[2] For figures similar to Figs. 5.3, 5.4 and 5.5, but for different values of the parameters, see *Estimation of entanglement in bipartite systems directly from tomograms*, Sharmila et al. [7].

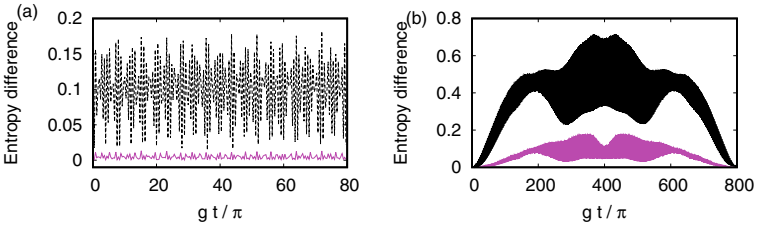

Fig. 5.3 $d_1(t)$ (black) and $d_2(t)$ (pink) versus scaled time gt/π, for $\omega_F = \omega_A = \gamma = 1$ in the atom-field interaction model. **a** $g = 0.4$, initial two-mode squeezed state $|\zeta\rangle$, $\zeta = 0.2$. **b** $g = 200$, initial state $|\alpha; 0\rangle$, $|\alpha|^2 = 1$. For similar figures with **a** $g = 0.2, \zeta = 0.1$ and **b** $g = 100$ respectively, see [7]

reveals that $\Delta(t) > d_2(t)$. Hence, in our analysis we consider only $d_2(t)$ and the difference

$$d_3(t) = |\xi_{\text{SLE}} - \xi_{\text{IPR}}|. \tag{5.17}$$

This comparison provides insights into the nature of the tomographic entanglement indicators considered here. We have already established that entanglement measures capture signatures of near-revival phenomena. In the present context, it is evident from Fig. 5.4a that, at $gT_{\text{rev}}/\pi = 800$ (the revival time in the present instance), the agreement of ξ'_{TEI} with ξ_{SLE} is much better than that of ξ_{IPR}. In most cases, $d_2(t)$ is much smaller than $d_3(t)$ over the entire time interval considered even for large values of γ/g (see Fig. 5.4b). We therefore infer that in this model, during dynamics ξ'_{TEI} fares better as an entanglement indicator than ξ_{IPR}. Further, the manner in which $d_2(t)$ varies in time is very different from that of $d_3(t)$, if the initial field states depart from ideal coherence. In this case, for sufficiently small values of γ/g, ξ_{IPR} performs notably better than ξ'_{TEI} as seen from Fig. 5.4c. With an increase in the magnitude of γ/g, both entanglement indicators show similar behavior (see Fig. 5.4d).

The lessons learnt in the case of entangled initial states are somewhat different. The precise nature of the initial state now plays a significant role in determining the performance of the entanglement indicators. We first consider an initial two-mode squeezed state $|\zeta\rangle$. From Fig. 5.5, it is clear that over the entire time interval considered, if ζ is sufficiently small, ξ'_{TEI} is a better indicator than ξ_{IPR}. However, with an increase in the value of ζ, neither indicator is adequately reliable.

In contrast, for an initial binomial field state, ξ_{IPR} performs considerably better than ξ'_{TEI} does. We recall from Sect. 4.4 that this feature has its genesis in the nature of the binomial state, and the relevance of the Hamming distance in this context. With an increase in the Hamming distance, ξ_{IPR} performs better. Hence, when evaluating the extent of entanglement for superpositions of states that are Hamming-uncorrelated (equivalently, for bipartite states which are separated by a Hamming distance equal to 2), both in spin systems [8] and CV systems [7, 9], this indicator is reliable. In the atom-field interaction model that we have discussed here, both the subsystems are infinite dimensional. In this case, $|\psi_{\text{bin}}\rangle$ can be expanded as a superposition of states which are Hamming-uncorrelated. As a consequence, during dynamical evolution of the system, ξ_{IPR} turns out to be a superior entanglement indicator as compared to ξ'_{TEI}.

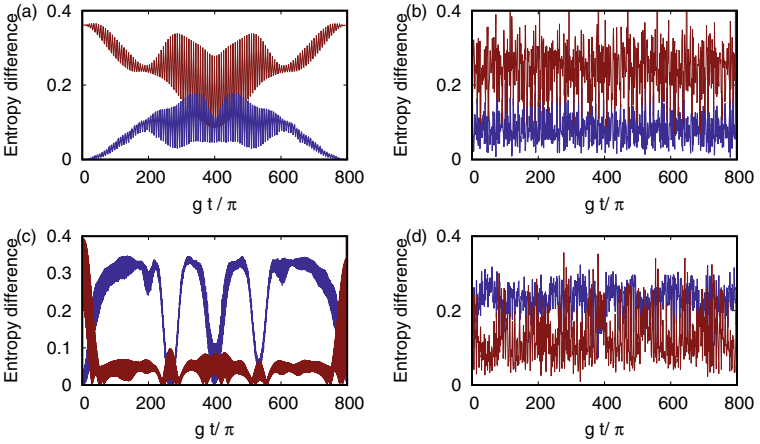

Fig. 5.4 $d_2(t)$ (blue) and $d_3(t)$ (brown) versus scaled time gt/π, for $\omega_F = \omega_A = \gamma = |\alpha|^2 = 1$ in the atom-field interaction model. **a**, **b** Initial state $|\alpha; 0\rangle$, $g = 200$ and 0.4 respectively. **c**, **d** Initial state $|(\alpha, 5); 0\rangle$, $g = 200$ and 0.4 respectively. For similar figures with **a**, **c** $g = 100$, and **b**, **d** $g = 0.2$ respectively, see [7]

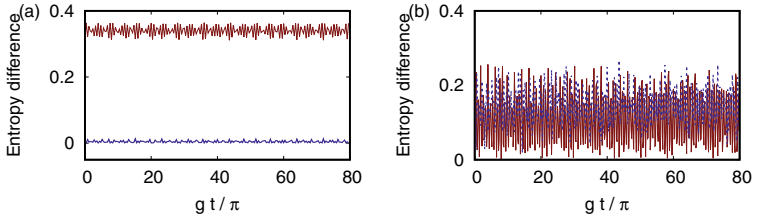

Fig. 5.5 $d_2(t)$ (blue) and $d_3(t)$ (brown) versus scaled time gt/π, for $\omega_F = \omega_A = \gamma = 1$, $g = 0.4$ in the atom-field interaction model. Initial two-mode squeezed state $|\zeta\rangle$, **a** $\zeta = 0.2$ and **b** $\zeta = 0.8$. For similar figures with $g = 0.2$, **a** $\zeta = 0.1$ and **b** $\zeta = 0.7$ respectively, see [7]

5.3 The Double-Well BEC Model Revisited

5.3.1 Time Development

We now consider once again the effective Hamiltonian in Eq. (2.53) for a BEC in a double well,

$$H_{\text{BEC}} = \omega_0 \mathsf{N}_{\text{tot}} + \omega_1 (a^\dagger a - b^\dagger b) + u_0 \mathsf{N}_{\text{tot}}^2 - \lambda (a^\dagger b + a b^\dagger). \tag{5.18}$$

We recall that $(a, a^\dagger)$ and $(b, b^\dagger)$ are respectively the boson annihilation and creation operators of the atoms in wells A and B, $\mathsf{N}_{\text{tot}} = a^\dagger a + b^\dagger b$, u_0 is the nonlinear interaction strength (both in the individual modes as well as in their interaction), λ is the linear interaction strength, and ω_0, ω_1 are constants. The initial states considered

for our purpose here are the following: (i) the unentangled direct product $|\alpha_A, m_1\rangle \otimes |\alpha_B, m_2\rangle$ of boson-added coherent states of atoms in the wells A and B respectively, where $\alpha_A, \alpha_B \in \mathbb{C}$; (ii) the binomial state $|\psi_{\rm bin}\rangle$ (Eq. 1.27); and (iii) the two-mode squeezed vacuum state $|\zeta\rangle$ (Eq. 1.24). In this case, the basis states are product states of the condensates in the two wells.

In case (i) above, the state of the system at any subsequent time can be calculated explicitly [10]. In cases (ii) and (iii), the state vector as a function of time is computed numerically. Following the procedure outlined earlier, it can be shown that $\xi'_{\rm TEI}$ agrees better with $\xi_{\rm SLE}$ than with $\xi_{\rm SVNE}$. Further, the difference between $\xi'_{\rm TEI}$ and $\xi_{\rm SLE}$ is smaller than that between $\xi_{\rm SVNE}$ and $\xi_{\rm SLE}$. In this model, the relevant ratio that characterizes the dynamics is u_0/λ_1 where $\lambda_1 = (\omega_1^2 + \lambda^2)^{1/2}$. It can also be established that for entangled initial states $|\psi_{\rm bin}\rangle$ and $|\zeta\rangle$, the general trends in the behavior of the entanglement indicators are consistent with earlier results from the atom-field interaction model.

5.3.2 *Decoherence Effects in the Double-Well BEC Model*

Before concluding this chapter, we comment on the decoherence aspect in this model. As a toy example, we consider an initial state $\|\alpha_A\rangle \otimes |\alpha_B\rangle$, with $\alpha_A = \sqrt{0.001}$ and $\alpha_B = 1$: The relatively small numerical value of α_A has been chosen so that this state can be approximated by a superposition of the zero-boson state $|0\rangle_A$ and the one-boson state $|1\rangle_A$. To identify the effects of decoherence, and the efficacy of tomograms in assessing entanglement during dissipation, we may consider the entangled state of the system at any instant, say $u_0 t = \pi/2$, and apply damping to subsystem A alone for a time interval τ. For illustrative purposes, the decoherence is taken to proceed through amplitude decay. The master equation (Eq. (2.42)) is given by

$$\frac{{\rm d}\rho}{{\rm d}\tau} = -\Gamma(a^\dagger a\rho - 2a\rho a^\dagger + \rho a^\dagger a), \tag{5.19}$$

where ρ is the density matrix, Γ is the rate of loss and τ is the time parameter reckoned from the instant $t = \pi/(2u_0)$. Since the system is bipartite, the expression for ρ is a generalization of the corresponding expression for single-mode systems (see Eqs. 2.43 and 2.44). The solution to this master equation is [11]

$$\rho(\tau) = \sum_{n,m,n',m'=0}^{\infty} \rho_{n,m,n',m'}(\tau)|n;m\rangle\langle n';m'|, \tag{5.20}$$

where

$$\rho_{n,m,n',m'}(\tau) = {\rm e}^{-\Gamma\tau(n+n')} \sum_{r=0}^{\infty} \binom{n+r}{r}^{1/2} \binom{n'+r}{r}^{1/2} (1 - {\rm e}^{-2\Gamma\tau})^r \rho_{n+r,m,n'+r,m'}(\tau = 0). \tag{5.21}$$

$\rho(\tau = 0)$ is chosen to be $|\Psi_{00}(\pi/2u_0)\rangle \langle\Psi_{00}(\pi/2u_0)| |$. (The expression for $|\Psi_{00}(t)\rangle$ as a function of time t is given in Eq. (2.54)).

Since the bipartite state here is a mixed state, ξ_{SVNE} corresponding to subsystems A and B are not equal to each other. They are denoted by $\xi^{(A)}_{\text{SVNE}}$ and $\xi^{(B)}_{\text{SVNE}}$ respectively. The entropy of the full system is $\xi^{(AB)}_{\text{SVNE}}$. The quantum mutual information

$$\xi_{\text{QMI}} = \xi^{(A)}_{\text{SVNE}} + \xi^{(B)}_{\text{SVNE}} - \xi^{(AB)}_{\text{SVNE}} \tag{5.22}$$

is of relevance here. At each instant τ, ξ'_{TEI}, $\xi^{(A)}_{\text{SVNE}}$ and ξ_{QMI} have been calculated numerically, for u_0, ω_0, ω_1 and λ equal to 1. Since the subsystem entropies are not equal, we expect that, if the tomogram captures decoherence effects well, ξ'_{TEI} must match ξ_{QMI} during dynamical evolution. This is indeed borne out when ξ'_{TEI}, ξ_{QMI} and $\xi^{(A)}_{\text{SVNE}}$ are compared [7] with each other.

To summarize: The lessons from the foregoing investigations are that, even without information about the off-diagonal elements of the density matrix, substantial reproduction of the qualitative aspects of entanglement dynamics can be achieved *using the tomograms alone*. This is to be contrasted with the fact that entanglement measures such as ξ_{SVNE} and ξ_{SLE} can be constructed only if the off-diagonal elements of the density operator are known. The tomographic entanglement indicator ξ'_{TEI} fares significantly better for generic initial states of a bipartite CV system even during time evolution, compared to more familiar entanglement indicators such as ξ_{IPR}. A fair picture of the performance of different entanglement indicators will emerge more clearly if they are assessed in the context of HQ systems as well. We proceed to carry out this investigation in Chap. 6.

References

1. C. Sudheesh, S. Lakshmibala, V. Balakrishnan, J. Phys. B: At. Mol. Opt. Phys. **39**, 3345 (2006). https://doi.org/10.1088/0953-4075/39/16/017
2. T. Yu, J. Eberly, Science **323**, 598 (2009)
3. P. Laha, B. Sudarsan, S. Lakshmibala, V. Balakrishnan, Int. J. Theor. Phys. **55**, 4044 (2016)
4. G.S. Agarwal, R.R. Puri, Phys. Rev. A **39**, 2969 (1989)
5. S. Weigert, M. Wilkinson, Phys. Rev. A **78**, 020303 (2008)
6. S. Seshadri, S. Lakshmibala, V. Balakrishnan, J. Stat. Phys. **101**, 213 (2000)
7. B. Sharmila, S. Lakshmibala, V. Balakrishnan, Quantum Inf. Process. **18**, 236 (2019). https://doi.org/10.1007/s11128-019-2352-0
8. L. Viola, W.G. Brown, J. Phys. A: Math. Theor. **40**, 8109 (2007)
9. B. Sharmila, S. Lakshmibala, V. Balakrishnan, J. Phys. B: At. Mol. Opt. Phys. **53**, 245502 (2020)
10. B. Sharmila, K. Saumitran, S. Lakshmibala, V. Balakrishnan, J. Phys. B: At. Mol. Opt. **50**, 045501 (2017)
11. A. Biswas, G.S. Agarwal, Phys. Rev. A **75**, 032104 (2007)

Chapter 6
Dynamics of Entanglement Indicators in Hybrid Quantum and Spin Systems

6.1 Introduction

In this chapter we investigate the dynamics of hybrid quantum (HQ) systems, in generic models of two-level or three-level atoms interacting with a quantized radiation field. A sizeable body of literature exists on the entanglement dynamics in the Jaynes-Cummings model and its extensions such as the double Jaynes-Cummings (DJC) [1] and double Tavis-Cummings (DTC) [2] models. These and other variants have been investigated extensively with particular reference to revival phenomena, entanglement sudden death (ESD) and sudden birth, and entanglement transfer between states. The effects of additional terms such as the Kerr nonlinearity, dipole-dipole interaction, beamsplitter and Ising interactions on the entanglement dynamics have been examined in considerable detail in these systems.

Certain tripartite systems, treated effectively as two subsystems interacting with each other, display a collapse of the bipartite entanglement to a constant nonzero value over a significant time interval during temporal evolution. Examples include an optomechanical system omprising a two-level atom placed inside a Fabry-Pérot type cavity with a vibrating mirror attached to one end [3], and a system comprising a single three-level Λ atom interacting with two radiation fields [4, 5]. It is instructive to review the salient aspects of ESD in the DJC model, before we proceed to identify the usefulness of entanglement indicators (obtained both in this model and in the DTC model) from numerically generated tomograms at various instants of time during unitary evolution of the system. Wherever possible, these are compared with tomograms from equivalent circuits implemented in the IBM quantum computing platform (IBM Q). The latter are obtained from experimental runs as well as simulations using the IBM open quantum assembly language (QASM) simulator [6].

In the next section we briefly review aspects of entanglement dynamics in the DJC model. Following this, we examine the efficacy of entanglement indicators in this model. The performance of ξ_{TEI} and ξ'_{TEI} during time evolution is assessed by making a comparison with ξ_{QMI} at different instants of time. We recall that ξ_{QMI} is defined (see Eq. 5.22) as

© The Author(s), under exclusive license to Springer Nature Switzerland AG 2022

S. Lakshmibala and V. Balakrishnan, *Nonclassical Effects and Dynamics of Quantum Observables*, SpringerBriefs in Physics,
https://doi.org/10.1007/978-3-031-19414-6_6

$$\xi_{\mathrm{QMI}} = \xi_{\mathrm{SVNE}}^{(A)} + \xi_{\mathrm{SVNE}}^{(B)} - \xi_{\mathrm{SVNE}}^{(AB)}. \tag{6.1}$$

Here, the bipartite subsystem AB and the subsystems A and B are denoted by the superscripts (AB), (A) and (B) respectively.

6.2 The Double Jaynes-Cummings Model

In the double Jaynes-Cummings (DJC) model, two 2-level atoms denoted by C and D are initially entangled. C (respectively, D) interacts with the lossless cavity field A (respectively, B) with strength g_0. Although the two subsystems (each comprising an atom and a radiation field) do not interact with each other, the initial atom-atom entanglement leads to very interesting subsequent dynamics [1].

6.2.1 Dynamics

The effective Hamiltonian (setting $\hbar = 1$) is

$$H_{\mathrm{DJC}} = \sum_{j=A,B} \chi_{\mathrm{F}} a_j^{\dagger} a_j + \sum_{k=C,D} \chi_0 \sigma_{kz} + g_0 \left(a_A^{\dagger} \sigma_{C-} + a_A \sigma_{C+}\right) + g_0 \left(a_B^{\dagger} \sigma_{D-} + a_B \sigma_{D+}\right). \tag{6.2}$$

The photon destruction and creation operators are $a_j, {a_j}^{\dagger}$ $(j = A, B)$ respectively, χ_0 is the difference in energy between the energy levels of each atom, and χ_{F} is the frequency of each radiation field. The atomic ladder operators for subsystem $k\,(= C, D)$ are given in terms of the Pauli matrices by $\sigma_{k\pm} = (\sigma_{kx} \pm i\sigma_{ky})$. The initial atomic states are

$$|\psi_{\alpha_0}\rangle = (\cos\,\alpha_0)|g\rangle_1 \otimes |g\rangle_2 + (\sin\,\alpha_0)|e\rangle_1 \otimes |e\rangle_2 \tag{6.3}$$

and

$$|\phi_{\alpha_0}\rangle = (\cos\,\alpha_0)|g\rangle_1 \otimes |e\rangle_2 + (\sin\,\alpha_0)|e\rangle_1 \otimes |g\rangle_2. \tag{6.4}$$

Here, the respective ground and excited states of atom p $(p = 1, 2)$ are denoted by $|g\rangle_p$ and $|e\rangle_p$. (This notation will be generalized in the sequel to describe the double Tavis-Cummings (DTC) model.) In the DJC model, 1 and 2 are to be replaced by C and D, respectively. A and B are initially taken to be in the vacuum states $|0\rangle_A$ and $|0\rangle_B$ respectively. The full system's initial states that are considered here are given by the factored products $|0\rangle_A \otimes |0\rangle_B \otimes |\psi_{\alpha_0}\rangle_{CD} \equiv |0; 0; \psi_{\alpha_0}\rangle$ and $|0\rangle_A \otimes |0\rangle_B \otimes |\phi_{\alpha_0}\rangle_{CD} \equiv |0; 0; \phi_{\alpha_0}\rangle$. Corresponding to each of these states, the extent of entanglement between the atoms has been obtained using the standard procedure of

tracing out the two fields and calculating the atomic concurrence [7, 8] (see Eq. 1.38). Of special interest to us is the case of zero detuning ($\chi_0 = \chi_F$). Then, corresponding to $|0; 0; \psi_{\alpha_0}\rangle$, the concurrence is given by [1] $\max[0, f(t)]$ where

$$f(t) = \cos^2(g_0 t)[|\sin 2\alpha_0| - \sin^2(g_0 t)\cos^2\alpha_0]. \tag{6.5}$$

It can be seen that the atomic entanglement can vanish abruptly at a subsequent instant and the state becomes separable for a substantial interval of time, before entanglement sets in again. The duration of entanglement death increases as the extent of initial entanglement decreases. In contrast to this case, for an initial state $|0; 0; \phi_{\alpha_0}\rangle$ the atomic concurrence is $|\sin 2\alpha_0|\cos^2(g_0 t)$, which is purely oscillatory, vanishing at specific instants. Since α_0 merely controls the time interval of ESD, in what follows we set $\cos\alpha_0 = \sin\alpha_0 = 1/\sqrt{2}$ without loss of generality, and evaluate the reliability of the tomographic entanglement indicators in both the DJC and DTC models. The corresponding initial atomic states are of the form

$$|\psi_+\rangle = \big(|g\rangle_1 \otimes |g\rangle_2 + |e\rangle_1 \otimes |e\rangle_2\big)/\sqrt{2} \tag{6.6}$$

and

$$|\phi_+\rangle = \big(|g\rangle_1 \otimes |e\rangle_2 + |e\rangle_1 \otimes |g\rangle_2\big)/\sqrt{2}. \tag{6.7}$$

The two initial states that we consider are therefore $|0\rangle_A \otimes |0\rangle_B \otimes |\psi_+\rangle_{CD} \equiv |0; 0; \psi_+\rangle$ and $|0\rangle_A \otimes |0\rangle_B \otimes |\phi_+\rangle_{CD} \equiv |0; 0; \phi_+\rangle$.

As in the case of CV systems, numerically generated tomograms (corresponding to both the field and atomic subsystem) have been used for our calculations. At approximately 300 instants of time, separated by a time step equal to 0.02 (in units of π/g_0), the tomograms and hence the entanglement indicator ξ_{TEI} have been obtained, It was shown in Chap. 5 that for radiation fields, both ξ_{TEI} and ξ'_{TEI} (the latter computed by averaging over only those values of $\varepsilon_{TEI}(\theta_a, \theta_b)$ that exceed the mean by one standard deviation) were in fairly good agreement with each other [9]. The purpose of the present exercise is to investigate whether a similar observation is valid even for HQ systems. Plots of ξ_{TEI}, ξ'_{TEI} and ξ_{QMI} versus $g_0 t$ are shown in Fig. 6.1a–c[1] for the field subsystem, setting the detuning parameter $(\chi_F - \chi_0)$ to zero in Fig. 6.1a, b and to unity in Fig. 6.1c. The initial states considered are $|0; 0; \phi_+\rangle$ in Fig. 6.1a and $|0; 0; \psi_+\rangle$ in Fig. 6.1b, c. From the plots it is clear that ξ'_{TEI} and ξ_{TEI} are similar in their dynamical behavior, and that they closely follow the trends revealed by ξ_{QMI} (the latter scaled by a factor of 10, for ease of comparison), in all the three cases. The precise initial atomic state selected and the extent of detuning clearly affect the qualitative features of the indicators, particularly close to their maximum values.

For ready comparison, the atomic system has been investigated for the same set of parameter values and initial states. In this case, while ξ_{TEI} and ξ_{QMI} show similar dynamical behavior over the time interval considered, ξ'_{TEI} differs in its qualitative

[1] Figures 6.1, 6.2, 6.3 and 6.4 are reproduced from *Tomographic entanglement indicators in multipartite systems*, Sharmila et al. [10] with permission from Springer.

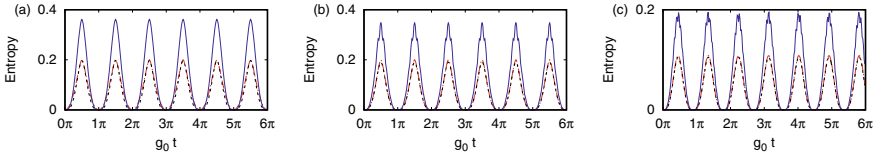

Fig. 6.1 ξ_{TEI} (black), ξ'_{TEI} (blue) and $0.1\,\xi_{\mathrm{QMI}}$ (red) versus scaled time $g_0 t$ for the field subsystem in the DJC model. Initial state, **a** $|0;0;\phi_+\rangle$; **b**, **c** $|0;0;\psi_+\rangle$. Detuning parameter **a**, **b** 0 and **c** 1. Figures are reproduced from [10]

features. This is in sharp contrast to the situation that prevails in the case of the field dynamics examined earlier.

6.2.2 *Equivalent Circuit for the DJC Model and the IBM Q Platform*

In order to assess the extent of real experimental losses in these systems, an equivalent circuit for the DJC model was submitted to the IBM Q platform [10]. The qubit tomograms (analogous to the atomic tomograms of the model) obtained from the experimental implementation of the circuit, the simulations carried out on the IBM QASM simulator (without considering experimental losses), and the numerical tomograms generated (again without taking dissipation into account) have been compared in what follows. We observe that for zero detuning, ξ_{QMI} returns to its initial value of 2 at the instant $t = \pi/g_0$. This feature is used in constructing the equivalent circuit (Fig. 6.2).

We now describe the circuit components using the standard notation of the IBM platform [6]. The dynamics of the two-atom subsystem is followed by the qubits $q[0]$ and $q[4]$. The auxiliary qubits that facilitate the dynamics are $q[2]$ and $q[3]$, with each of these toggling between $|0\rangle$ and $|1\rangle$, respectively, as the atomic transitions involve absorption and emission of one photon alone.

The operator $U_3(\theta', \varphi', \upsilon)$ in the circuit is given by

$$U_3(\theta', \varphi', \upsilon) = \begin{bmatrix} \cos(\theta'/2) & -\mathrm{e}^{i\upsilon}\sin(\theta'/2) \\ \mathrm{e}^{i\varphi'}\sin(\theta'/2) & \mathrm{e}^{i(\upsilon+\varphi')}\cos(\theta'/2) \end{bmatrix}, \tag{6.8}$$

where $0 \leqslant \theta' < \pi$, $0 \leqslant \varphi' < 2\pi$ and $0 \leqslant \upsilon < 2\pi$. The four qubits are initially in the qubit state $|0\rangle$. The atomic state $|\psi_+\rangle$ in the DJC model is mimicked by the initial entanglement between $q[0]$ and $q[4]$. This is produced by using an Hadamard gate and a controlled-NOT gate between $q[4]$ and $q[2]$, with a SWAP gate between $q[2]$ and $q[0]$. Note that θ' is analogous to $g_0 t$. In order to ensure that the entanglement is equal to 2 (its initial value), we set $\theta' = \pi$. Further, we choose $\varphi' = 0$, and $\upsilon = \pi/2$.

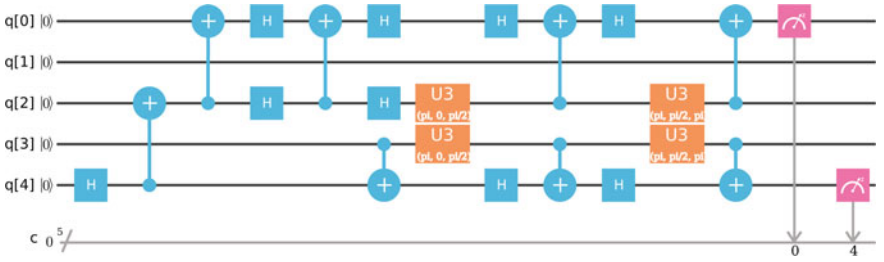

Fig. 6.2 Equivalent circuit for the DJC model (created using IBM Q). This figure is reproduced from [10]

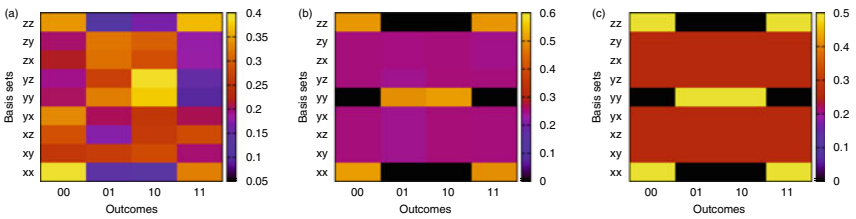

Fig. 6.3 Tomograms from **a** IBM Q experiment, **b** QASM simulation, **c** numerical computations of the DJC model. Figures are reproduced from [10]

It can be seen that the matrix $U_3(\pi, \pi/2, \pi)$ in the equivalent circuit is equal to $U_3^\dagger(\pi, 0, \pi/2)$.

Measurements are carried out in the x, y and z bases corresponding to the matrices defined in Eq. (4.14). The IBM platform automatically allows for a measurement in the z-basis.The measurement in the x-basis is carried out through an Hadamard gate operation followed by a measurement in the z-basis. Defining the operator

$$S^\dagger = \begin{bmatrix} 1 & 0 \\ 0 & -i \end{bmatrix}, \tag{6.9}$$

a measurement in the y-basis is achieved by the sequence of operations $S^\dagger$, Hadamard, and finally a measurement in the z-basis. Measurements in all the three bases are necessary to construct the spin tomogram in Fig. 6.3a. This is equivalent to the bipartite atomic tomogram in the basis sets of the Pauli matrices.

These spin tomograms have also been obtained experimentally using the IBM superconducting circuit with appropriate Josephson junctions (Fig. 6.3a), as well as the QASM simulator (Fig. 6.3b). A comparison of these tomograms with their corresponding numerically generated counterparts (Fig. 6.3c), reveal that the qualitative aspects are very similar in Fig. 6.3b, c.This is expected as the circuit trails the DJC model's dynamics.

Again, owing to experimental losses at different stages, Fig. 6.3a is distinctly different from the others, and this is reflected in the corresponding numerical value of ξ_{TEI}, which is 0.0410 ± 0.0016. The simulation and numerical analysis yield values

0.2311 and 0.2310, respectively. For completeness, we summarize the procedure followed for this purpose. Six tomograms were obtained from six executions of the experiment. Each execution comprised 8192 runs over each of the 9 basis sets. The error bar was calculated from the standard deviation of $\xi_{\rm TEI}$.

It is instructive to estimate the extent of loss in state preparation *alone*. For this purpose, an entangled state of two qubits was prepared using an Hadamard gate and a controlled-NOT gate, to effectively mimic $|\psi_+\rangle$. For the initial state $|\psi_+\rangle$, the values for $\xi_{\rm TEI}$ obtained from the experiment, simulation and the DJC model are $0.0973 \pm 0.0240, 0.2310$ and 0.2310 respectively. This demonstrates that substantial losses arise even in state preparation. In order to estimate how an increase in the number of atoms in the system increases these losses, we turn to the double Tavis-Cummings (DTC) model and its equivalent circuit.

6.3 The Double Tavis-Cummings Model

6.3.1 The Model

The DTC model comprises four 2-level atoms, C_1, C_2, D_1 and D_2, where C_1 and C_2 (respectively, D_1 and D_2) are coupled with strength g_0 to a radiation field A (resp., B) of frequency $\chi_{\rm F}$. The notation used is similar to that in $H_{\rm DJC}$ (Eq. 6.2), since the Hamiltonian $H_{\rm DTC}$ can be obtained from the former by appropriate changes. Setting $\hbar = 1$, we have [2]

$$H_{\rm DTC} = \sum_{j=A,B} \chi_{\rm F}\, a_j^\dagger a_j + \sum_{k=1}^{2} \big\{ \chi_0\, \sigma_{C_k z} + \chi_0\, \sigma_{D_k z} + g_0(a_A^\dagger \sigma_{C_k -} + a_A \sigma_{C_k +}) + g_0(a_B^\dagger \sigma_{D_k -} + a_B \sigma_{D_k +}) \big\}. \tag{6.10}$$

C_1 and D_1 (respectively, C_2 and D_2) are taken to be in the initial state $|\psi_+\rangle$ (Eq. 6.6) or $|\phi_+\rangle$ (Eq. 6.7). Each field is initially in its vacuum state $|0\rangle$. Hence the initial states of the full system considered are $|0; 0; \psi_+; \psi_+\rangle$, $|0; 0; \phi_+; \phi_+\rangle$ and $|0; 0; \psi_+; \phi_+\rangle$. The notation $|0; 0; \psi_+; \phi_+\rangle$ indicates, for instance, that A and B are in the state $|0\rangle$, the subsystem (C_1, D_1) is in the state $|\psi_+\rangle$, and the subsystem (C_2, D_2) is in the state $|\phi_+\rangle$. (We need not consider the initial state $|0; 0; \phi_+; \psi_+\rangle$ separately because the corresponding results can be obtained using symmetry arguments from the results for the initial state $|0; 0; \psi_+; \phi_+\rangle$). For brevity, we denote (C_1, C_2) by C and (D_1, D_2) by D.

6.3.2 Equivalent Circuit and the IBM Q Platform

As the number of atoms in the DTC model is larger than that in the DJC model, the equivalent circuit for the former will have more elements, and hence more losses

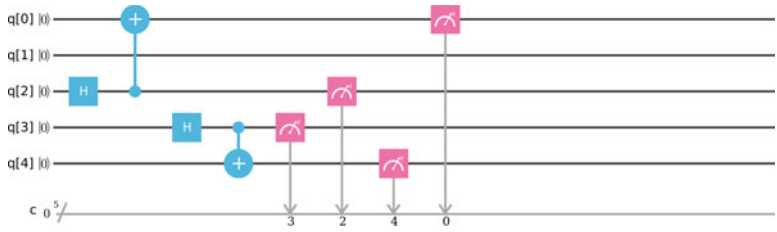

Fig. 6.4 Equivalent circuit of the entangled state $|\psi_+;\psi_+\rangle$ in the DTC model (created using IBM Q). This figure is reproduced from [10]

during its implementation. We require 4 qubits to represent the 4 two-level atoms, and a minimum of 4 auxiliary qubits to aid the dynamics. In what follows, we assess the losses in state preparation *alone*. For this purpose, 4 qubits are prepared in a pairwise entangled state (analogous to the initial state $|\psi_+;\psi_+\rangle$ of the atomic subsystem $(C,\ D)$) using 2 Hadamard gates and 2 controlled-NOT gates (see Fig. 6.4). Here qubits $q[2]$ and $q[3]$ are entangled with qubits $q[0]$ and $q[4]$ respectively. We note that the pair $(q[2], q[3])$ is analogous to subsystem C, and $(q[0], q[4])$ is analogous to D. The entanglement between C and D is quantified using ξ_{TEI}. The numerical values obtained from experiment, simulation and the DTC model are 0.2528, 0.4761 and 0.4621, respectively. In this case, the experiment was executed just once, comprising 8192 runs over each of the 81 basis sets [10]. Hence the outcome of the experiment, namely 0.2528, is stated without an accompanying error bar. As 4 qubits are involved in this circuit, the number of possible outcomes is 16, in contrast to the earlier case which had only 4 possible outcomes. Hence the experimental losses, as well as the difference between the simulated and the numerically obtained values, are higher than those obtained in the case of the DJC model.

A numerical investigation of the time evolution of the entanglement between the field subsystems A and B, and between the atomic subsystems C and D, ignoring experimental losses, reveals that both ξ_{TEI} and ξ'_{TEI} effectively follow ξ_{QMI} for the field subsystem, while ξ'_{TEI} does not reflect ξ_{QMI} for the atomic subsystem. These features are similar to those seen in the DJC model. The results indicate that ξ'_{TEI} is not a good indicator of bipartite entanglement in qubit (atomic) systems.

6.4 Bipartite Entanglement in Tripartite Models

We turn, next, to tripartite systems. With the addition of one more subsystem, we expect to see new features in the entanglement during time evolution. The first system we examine here is a cavity optomechanical set-up comprising a cavity with two mirrors, one of them fixed and the other capable of small oscillations due to radiation pressure inside the cavity. A light membrane is connected to the movable mirror, so that it oscillates with the mirror. A two-level atom is placed inside the cavity. The

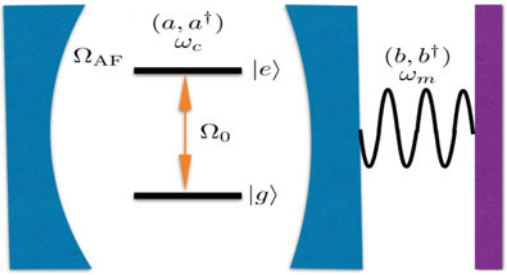

Fig. 6.5 Schematic diagram of a cavity optomechanical system. This figure is reproduced from [3]

radiation field interacts with the atom and also with the movable mirror-membrane unit by pushing the mirror. The second system that we study below is a three-level Λ atom interacting with quantized radiation fields. For specific initial states and parameter values, both these systems exhibit rich entanglement dynamics, with the entanglement collapsing to a nonzero constant value over a considerable time interval, under specific conditions.

6.4.1 The Cavity Optomechanical System

The Hamiltonian $H_{\rm opt}$ for the tripartite optomechanical system has two interaction terms, namely, the photon number operator coupling to the mirror displacement operator, and also a Jaynes-Cummings type of coupling between the atom and the field. Thus

$$H_{\rm opt} = \omega_c\, a^\dagger a + \omega_m\, b^\dagger b + \tfrac{1}{2}\Omega_0\sigma_z - G\, a^\dagger a(b + b^\dagger) + \Omega_{\rm AF}\big(a\,\sigma_+ + a^\dagger\,\sigma_-\big), \tag{6.11}$$

in standard notation. The operators $a, a^\dagger$ correspond to the cavity field of frequency ω_c, the ladder operators $b, b^\dagger$ pertain to the mirror-membrane unit with a natural frequency ω_m, and the two-level atom with a transition frequency Ω_0 has raising and lowering operators $\sigma_+ = |e\rangle\langle g|$ and its hermitian conjugate σ_-, respectively. The atom-field coupling constant is Ω_{AF}, and the optomechanical coupling G is expressed in terms of the cavity length L and the mass m of the mirror by $G = (2m\omega_m/\hbar)^{-1/2}\omega_c/L$. The model (Fig. 6.5)[2] is generic and is applicable, for instance, to the early experiment on Cs atoms [11] in a cavity of length $L = 10\,\mu$m, with atomic transition $(6S_{1/2}, F = 4, m_F = 4) \rightarrow (6P_{3/2}, F = 5, m_F = 5)$, and $\omega_c \approx 10^{14}$ Hz. In such a set-up the oscillator mass m is about 10^{-17} kg, while ω_m is of the order of 10^9 Hz [12]. Corresponding to these values, it can be easily verified that $G \sim 10^6$ Hz, and that the resonance condition $\omega_c = \Omega_0 + \omega_m$ is satisfied. Since the coupling

[2] Figures 6.5, 6.6 and 6.7 are reprinted from *Nonclassical effects in optomechanics: dynamics and collapse of entanglement*, Laha et al. [3] with permission from The Optical Society.

between the atom and the cavity depends on the atomic position R through the relation $\Omega_0 = \Omega_R \exp(-R^2/\overline{\omega}^2)$, where Ω_R (the vacuum Rabi frequency for zero detuning) is $2\pi \times 120$ MHz, and $\overline{\omega}$ (the waist of the cavity mode) is equal to 15 μm, R can be suitably arranged to set the value of Ω_0 close to that of G. The Hamiltonian $H_{\rm opt}$ above has manifestly bipartite interactions alone. Since there are three subsystems, it is helpful to transform the Hamiltonian to a form where tripartite interactions are explicitly present, in addition to specific bipartite interactions. This is possible in the limit $\omega_m \gg G, \Omega_0$, as is the case here. Writing Ω_0 as rG where r is a real constant of order unity, an effective Hamiltonian $H_{\rm eff}$ for this system can now be obtained [13]. It is given by

$$H_{\rm eff} = (G^2/\omega_m)\left\{r\left(a^\dagger b\sigma_- + ab^\dagger\sigma_+\right) - r^2\left(a^\dagger a\,\sigma_z - \sigma_+\sigma_-\right) - (a^\dagger a)^2\right\}. \quad (6.12)$$

We draw attention to two new features in $H_{\rm eff}$, namely, the Kerr-like nonlinearity in the field subsystem, and a tripartite interaction between the field, atom and membrane. This form facilitates comparison between terms linear in r and terms quadratic in r. The dimensionless time is now given by $t_s = G^2 t/\omega_m$.

The dynamics of this system has been examined in Ref. [14] for a product initial state, with the field in a single photon state, the mirror in the oscillator ground state and the atom in a superposition of its two energy levels. It has been shown that GHZ-like maximal entanglement can be obtained. More detailed investigations of the SVNE of all the three subsystems, and the squeezing properties as the system evolves in time, have been carried out corresponding to an initial state which is a product of the field state (a CS $|\alpha\rangle$), the membrane in the oscillator ground state, and the atom in the superposed state of the two energy levels [3], $(\cos\phi_0|e\rangle + \sin\phi_0|g\rangle)$. In what follows we have taken α to be real, without loss of generality.

The dynamics turns out to be sensitive to the precise values of r, ϕ_0, and α. The system is considered to be effectively bipartite. The SVNE $S_{\rm a}$ of the atom, for instance, is obtained treating the atom as a subsystem and the field-mirror unit as the other subsystem. Similar definitions hold for the field SVNE $S_{\rm f}$ and the SVNE $S_{\rm m}$ computed for the mirror subsystem.

Plots of $S_{\rm a}$, $S_{\rm m}$ and $S_{\rm f}$ versus the dimensionless time t_s, for $r = 1$, are shown in Fig. 6.6a–f. Certain interesting features emerge in the entanglement dynamics, and are listed below.

(i) From Fig. 6.6a it is clear that for $\phi_0 = \pi/2$, even for small values of α (set to 1 in the figure), $S_{\rm a}$ equals 1 (the maximum allowed value of the SVNE for a two-level atom) at specific instants of time. With an increase in the value of α (see Fig. 6.6b), the entanglement collapses to this maximum value for a substantial time interval.

(ii) Further, plots of $S_{\rm a}$ and $S_{\rm m}$ versus scaled time are identical for $\phi_0 = \pi/2$ (compare the red curves in Fig. 6.6a, c, and also b, d). This can be traced back to the fact that for $\phi_0 = \pi/2$, the density matrices for the atom and mirror effectively involve only two states, namely, $|g\rangle$ and $|e\rangle$ for the atom and $|0\rangle$ and $|1\rangle$ for

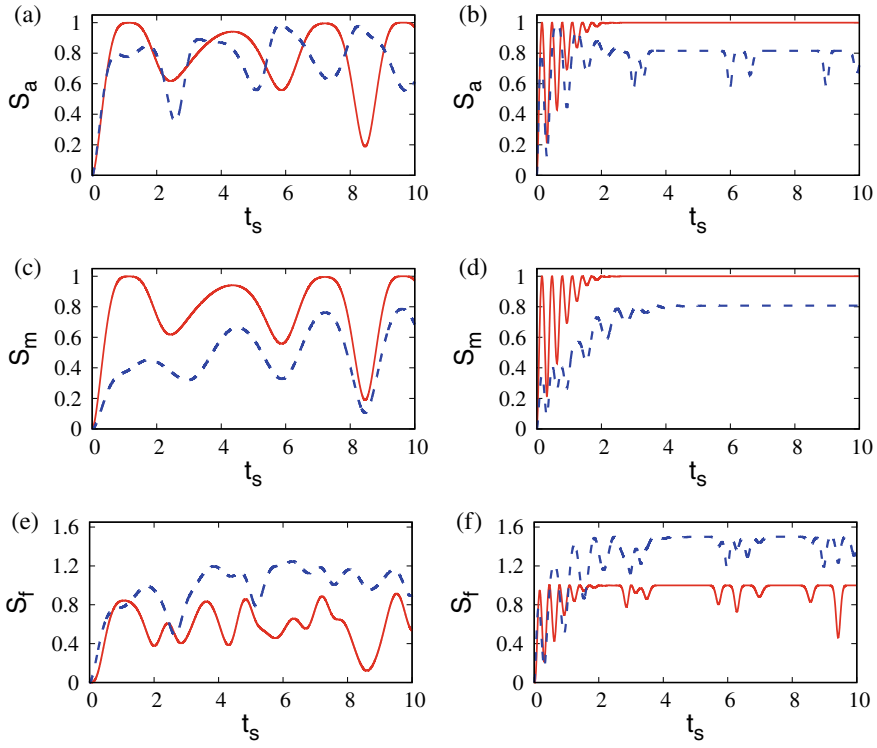

Fig. 6.6 S_a (top panel), S_m (centre panel) and S_f (bottom panel) versus t_s for $r = 1$, $\phi_0 = \frac{1}{2}\pi$ (red), $\frac{1}{4}\pi$ (blue), and $\alpha = 1$ (first column) and 5 (second column). Figures are reproduced from [3]

the mirror. By making a correspondence between the states of these two subsystems, it can be seen that the two subsystem density matrices are identical in form, and the result above follows [3].

(iii) For other values of ϕ_0 (e.g., for $\phi_0 = \pi/4$) in Fig. 6.6a, b, such collapses in S_a are not discernible. However, for sufficiently large values of α, S_m collapses to a nonzero value, although considerably less than 1, for a significant time interval (Fig. 6.6d).

(iv) An increase in the time interval of the collapse of S_a to sufficiently high values of entanglement can be achieved by using photon-added coherent states $|\alpha, m\rangle$ as the initial field states. The interval of entanglement collapse has been shown to increase with increasing m.

(v) It is clear from Fig. 6.6e, f that S_f does not exhibit collapses, for any value of α and ϕ_0.

(vi) The sensitivity of the entanglement to the value of r is borne out by examining the manner in which S_a changes with time for $r = 1/\sqrt{2}$.

In this case, for both $\phi_0 = \pi/2$ and $\pi/4$, and for sufficiently large values of α (Fig. 6.7b), S_a collapses to a constant nonzero value for longer intervals of time, as compared to the earlier case. For small values of α, collapse is absent, but the extent of entanglement reaches high values at certain instants, as seen from Fig. 6.7a.

(vii) It can be verified that both S_m and S_f also follow this trend.

The picture that emerges so far from models of field-atom interaction is as follows: We recall from Fig. 5.2 (b) that, when a multilevel atom (modelled as a nonlinear oscillator, with strong nonlinearity as compared to the interaction strength) interacts with a radiation field which is initially in a CS $|\alpha\rangle$ with a sufficiently large value of α, the SVNE approximately saturates about a nonzero value after some time has elapsed. Oscillations about this value arise due to interactions between the subsystems. This feature, that pertains to the bipartite entanglement when the full system is divided into two subsystems, continues to be valid even in the case of the tripartite optomechanical model. In the latter case, however, the atom only has two energy levels, but both bipartite and tripartite interactions are present. Here too, since a CS with a sufficiently large value of α is roughly close in its properties to a PACS with a relatively smaller value of α, saturation of the entropy also arises for an initial field state which is a PACS with a smaller intensity. However, as seen from Fig. 5.2a, in this case also oscillations in the SVNE are more pronounced for an initial CS, with smaller values of α (compare the corresponding figures for the atomic SVNE for $r = 1$ and $1/\sqrt{2}$.) It can be verified that these gross features hold in the case of S_m and S_f as well.

As the dynamics is very sensitive to the value of r, it is worth analyzing the contributions from different terms in H_{eff}, corresponding to two different values of r. For sufficiently large α, all terms in the Hamiltonian have comparable significance. The first term on the right-hand side of Eq. 6.12 is manifestly symmetric with respect to the mirror and the atom. However, there is an asymmetry between the field-mirror interaction (the second term alone on the right in H_{eff}) and the field-atom interaction (both the first and the second terms on the right in H_{eff}). This is responsible for the differences in the dynamics as reflected in S_m and S_a (see the top and middle panels of the second column in Fig. 6.6). For $r = 1/\sqrt{2}$, the significant contribution to the dynamics is from the first term on the right in Eq. 6.12. In this case, too, an analysis on lines similar to the foregoing accounts for the gross features seen in S_m, S_a and S_f.

6.4.2 Λ-*Atom Interacting with Radiation Fields*

We now extend our investigation to tripartite systems comprising a three-level V-type or Λ-type atom interacting with light. Such systems have been used widely to examine a variety of phenomena, including electromagnetically induced transparency (EIT) and the Autler-Townes effect. The literature on the subject, which comprises both theoretical investigations and experiments, is vast [5, 15–20]. The purpose of the

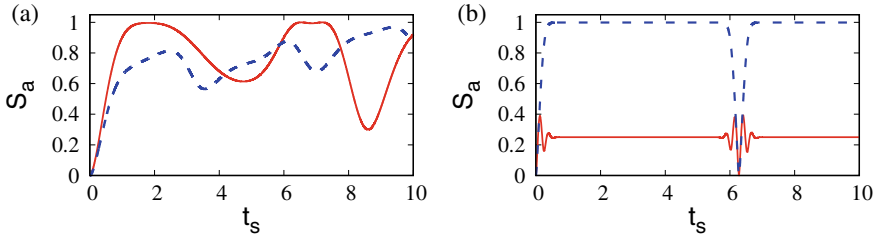

Fig. 6.7 S_a versus t_s for $r = 1/\sqrt{2}$, $\phi_0 = \frac{1}{2}\pi$ (red), $\frac{1}{4}\pi$ (blue), and $\alpha = 1$ (**a**) and 5 (**b**). Figures are reproduced from [3]

present discussion is to examine the role of a finite number of atomic levels on the entanglement dynamics.

We begin by summarizing results on the dynamics of the field mode in two models describing the interaction between light and a three-level V-type atom, where the field has inherent nonlinearities [4]. To set the terms of reference, we consider first a bipartite model of a single-mode radiation field interacting with a V-type atom, enabling transitions from either of the excited levels to the ground state of the atom. Here, a new feature emerges in the entanglement dynamics. Signatures of near-revival phenomena are captured in the field SVNE in this system, even in the case of strong nonlinearity. This is in contrast to the earlier result for the atom-field interaction model where, regardless of the initial state, plausible signatures of near- revival phenomena are seen in the SVNE only in the weak nonlinearity regime. The finite dimensional Hilbert space of the V-type atom thus plays a crucial role in bipartite entanglement dynamics. Consistent with our earlier results, any significant departure of the initial field state from coherence, or an initial CS with large $|\alpha|^2$, effectively erases revivals.

The second model is a tripartite extension of the foregoing, where two independent single-mode fields interact with the V-type atom. Denoting the excited states of the atom by $|1\rangle$ and $|2\rangle$, and the ground state by $|3\rangle$, one of the radiation modes induces $|1\rangle \rightarrow |3\rangle$ transitions, while the other induces $|2\rangle \rightarrow |3\rangle$ transitions. The ratio of the strength of the nonlinearity to the strength of the atom-field interaction is a control parameter. For the atom initially in $|1\rangle$ and the fields in the CS $|\alpha\rangle$, our investigations reveal that the revival phenomenon is absent, for sufficiently large field nonlinearities, independent of the value of $|\alpha|$. This indicates that, if the ratio of the strength of the nonlinearity to that of the interaction is high, then, even if two subsystems of a full system have high-dimensional Hilbert spaces associated with them, the revival phenomenon is absent, independent of whether these large subsystems interact with each other directly (as in the earlier example of the atom-field interaction model) or through much smaller subsystems.

The next step is to explore, in the strong nonlinearity regime, the possible occurrence of interesting entanglement phenomena during time evolution. These include entanglement collapse, revivals, oscillatory behavior, etc., as an appropriate parameter of the system is fine tuned. The identification of an experimentally measurable

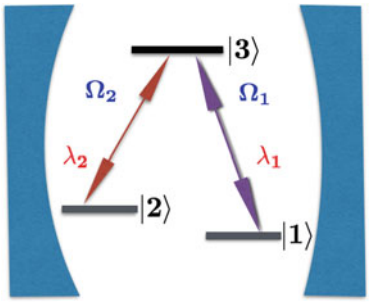

Fig. 6.8 Schematic diagram of the Λ system. This figure is reproduced from [22]

observable which follows these changes in the entanglement dynamics would be desirable, as that would provide a novel approach towards understanding the dependence of ergodicity properties of quantum expectation values on tunable system parameters, via an analysis of the time series of the observables concerned. For this purpose, we consider a Λ-atom interacting with two quantized radiation fields. The rich entanglement dynamics of this system is closely mimicked by the dynamics of the mean photon number of either field. This provides an ideal platform for exploring interesting connections with aspects of classical dynamical systems. The gross features of the dynamics discussed below are preserved even if a V-type atom is used instead of the Λ-atom.

The two lower energy states of the Λ-atom are $|1\rangle$ and $|2\rangle$, and the excited state is $|3\rangle$. The fields F_1 and F_2 with respective frequencies Ω_1 and Ω_2, mediate, respectively, $|1\rangle \rightarrow |3\rangle$ and $|2\rangle \rightarrow |3\rangle$ transitions. Direct transitions between $|1\rangle$ and $|2\rangle$ are dipole forbidden (Fig. 6.8).[3] The photon destruction and creation operators corresponding to the fields F_i, $(i = 1, 2)$ are a_i and ${a_i}^\dagger$ respectively. An intensity-dependent coupling (IDC) $f(\mathsf{N}_i)$, which depends on the photon number operators $\mathsf{N}_i = {a_i}^\dagger a_i$, governs the interaction between the radiation fields and the atom. This is a new feature that has been introduced in the system at hand, compared to the models we have examined hitherto. Different forms of IDC have been introduced in the literature. Following [21], we will set $f(\mathsf{N}_i) = (1 + \kappa_i \mathsf{N}_i)^{1/2}$. As we will see in what follows, this form provides a framework for exploring novel features that emerge in this model. Further, it provides a route to assess the performance of 'tools' such as return distributions, Lyapunov exponents, etc., (used in understanding the ergodicity properties of classical dynamical variables) in a quantum context, where observables are treated as dynamical variables.

Setting $\hbar = 1$, the Hamiltonian H_Λ is given by

$$H_\Lambda = \sum_{j=1}^{3} \omega_j \sigma_{jj} + \sum_{i=1}^{2} \Big\{ \Omega_i \, a_i^\dagger a_i + \chi \, {a_i^\dagger}^2 a_i^2 + \lambda \big[a_i \, f(\mathsf{N}_i) \, \sigma_{3i} + f(\mathsf{N}_i) \, a_i^\dagger \, \sigma_{i3} \big] \Big\}. \tag{6.13}$$

[3] Figures 6.8 and 6.9 are reproduced from *Recurrence network analysis in a model tripartite quantum system*, Laha et al. [22] with permission from IOP Publishing.

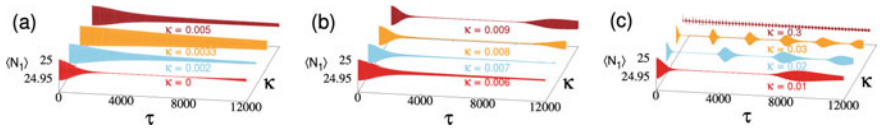

Fig. 6.9 $\langle \mathsf{N}_1 \rangle$ versus τ for different values of κ. Initial state $|1; \alpha; \alpha\rangle$, $|\alpha|^2 = 25$, $\chi/\lambda = 5$. Figures are reproduced from [22]

Here, $\sigma_{jk} = |j\rangle\langle k|$ are the Pauli operators, with $|j\rangle$ denoting an atomic state ($j = 1, 2, 3$), $\{\omega_j\}$ are positive constants, χ is the strength of the nonlinearity, and λ is the atom-field coupling.The detuning parameter $\omega_3 - \omega_i - \Omega_i$ is set to zero. The system is treated as bipartite, with the atom as a subsystem and the two fields as the other subsystem.

The short-time dynamics of the atomic SVNE is interesting. For both fields initially in a PACS $|\alpha, 5\rangle$, with $|\alpha|^2 = 10$, and for strong nonlinearity compared to the interaction strength i.e., $\chi/\lambda = 5$, setting the IDC of both fields to be equal, it has been shown [5] that the atomic SVNE passes through a bifurcation cascade, as the intensity parameter κ is slowly varied from 0 to 1. Further, the mean photon number of either field mimics this behavior. As expected, for the fields initially in a CS $|\alpha\rangle$ with a sufficiently large value of $|\alpha|$ ($|\alpha|^2 = 25$), the same behavior is seen both in the atomic SVNE and in the mean photon number, as shown in [22].

The entanglement collapse when $\kappa = 0$, reflected in the dynamics of the mean photon number $\langle \mathsf{N}_1 \rangle$ corresponding to the field F_1 (see Fig. 6.9) from approximately 3000–9000 units of scaled time $\tau = \lambda t$, is replaced by a 'pinched' effect over the same time interval for $\kappa = 0.002$. In contrast, for $\kappa = 0.0033$ there is a significantly larger spread in the range of values of the mean photon number, and the pinch seen for lower values of κ is absent. The qualitative behavior of $\langle \mathsf{N}_1 \rangle$ for $\kappa = 0.005$ is very similar to that which arises for $\kappa = 0.002$. Thus, $\kappa = 0.0033$ is a special value, for the selected values of χ/λ and $|\alpha|^2$. With further increase in κ, an oscillatory pattern in the mean photon number takes over, the spacing between successive crests and troughs diminishing with increasing κ. This feature persists up to $\kappa = 1$. The time interval $\tau = 0$–10,000 suffices to capture all these features pertaining to the bifurcation cascade in the dynamics of the mean photon number of either field.

6.5 Entanglement and Squeezing in NMR Experiments

There is a considerable amount of ongoing research on quantum information processing using liquid state NMR techniques, as the latter are suitable for diverse manipulations of spin dynamics and the interplay between electronic, nuclear and spin degrees of freedom in small liquid molecules (see, for instance, [23, 24]). Demonstration of spin squeezing [25, 26], generation [27] and quantification of entanglement [28, 29] and identification of the links between entanglement and squeezing are some of the milestones in these experiments.

In order to extract the density operator corresponding to the spin degrees of freedom in nuclear systems, and subsequently quantify the extent of entanglement, several procedures using NMR techniques have been proposed and implemented in the literature [30–32]. However, when a considerably large number of qubits are involved, scalability of the state reconstruction program using standard procedures is a challenge [33, 34]. This is primarily because the program is time consuming due to the need for several positive-operator-valued measurements. Alternative procedures such as compressed sensing have been proposed. Here, a judicious choice of a subset of the data suffices to identify the quantum state [35–38]. But this has proved successful only in specific cases where the density matrix has special properties, and is inadequate for reconstruction of generic multiqubit entangled states.

In the spirit of the theme of this work, we now proceed to estimate entanglement and squeezing properties of spin systems from the tomograms, and benchmark these entanglement indicators against standard measures [39], using actual data from three different liquid-state NMR experiments (labeled I, II and III in the sequel), in contrast to the numerically generated data examined in earlier chapters. The experimental data were obtained from the NMR-QIP group in IISER Pune, India. The details regarding the methods of state preparation, the data obtained, and the errors involved in the experiments have been reported in [40, 41]. The NMR experiments I and III have been performed on ^{13}C, ^{1}H and ^{19}F spin-half nuclei in dibromofluoromethane (DBFM) dissolved in deuterated acetone [40]. NMR experiment II has been performed on ^{19}F and ^{31}P spin-half nuclei in sodium flourophosphate (NaFP) dissolved in D_2O [41]. In all the three experiments, bipartite entanglement has been investigated, with special attention paid to the optimal number of tomographic slices that are required.

In what follows, we will calculate spin squeezing from the qubit tomograms using the procedure given in Sect. 4.3 of Chap. 4, and also obtain the tomographic entanglement indicators for the three systems using the standard program that we have implemented in earlier chapters. The performance of the latter is assessed as usual by comparing with standard indicators obtained from the density matrix, such as $\xi_{\rm QMI}$, negativity and discord, defined in Eqs. (5.22), (1.41), and (1.42). While in these specific experiments reconstruction of the density matrix is straightforward, it is important to remember that this in general not true, and the tomographic approach may have considerable advantages, particularly in large systems. With this objective, we work backwards from the density matrix to get the tomograms (in a sense, the inverse problem), and estimate nonclassical properties from the tomograms. This preliminary study will help assess how the tomographic approach fares in experiments, so that it can be extended to qubit/spin systems with large Hilbert spaces, taking into consideration experimental losses.

In all the three experiments mentioned above, the following procedure has been carried out:
(a) The Liouville equation has been numerically solved using the Hamiltonian and the initial state as inputs, to obtain the density matrix at different instants. From these the corresponding tomograms have been computed. Entanglement indicators and squeezing properties have been calculated directly from the tomograms. (b) The tomograms have also been re-created from the experimental data. An estimate of

the effect of experimental losses on the entanglement indicators calculated in this case can be obtained by comparing the results of (a) and (b). (c) Further, a direct computation of the standard entanglement measures from both the reconstructed and numerically obtained density matrices has been carried out. The extent to which tomographic indicators reproduce the generic features of these 'density matrix dependent' entanglement measures, over the time interval considered, gives us information on whether at all, state reconstruction can be circumvented.

We reiterate that in all these experiments, owing to the smallness of the Hilbert space, the relevant density matrices can easily be reconstructed from the tomograms by first obtaining the deviation matrix, and then computing the density matrix from the deviation matrix (for details, see [40]).

Our results indicate that in a large collection of spins the tomographic approach could provide a viable alternative to state reconstruction protocols in estimating nonclassical effects. We now proceed to examine the NMR experiment I. All results reported here are from [39].

6.5.1 NMR Experiment I

Our starting point is the set of reconstructed density matrices at different instants of time obtained from the experiment. We recall that the system of interest comprises ^{1}H spins (subsystem A), ^{19}F spins (subsystem B), and ^{13}C spins (subsystem M), evolving in time. In each DBFM molecule, the focus is on a chain of three qubits, in the linear topology A-M-B, such that the probe qubits A and B only interact with each other via the mediator qubit M. The effective Hamiltonian s given by [40]

$$H_{\text{NMR1}} = 4\chi_s(\sigma_{Ax} + \sigma_{Bx})\sigma_{Mx} \tag{6.14}$$

where χ_s is a constant, and σ_{ix} $(i = A, B, M)$ is the Pauli matrix for the subsystem concerned. The initial state is

$$\rho_{MAB}(0) = \tfrac{1}{2}|\phi_+\rangle_{AB\,AB}\langle\phi_+| \otimes \rho_{M+} + \tfrac{1}{2}|\psi_+\rangle_{AB\,AB}\langle\psi_+| \otimes \rho_{M-}, \tag{6.15}$$

where $\rho_{M+} = |+\rangle_{M\,M}\langle+|$, $\rho_{M-} = |-\rangle_{M\,M}\langle-|$, and

$$\left.\begin{aligned} |\psi_+\rangle_{AB} &= \big(|\downarrow\rangle_A \otimes |\downarrow\rangle_B + |\uparrow\rangle_A \otimes |\uparrow\rangle_B\big)/\sqrt{2}, \\ |\phi_+\rangle_{AB} &= \big(|\downarrow\rangle_A \otimes |\uparrow\rangle_B + |\uparrow\rangle_A \otimes |\downarrow\rangle_B\big)/\sqrt{2}. \end{aligned}\right\} \tag{6.16}$$

Here $|\uparrow\rangle$ and $|\downarrow\rangle$ denote the eigenstates of σ_z, while $|+\rangle$ and $|-\rangle$ denote those of σ_x. It is straightforward to show that

$$\rho_{MAB}(t) = \tfrac{1}{2}|\Psi_0\rangle\langle\Psi_0| + \tfrac{1}{2}|\Psi_1\rangle\langle\Psi_1| \tag{6.17}$$

where

$$\left.\begin{aligned} |\Psi_0\rangle &= |+\rangle_M \left[\cos(2\chi_s t)|\phi_+\rangle_{AB} - i\sin(2\chi_s t)|\psi_+\rangle_{AB}\right], \\ |\Psi_1\rangle &= |-\rangle_M \left[\cos(2\chi_s t)|\psi_+\rangle_{AB} + i\sin(2\chi_s t)|\phi_+\rangle_{AB}\right]. \end{aligned}\right\} \tag{6.18}$$

Of direct relevance to us is the reduced density matrix

$$\rho_{AB}(t) = \mathrm{Tr}_M\left(\rho_{MAB}(t)\right) \tag{6.19}$$

corresponding to the subsystem AB.

As explained in Sect. 4.3, in order to estimate spin squeezing properties, the mean spin direction needs to be identified. In this case it is a null vector, since $\langle\sigma_{ix}(t)\rangle$, $\langle\sigma_{iy}(t)\rangle$ and $\langle\sigma_{iz}(t)\rangle$ ($i = A, B$) are all zero. Hence, any unit vector $\mathbf{v}_\perp$ can be chosen to obtain the required variance, at any given instant. Using several such unit vectors, the corresponding variances, and hence the minimum variance $(\Delta J_{\min})^2$ is obtained as a function of time. By comparing this with the corresponding numerically obtained variance it can be seen that for this system, there is excellent agreement between the variance obtained from the experimentally reconstructed density matrices and from numerical calculations. Further, the extent of squeezing $[1 - 2(\Delta J_{\min})^2]$, increases with time [39].

In the case of second-order squeezing, too, the minimum variance denoted by $(\Delta\mathcal{J}_{\min})^2$ obtained both numerically and from the experimental data as a function of time are in reasonable agreement with each other. The extent of agreement increases with time. This can be traced back to the fact that the off-diagonal contributions in the density matrix decrease with time, and hence the tomograms that capture only the diagonal elements become 'truer' representations of the corresponding states. As in the earlier case, the measure of second-order squeezing given by $[1 - 8(\Delta\mathcal{J}_{\min})^2]$ (for comparative purposes) increases with time. Neither subsystem displays entropic squeezing [43].

The entanglement indicators computed in this experiment (namely, ξ_{TEI}, ξ_{IPR}, ξ_{BD} and ξ_{PCC}) have been compared with ξ_{QMI} and the negativity $N(\rho_{AB})$, defined in Eq. 1.41. (Negativity has been computed from density matrices obtained from the experiment [40], without using the tomographic approach).

The following observations can be made. The gross features of ξ_{TEI}, ξ_{QMI} and $N(\rho_{AB}$ are in agreement with each other (Fig. 6.10a).[4] As expected, ξ_{TEI} is closer to ξ_{QMI} owing to the similarity in their definitions. Also ξ_{BD} and ξ_{IPR} display trends similar to ξ_{TEI} (Fig. 6.10b, c). Surprisingly, the indicator ξ_{PCC}, that captures only linear correlations, performs well and agrees reasonably with $N(\rho_{AB})$ (Fig. 6.10d). This is an unanticipated result, in the light of the inferences from the previous chapters on entanglement in CV and HQ systems. Agreement between the two curves corresponding to the experimental data and the theoretical prediction follows a trend similar to that in the case of squeezing discussed earlier. Once again the results emphasize the advantages of adopting the tomographic approach.

[4] Figures 6.10, 6.11, 6.12, 6.13, 6.14 and 6.15 are reproduced from *Tomographic entanglement indicators from NMR experiments*, Sharmila et al. [39] with permission from AIP Publishing.

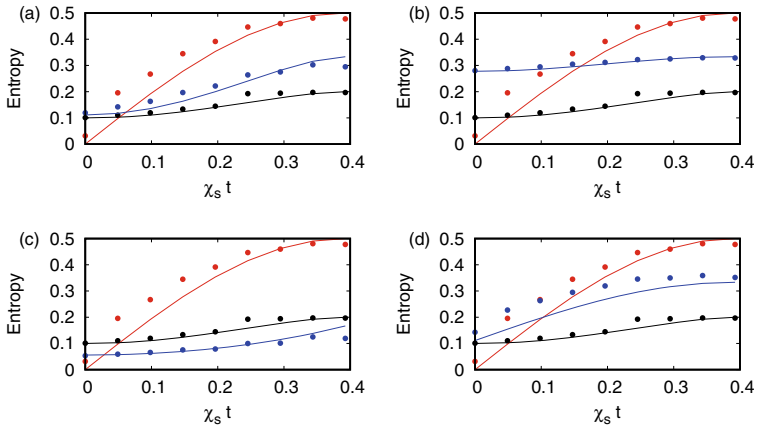

Fig. 6.10 $N(\rho_{AB})$ (red), 0.1 ξ_{QMI} (black), and **a** ξ_{TEI} (blue), **b** ξ_{IPR} (blue), **c** ξ_{BD} (blue), **d** ξ_{PCC} (blue) versus scaled time $\chi_s t$. The solid curves are computed using Eq. 6.19 and the dotted curves from experimental data. Figures are reproduced from [39]

To estimate squeezing, tomograms obtained from all the 9 basis sets, namely, xx, xy, xz, yx, yy, yz, zx, zy, and zz are necessary. However, in the case of entanglement, we have verified that the bipartite entanglement indicators ξ_{TEI} computed with all the 9 basis sets, and ξ'_{TEI}, obtained with just the 6 slices corresponding to xx, xy, xz, yx, yy, and yz, are in good agreement with each other. Such a reduction in the number of tomographic slices is however not possible while computing the IPR based indicator. It turns out that ξ_{IPR} computed with the full basis set is not in reasonable agreement with the corresponding indicator obtained with lesser tomographic slices. It now remains to be seen if such a reduction of slices is possible in NMR experiment II, which we will discuss further on.

Returning to the problem at hand, Fig. 6.11a, b facilitate comparison between $[1 - 2(\Delta J_{\text{min}})^2]$, $[1 - 8(\Delta \mathcal{J}_{\text{min}})^2]$, $N(\rho_{AB})$, ξ_{TEI}, and ξ_{QMI}. It is clear that $N(\rho_{AB})$ characterizes the degree of squeezing and higher-order squeezing extremely well. ξ_{TEI} and ξ_{QMI} estimate the extent of squeezing to a much lesser degree. From Fig. 6.12a, b it is clear that ξ_{PCC} compares well with $[1 - 2(\Delta J_{\text{min}})^2]$, $[1 - 8(\Delta \mathcal{J}_{\text{min}})^2]$, and $N(\rho_{AB})$. The general behavior of $N(\rho_{AB})$ is mirrored in the trends shown by the variances and covariances. Further, ξ_{TEI} reflects the trends in ξ_{QMI}. From Fig. 6.13 where ξ_{TEI}, ξ_{QMI}, and $N(\rho_{AB})$ are compared with the discord $D(A : B)$ (Eq. 1.42), it can be seen that ξ_{TEI} agrees well with both ξ_{QMI}, and $D(A : B)$. However, our calculations also reveal that ξ_{PCC} does not capture the trends seen in the discord. It is important to note that entanglement dynamics captured by two standard entanglement measures, such as negativity and discord, do not share completely identical trends. In the light of this observation, even the current level of efficacy of the tomographic indicators is both interesting and useful.

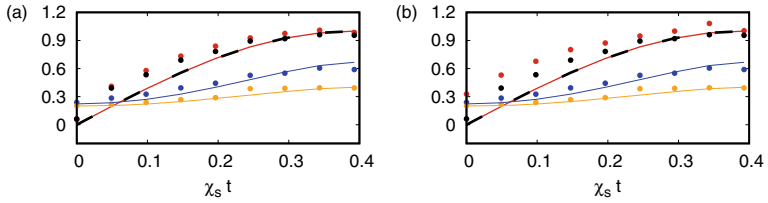

Fig. 6.11 $2\,N(\rho_{AB})$ (black), $2\,\xi_{\text{TEI}}$ (blue), $0.2\,\xi_{\text{QMI}}$ (orange), and **a** $[1-2(\Delta J_{\text{min}})^2]$ (red), **b** $[1-8(\Delta \mathcal{J}_{\text{min}})^2]$ (red), versus scaled time $\chi_s t$. The solid curves are computed using Eq. 6.19 and the dotted curves from experimental data. Figures are reproduced from [39]

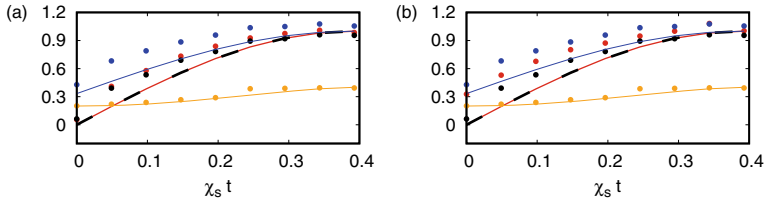

Fig. 6.12 $2\,N(\rho_{AB})$ (black), $3\,\xi_{\text{PCC}}$ (blue), $0.2\,\xi_{\text{QMI}}$ (orange), and **a** $[1-2(\Delta J_{\text{min}})^2]$ (red), **b** $[1-8(\Delta \mathcal{J}_{\text{min}})^2]$ (red), versus scaled time $\chi_s t$. The solid curves are computed using Eq. 6.19 and the dotted curves from experimental data. Figures are reproduced from [39]

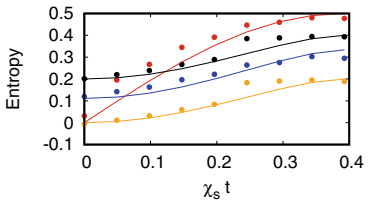

Fig. 6.13 $N(\rho_{AB})$ (red), $0.2\,\xi_{\text{QMI}}$ (black), ξ_{TEI} (blue), and $0.2\,D(A:B)$ (orange) versus scaled time $\chi_s t$. The solid curves are computed using Eq. 6.19 and the dotted curves from experimental data. Figures are reproduced from [39]

6.5.2 *Blockade and Freezing in Nuclear Spins*

We now proceed to examine NMR experiments II and III. Here, the systems comprise N spin qubits ($N = 2$ for II and $N = 3$ for III) that evolve in time, as in the earlier case. In NMR experiment II, each qubit is a subsystem, while in experiment III, one subsystem comprises two qubits and the other has a single qubit. The effective Hamiltonian for N qubits is

$$H_N = \sum_{i=1}^{N} (\omega_i \sigma_{ix} - \Omega_i \sigma_{iz}) + \sum_{i=1}^{N-1} \sum_{j=i+1}^{N} \lambda_{ij} \sigma_{iz} \sigma_{jz}, \tag{6.20}$$

where ω_i, Ω_i and λ_{ij} are constants, σ_x and σ_z are the usual spin matrices, and the subscripts i, j label the qubits.

The initial density matrix is

$$\rho_N(0) = \left(\frac{1-\epsilon}{2^N}\right)\mathbb{I}_N + \epsilon|\psi\rangle\langle\psi|, \tag{6.21}$$

where $\mathbb{I}_N$ is the $(2^N \times 2^N)$ unit matrix, $|\psi\rangle = |\downarrow\rangle^{\otimes N}$, and ϵ is the purity of the state.

As in the earlier experiment ξ_{TEI}, ξ_{IPR} and ξ_{BD} are computed from the corresponding tomograms, and compared with the discord. We also comment on the spin squeezing properties.

NMR Experiment II

The experiment has been performed [41] using the nuclear spins of ^{19}F and ^{31}P, regarded as the respective subsystems 1 and 2, in NaFP. For $N = 2$, the numerical computation has been carried out setting $\lambda_{12}/(2\pi) = 868$ Hz, and $\Omega_1 = \Omega_2 = \lambda_{12}/2$. Three cases have been examined, namely, (i) $\omega_1/(2\pi) = 217$ Hz, $\omega_2 = \omega_1$ (which describes the blockade condition), (ii) $\omega_2/(2\pi) = 217$ Hz, $\omega_1 = \omega_2/4$, and (iii) $\omega_1/(2\pi) = 217$ Hz, $\omega_2 = \omega_1/4$, (which describe freezing as detailed in [41]). In contrast to the earlier experiment considered, the mean spin direction is not a null vector for this system. A procedure similar to what has been prescribed earlier to compute indicators of entanglement and squeezing properties has been followed in Cases (i) and (ii). This indicates that all the numerically simulated tomographic entanglement indicators are in good agreement with the discord. Further, in contrast to NMR experiment I, trends in spin squeezing and discord agree well. The variance computed from both the experimentally reconstructed and the numerically simulated density matrices are in good agreement. The small discrepancies between them can be interpreted as arising from reconstruction errors. However, the tomographic indicators computed from the experiment and simulations do not match well. This is especially so for low purity states. The inferences drawn from Case (iii) are identical to those of Case (ii).

A reduction in the number of tomographic slices in computing ξ_{TEI}, ξ_{IPR}, and ξ_{BD} is ineffective. Since the extent of discord in NMR experiment I is in the range [0, 1], whereas in NMR experiment II it is significantly smaller (the typical range is $[0, 10^{-8}]$), it appears that ξ'_{TEI} is a reliable entanglement indicator only for sufficiently strong bipartite entanglement. This is corroborated by the investigations on NMR experiment III.

NMR Experiment III

This three-qubit experiment has been performed using the nuclear spins of ^{13}C, ^{1}H and ^{19}F (treated as subsystems 1, 2 and 3 respectively) in the DBFM molecule, which is the same system as in NMR experiment I. The system Hamiltonian is given by Eq. 6.20. The initial density matrix obtained by setting $N = 3$ in Eq. 6.21 was evolved

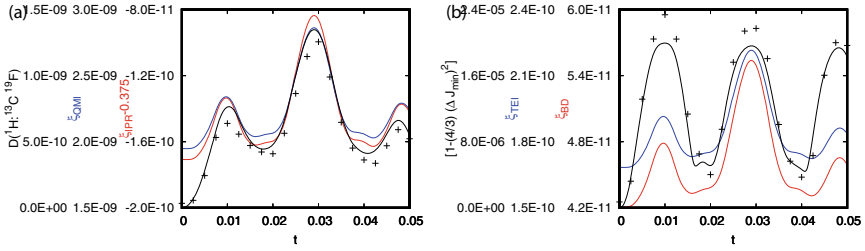

Fig. 6.14 **a** $D(^1\mathrm{H} : ^{13}\mathrm{C}\ ^{19}\mathrm{F})$ (black), ξ_{QMI} (blue), and ξ_{IPR} (red) versus time t in seconds, and **b** $[1-(4/3)(\Delta J_{\mathrm{min}})^2]$ (black), ξ_{TEI} (blue), and ξ_{BD} (red) versus time t in seconds for Case (C). The solid curves are computed by numerical simulation and the crosses from experimental data. Figures are reproduced from [39]

numerically. The parameter values used for computations are as follows: $\lambda_{12}/(2\pi) = 224.7$ Hz, $\lambda_{13}/(2\pi) = -311.1$ Hz, $\lambda_{23}/(2\pi) = 49.7$ Hz, $\Omega_1 = (\lambda_{12}+\lambda_{13})/2$, $\Omega_2 = (\lambda_{12}+\lambda_{23})/2$ and $\Omega_3 = (\lambda_{13}+\lambda_{23})/2$. The cases examined are (A) $\omega_1/(2\pi) = 10$ Hz, $\omega_1 = \omega_2 = \omega_3$ [bipartite entanglement between subsystems (1) and (2,3)], (B) $\omega_1/(2\pi) = 50$ Hz, $\omega_1 = 5\omega_2 = 5\omega_3$ [bipartite entanglement between subsystems (1) and (2,3)], (C) $\omega_2/(2\pi) = 50$ Hz, $\omega_2 = 5\omega_1 = 5\omega_3$ [bipartite entanglement between subsystems (2) and (1,3)], and (D) $\omega_1/(2\pi) = 50$ Hz, $\omega_1 = \omega_2 = 5\omega_3$ [bipartite entanglement between subsystems (1,2) and (3)]. In this case, the spin operator

$$\begin{aligned}\mathbf{J}_3 =&(\sigma_{1x}+\sigma_{2x}+\sigma_{3x})\mathbf{e_x}+(\sigma_{1y}+\sigma_{2y}+\sigma_{3y})\mathbf{e_y}\\&+(\sigma_{1z}+\sigma_{2z}+\sigma_{3z})\mathbf{e_z}\end{aligned}$$

is used instead of $\mathbf{J}_2$, and $(\Delta J_{\mathrm{min}})^2 < 0.75$ implies spin squeezing.

Plots of the entanglement indicators and squeezing as a function of time reveal the following. As in NMR experiments I and II, in Cases (A) and (B) of experiment III, the gross features of entanglement are reflected in the indicators. In contrast to experiment I, and similar to experiment II, spin squeezing agrees with discord in Cases (A) and (B). The numerical simulations and the experimentally reconstructed density operators give results on the discord which are in agreement.

All 27 tomographic sections were used to compute the tomographic entanglement indicators, the discord, $[1-(4/3)(\Delta J_{\mathrm{min}})^2]$ and ξ_{QMI}. Figures 6.14 and 6.15, corresponding to Cases C and D indicate that as before ξ_{TEI}, ξ_{IPR} and ξ_{BD} agree with the discord. However, as in the case of NMR experiment 1, $[1-(4/3)(\Delta J_{\mathrm{min}})^2]$ and the discord do not match effectively.

An unanticipated result arises from the investigations in Case (D). Here, during temporal evolution, ξ_{TEI}, ξ_{BD} and spin squeezing do not mimic the discord. However, ξ_{IPR} and the discord match well with each other. As in NMR experiment II, the bipartite entanglement is weak, and efficient reduction in the number of tomographic sections is not possible.

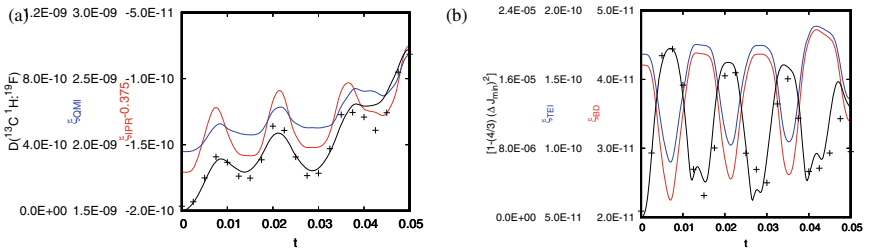

Fig. 6.15 **a** $D(^{13}\mathrm{C}\ ^{1}\mathrm{H} : ^{19}\mathrm{F})$ (black), ξ_{QMI} (blue), and ξ_{IPR} (red) versus time t in seconds, and **b** $[1-(4/3)(\Delta J_{\mathrm{min}})^2]$ (black), ξ_{TEI} (blue), and ξ_{BD} (red) versus time t in seconds for Case (D). The solid curves are computed by numerical simulation and the crosses from experimental data. Figures are reproduced from [39]

Inferences Drawn from the NMR Experiments

In direct contrast to our inferences from earlier investigations, in NMR experiment I in which the state considered is a *mixed* bipartite state, ξ_{PCC} is in good agreement with spin squeezing and the negativity $N(\rho_{AB})$, although not with the discord. Results from both the NMR experiments I and II indicate that all other tomographic entanglement indicators are in good agreement with the discord. We have further shown that novel features could arise when a tripartite system is partitioned into two subsystems and bipartite entanglement examined, as is revealed by Case (D) of NMR experiment III. Thus, the performance of entanglement indicators, and the extent to which these indicators and spin squeezing track the discord during dynamical evolution of multipartite systems, are very sensitive to the precise manner in which the full system is partitioned into subsystems, as well as to features such as blockade and spin freezing.

Our investigations on these three systems provide some preliminary pointers on the efficacy of identifying an optimal subset of tomographic slices for the computation of the corresponding bipartite entanglement indicator ξ'_{TEI}. If the entanglement is sufficiently strong (NMR experiment I), a subset of tomographic slices suffices. From the experimental point of view, this would permit a corresponding reduction in the number of measurements. However, if the entanglement is weak (NMR experiments II and III), the full set of tomographic slices needs to be used. A relevant question is whether the closeness of ξ'_{TEI} to ξ_{TEI} implies strong bipartite entanglement. More detailed investigations need to be carried out before this question can be answered definitively.

6.6 Concluding Remarks

In this chapter we have examined a wide spectrum of phenomena associated with bipartite entanglement, as the state of the composite system evolves in time. The illustrative examples considered include both HQ and spin systems modeled by

appropriate effective Hamiltonians. In the case of spin systems, actual data from three NMR experiments have been examined in detail from the tomographic point of view and conclusions drawn about the entanglement and spin squeezing properties. This investigation provides pointers to the differences in the performance of tomographic indicators in qubit/spin systems and HQ systems of light-matter interaction. In all cases the full system is considered to be a composite of only two subsystems.

The investigations on HQ systems reported in this chapter reveal the importance of the role played by the finiteness of the number of atomic levels, in contrast to the effects seen when the atom is modeled as an oscillator; the effect of more than one atom or field in either subsystem on the entanglement dynamics; the efficacy of tomographic indicators; the possibility of the occurrence of ESD and the subsequent birth of entanglement in specific models; the peculiar effects that arise if tunable IDCs are present in the Hamiltonian; the role played by the precise initial conditions and parameter values in the temporal changes in the extent of entanglement; the appearance of bifurcation cascades in the short-time regime; and so on. The mean photon number is seen to mimic the dynamics of the entanglement indicator. This opens up the possibility of examining the dynamics of this observable over both short and long time scales. The latter is done by carrying out a detailed time series analysis, using tools from classical dynamical systems theory. This is the theme of Chap. 7.

References

1. M. Yönaç, T. Yu, J. Eberly, J. Phys. B: At. Mol. Opt. Phys. **39**, S621 (2006)
2. Z.X. Man, Y.J. Xia, N.B. An, Eur. Phys. J. D. **53**, 229 (2009)
3. P. Laha, S. Lakshmibala, V. Balakrishnan, J. Opt. Soc. Am. B **36**, 575–584 (2019). http://opg.optica.org/josab/abstract.cfm?URI=josab-36-3-575, https://doi.org/10.1364/JOSAB.36.000575
4. A. Shankar, S. Lakshmibala, V. Balakrishnan, J. Phys. B: At. Mol. Opt. Phys. **47**, 215505 (2014)
5. P. Laha, B. Sudarsan, S. Lakshmibala, V. Balakrishnan, Int. J. Theor. Phys. **55**, 4044 (2016)
6. IBM Quantum. https://quantum-computing.ibm.com/
7. W.K. Wooters, Phys. Rev. Lett. **80**, 2245 (1998)
8. E. Joos, H.D. Zeh, C. Kiefer, D. Giulini, K. Kupsch, I.-O. Stamatescu, *Decoherence and the Appearance of a Classical World in Quantum Theory* (Springer, Germany, 2003)
9. B. Sharmila, S. Lakshmibala, V. Balakrishnan, Quantum Inf. Process. **18**, 236 (2019)
10. B. Sharmila, S. Lakshmibala, V. Balakrishnan, Quantum Inf. Process. **19**, 127 (2020). https://doi.org/10.1007/s11128-020-02625-5
11. C.J. Hood, M.S. Chapman, T.W. Lynn, H.J. Kimble, Phys. Rev. Lett. **80**, 4157 (1998)
12. A.N. Cleland, M.L. Roukes, Appl. Phys. Lett. **69**, 2653 (1996)
13. D.F. James, J. Jerke, Can. J. Phys. **85**, 625 (2007)
14. Q.H. Liao, W.J. Nie, J. Xu, Y. Liu, N.R. Zhou, Q.R. Yan, A. Chen, N.H. Liu, M.A. Ahmad, Laser Phys. **26**, 055201 (2016)
15. J.P. Marangos, J. Mod. Opt. **45**, 471 (1998)
16. M. Fleischhauer, A. Imamoglu, J.P. Marangos, Rev. Mod. Phys. **77**, 633 (2005)
17. W.R. Kelly, Z. Dutton, J. Schlafer, B. Mookerji, T.A. Ohki, J.S. Kline, D.P. Pappas, Phys. Rev. Lett. **104**, 163601 (2010)

18. P.M. Anisimov, J.P. Dowling, B.C. Sanders, Phys. Rev. Lett. **107**, 163604 (2011)
19. A. Lazoudis, T. Kirova, E.H. Ahmed, P. Qi, J. Huennekens, A.M. Lyyra, Phys. Rev. A **83**, 063419 (2011)
20. B. Peng, A.K. Ozdemir, W. Chen, F. Nori, L. Yang, Nat. Commun. **5**, 5082 (2014)
21. S. Sivakumar, Int. J. Theor. Phys. **43**, 2405 (2004)
22. P. Laha, S. Lakshmibala, V. Balakrishnan, Europhys. Lett. **125**(6), 60005 (2019). https://doi.org/10.1209/0295-5075/125/60005
23. H. Kampermann, W.S. Veeman, J. Chem. Phys. **122**, 214108 (2005)
24. I.A. Silva, J.G. Filgueiras, R. Auccaise, A.M. Souza, R. Marx, S.J. Glaser, T.J. Bonagamba, R.S. Sarthour, I.S. Oliveira, E.R. deAzevedo, NMR contributions to the study of quantum correlations, in *Lectures on General Quantum Correlations and Their Applications*, ed. by F.F. Fanchini, D.d.O. Soares Pinto, G. Adesso (Springer, Cham, 2017), pp. 517–542
25. S. Sinha, J. Emerson, N. Boulant, E.M. Fortunato, T.F. Havel, D.G. Cory, Quantum Inf. Process. **2**, 433 (2003)
26. R. Auccaise, A.G. Araujo-Ferreira, R.S. Sarthour, I.S. Oliveira, T.J. Bonagamba, I. Roditi, Phys. Rev. Lett. **114**, 043604 (2015)
27. R. Laflamme, E. Knill, W.H. Zurek, P. Catasti, S.V.S. Mariappan, Phil. Trans. R. Soc. A **356**, 1941 (1998)
28. G. Teklemariam, E.M. Fortunato, M.A. Pravia, Y. Sharf, T.F. Havel, D.G. Cory, A. Bhattaharyya, J. Hou, Phys. Rev. A **66**, 012309 (2002)
29. J. Filgueiras, T.O. Maciel, R. Auccaise, R.O. Vianna, R.S. Sarthour, I.S. Oliveira, Quantum Inf. Process. **11**, 1883 (2012)
30. J. Teles, E. R. deAzevedo, R. Auccaise, R. S. Sarthour, I. S. Oliveira, and T. J. Bonagamba, J. Chem. Phys. **126**, 154506 (2007)
31. D. Zanuttini, I. Blum, L. Rigutti, F. Vurpillot, J. Douady, E. Jacquet, P.-M. Anglade, B. Gervais, J. Chem. Phys. **147**, 164301 (2017)
32. J.-S. Lee, Phys. Lett. A **305**, 349 (2002)
33. T. Baumgratz, A. Nüßeler, M. Cramer, M.B. Plenio, New J. Phys. **15**, 125004 (2013)
34. J. G. Titchener, M. Gräfe, R. Heilmann, A. S. Solntsev, A. Szameit, and A. A. Sukhorukov, npj Quantum Inf. **4**, 19 (2018)
35. D. Gross, Y.-K. Liu, S.T. Flammia, S. Becker, J. Eisert, Phys. Rev. Lett. **105**, 150401 (2010)
36. W.-T. Liu, T. Zhang, J.-Y. Liu, P.-X. Chen, J.-M. Yuan, Phys. Rev. Lett. **108**, 170403 (2012)
37. A. Steffens, C. Riofrío, W. McCutcheon, I. Roth, B.A. Bell, A. McMillan, M. Tame, J. Rarity, J. Eisert, Quantum. Sci. Technol. **2**, 025005 (2017)
38. X. Chai, Y.-P. Lu, A.-N. Zhang, Q. Zhao, Phys. Rev. A **99**, 042321 (2019)
39. B. Sharmila, V.R. Krithika, S. Pal, T.S. Mahesh, S. Lakshmibala, V. Balakrishnan, J. Chem. Phys. **156**(15), 154102 (2022). https://doi.org/10.1063/5.0087032
40. S. Pal, P. Batra, T. Krisnanda, T. Paterek, T.S. Mahesh, Quantum **5**, 478 (2021)
41. V.R. Krithika, S. Pal, R. Nath, T.S. Mahesh, Phys. Rev. Research **3**, 033035 (2021)
42. M.H. Levitt, *Spin Dynamics: Basics of Nuclear Magnetic Resonance* (Wiley, New York, 2001)
43. H. Maassen, J.B.M. Uffink, Phys. Rev. Lett. **60**, 1103 (1988)

Chapter 7
Dynamics of the Mean Photon Number: Time Series and Network Analysis

7.1 Introduction

In Chap. 6, we discussed at length a variety of novel effects that arise in the bipartite entanglement dynamics in generic CV and HQ models. The mean photon number was shown to embody some of these effects, such as the bifurcation cascade that is seen in the short-time regime as the intensity-dependent coupling between the field and a three-level atom is fine tuned. This experimentally relevant observable is therefore ideally suited for a detailed time series analysis. The procedure also opens up a new approach in understanding the validity of known results from classical dynamical systems theory, when the quantum observable is treated akin to a classical dynamical variable. The central idea, as mentioned in Chap. 1, is to consider a 'phase space' of expectation values of appropriate quantum observables, obtain their long-time behavior and ergodicity properties by calculating the Lyapunov spectra, construct return maps and recurrence plots, and carry out an analysis of the recurrence time statistics. It is evident that when a state revives periodically, all expectation values of relevant observables return to their initial values at the instants of revival, thus leading to periodic returns of orbits in the phase space of these observables. Such revivals, however, do not occur in most cases. We recall, for instance, that in the model of the radiation field interacting with a multilevel atom, for an initial product state of the coherent field $|\alpha\rangle$ and an atomic state, the entanglement becomes nearly zero *only* for small values of $|\alpha|^2$. If the numerical value of $|\alpha|^2$ is sufficiently large, or when the field is initially an m-PACS, the entanglement saturates to a nonzero value. The corresponding phase space orbit is not periodic. The time series analysis of quantum observables is a procedure to investigate how the precise nature of the initial field state affects the ergodicity properties of the dynamical variable considered. Further, this procedure brings to light the sensitivity of these properties to the interplay between the couplings and the nonlinearities that are effective in the system.

For ease of understanding, we start in Sect. 7.2 with an outline of the main aspects of time series analysis. Following this, we investigate the time series corresponding to the specific models that have been introduced in earlier chapters. In Sect. 7.3,

© The Author(s), under exclusive license to Springer Nature Switzerland AG 2022

S. Lakshmibala and V. Balakrishnan, *Nonclassical Effects and Dynamics of Quantum Observables*, SpringerBriefs in Physics,
https://doi.org/10.1007/978-3-031-19414-6_7

we examine the model of a radiation field interacting with a multilevel atom, and identify how the extent of departure from coherence of the initial field state and the strength of the nonlinearity vis-à-vis that of the interaction, is responsible for the nature of the 'orbits' in the phase space of the observables. In Sect. 7.4, we consider the V-type atom interacting with one or two radiation fields, from the perspective of dynamical systems theory. In Sect. 7.5, we investigate the dynamics of a Λ-type atom interacting through an intensity-dependent coupling with two radiation fields. A time series of the mean photon number of either field is analysed to understand the manner in which the ergodicity properties of the observable are affected by the field-atom coupling. We also construct a network with a small subset of this long time series, and investigate its properties. This facilitates the identification of network quantifiers that mirror the results gleaned from the time series analysis.

7.2 Brief Overview of Time Series Analysis

For our purposes, we shall only invoke the machinery of time series analysis for data pertaining to a single observable (for instance, the mean photon number corresponding to a single-mode radiation field). Extension of the procedure to the analysis of a long time series of more than one signal or observable is well documented in the literature (see, for instance, [1]), although in practice such data may not be accessible readily for *all* the observables involved in the dynamics of a given system. The time evolution of the relevant set of dynamical variables is typically given by a set of coupled equations which are nonlinear. The aim of the time series analysis is to extract information from the available data set, namely, values of the measured/accessible observables and their delayed copies, about the *effective* number of variables that are relevant to describe the temporal evolution. This is in fact the effective dimensionality $d_{\rm emb}$ of the 'phase space' of the relevant variables, referred to as the embedding dimension. With a further increase in the phase space dimension beyond $d_{\rm emb}$, the important features of the dynamics do not change. Thus $d_{\rm emb}$ is in fact the minimum number of dimensions that is required for a 'true' description of the dynamics. It is evident that this effective phase space is only formally equivalent to the actual phase space of the system, and in a sense mimics the dynamical features present in the latter space. The technique has been very successful in leading to an understanding of the ergodicity properties of classical dynamical variables, ranging from regular or quasi-regular motion to fully developed chaos, thus providing an incentive to examine the efficacy of such an analysis when applied to the temporal data of quantum systems.

The procedure to identify the embedding dimension $d_{\rm emb}$ is indicated in the embedding theorem [2]. This is carried out through the following steps. One first assumes a trial value d for $d_{\rm emb}$, and from the (already known) time series data generates d dynamical variables. For this purpose, we need to identify a *time delay* τ such that data points separated by time intervals $\geq \tau$ are sufficiently independent of each other, so that they can be considered to be the independent dynamical variables. Con-

sider two data points $s(n)$ and $s(n+T)$ at discrete times n and $(n+T)$ (in units of time step δt) which are essentially independent of each other (for sufficiently large T). Any information on $s(n)$ obtained from the measured value of $s(n+T)$ must evidently tend to zero. Equivalently, let $p\big(s(n)\big)$ and $p\big(s(n+T)\big)$ be the individual probability densities for obtaining the values $s(n)$ and $s(n+T)$ at times n and $(n+T)$, respectively, and $p\big(s(n)\,,\,s(n+T)\big)$ the corresponding joint probability density. The average mutual information $I(T)$ is then given by

$$I(T) = \sum_{s(n)\,,\,s(n+T)} p\big(s(n), s(n+T)\big)\,\log_2\Big[\frac{p\big(s(n)\,,\,s(n+T)\big)}{p\big(s(n)\big)\,p\big(s(n+T)\big)}\Big]. \tag{7.1}$$

It is evident that $I(T)$ should tend to zero for sufficiently large T. A popular prescription for identifying τ [3] is to select that value of T at which the first minimum in $I(T)$ occurs.

Next, vectors are constructed in the effective phase space. We denote by $s(0),\ s(1),\ s(2), \ldots$ the time series of the signal obtained at discrete times $t = 0,\ 1,\ 2,\ \ldots$. At $t = 0$, the phase space vector $\mathbf{s}_0$ has components $s(0),\ s(\tau),\ s(2\tau),\ \ldots,\ s((d-1)\tau)$. This vector evolves after one time step to $\mathbf{s}_1$ whose components are $s(1),\ s(1+\tau),\ s(1+2\tau),\ \ldots,\ s(1+(d-1)\tau)$, and so on. This procedure is repeated over many time steps, so as to reconstruct sets of time-delayed vectors in the d-dimensional phase space. Each vector defines a point in the space. Taken in the correct sequence, these points describe the dynamical evolution in that space. This procedure is repeated for different pre-selected values of d. The next step in the program is to identify that value of d which corresponds to $d_{\rm emb}$. This is done by evaluating the correlation integral

$$C(r) = \lim_{n\to\infty} \frac{1}{n^2} \sum_{i,j=0}^{n-1} \theta\,(r - |\mathbf{s}_i - \mathbf{s}_j|) = \int_0^r d^d r'\, c(\mathbf{r}')\,. \tag{7.2}$$

The integrand $c(\mathbf{r}')$ itself is the standard correlation function. $C(r)$ provides an estimate of the average correlation between the various points in a phase space corresponding to a given dimension d. We recall that this space contains n points generated from the data set, where n is sufficiently large. It can be deduced [4] that, for sufficiently small r, $C(r)$ scales like a power r^{ζ} of r; moreover, as the value of d approaches the correct minimum embedding dimension $d_{\rm emb}$, the exponent ζ will not change with an increase in d beyond $d_{\rm emb}$. This feature determines the exact value of $d_{\rm emb}$. It must be emphasized that, while $d_{\rm emb}$ could be much smaller than the dimension of the actual phase space of the system considered, the dynamics of the effective variables *alone*, in the phase space of dimensionality $d_{\rm emb}$, should suffice to extract both qualitative and quantitative information about the extent of chaos in the signal.

Our aim here is to assess whether the mean photon number in the CV and HQ models that we have considered exhibits exponential sensitivity to the actual initial

state, the system parameters, the extent of nonlinearity, etc., thus resulting in 'chaotic' behavior. This is done by calculating the maximal Lyapunov exponent (MLE) in the reconstructed phase space of dimensionality d_{emb} . There are, in general, d_{emb} Lyapunov exponents corresponding to the dynamics in this space. We will be concerned with the largest of these exponents, namely, $\lambda_{\max}$, since a positive value of $\lambda_{\max}$ is indicative of chaotic behavior of the quantum observable, over a long time. The algorithm used by us to estimate $\lambda_{\max}$ from data sets represented by time series is provided in [5, 6]. We outline this algorithm as follows. Consider the set of 'distances' $\{d_j(0)\}$, where $d_j(0)$ is the separation between the jth pair of nearest neighbors in the phase space. At a later time time $t = k\,\delta t$, where k is a positive nonzero integer, this evolves to $\{d_j(k)\}$. If $\langle \ln\, d_j(k)\rangle$ (the angular brackets denote the average over all values of j) is plotted against $k\,\delta t$, the generic curve has an initial transient region over a short time interval, followed by a long, linear region. It then saturates for long times. The slope of the linear region is the MLE $\lambda_{\max}$. If d_{emb} is obtained correctly, any further increase in the dimensionality of the reconstructed phase space should not alter the inferences made regarding the exponential instability, if any, of the system.

Results on the ergodicity properties of the observable are augmented wherever possible by qualitative features that emerge from an analysis of return maps, recurrence plots and recurrence time statistics. With this summary of the relevant aspects of time series analysis, we proceed in the next section to carry out a detailed time series analysis of the numerically obtained data of the mean photon number in the bipartite atom-field interaction model.

7.3 The Bipartite Atom-Field Interaction Model: Time Series Analysis

7.3.1 Dynamics

We recall that the Hamiltonian is given by Eq. (4.38), namely,

$$H_{\text{AF}} = \omega_F a^\dagger a + \omega_A b^\dagger b + \gamma {b^\dagger}^2 b^2 + g(a^\dagger b + a b^\dagger). \tag{7.3}$$

We first mention the important features pertaining to the *classical* counterpart of this Hamiltonian. The quantum case, which we will analyze subsequently, shows features that are in contrast with the results in the classical context. Since the model pertains to two interacting oscillators the classical Hamiltonian is obtained, by associating with a and $a^\dagger$, an oscillator with mass m, position x and linear momentum p_x . Likewise, the 'atomic' oscillator with ladder operators b and $b^\dagger$ has mass M, position y and momentum p_y . It can then be seen that the only consistent way in which a nontrivial finite expression for the Hamiltonian can be obtained in the classical limit is to let $\hbar$ and γ simultaneously tend to zero with the ratio $\gamma/\hbar$ tending to a finite value $\overline{\lambda}$. The classical Hamiltonian is then given by

$$H_{\rm cl} = \frac{p_x^2}{2m} + \frac{1}{2}m\omega_F^2 x^2 + \frac{p_y^2}{2M} + \frac{1}{2}M\omega_A^2 y^2 + \frac{\overline{\lambda}}{\omega_A^2}\left(\frac{p_y^2}{2M} + \frac{1}{2}M\omega_A^2 y^2\right)^2 + \frac{g}{\sqrt{\omega_F\omega_A}}\left(\sqrt{mM}\,\omega_F\omega_A\, xy + \frac{p_x\, p_y}{\sqrt{mM}}\right). \tag{7.4}$$

The canonical Poisson bracket relations $\{x\,,\ p_x\} = \{y\,,\ p_y\} = 1$ are preserved. It can be verified that apart from the Hamiltonian the counterpart of $\mathsf{N}_{\rm tot} = a^\dagger a + b^\dagger b$, given by

$$N_{\rm cl} = \frac{1}{\omega_F}\left(\frac{p_x^2}{2m} + \frac{1}{2}m\omega_F^2 x^2\right) + \frac{1}{\omega_A}\left(\frac{p_y^2}{2M} + \frac{1}{2}M\omega_A^2 y^2\right), \tag{7.5}$$

is a second, analytic, constant of the motion. As a consequence, this two-freedom system is Liouville-Arnold integrable. The motion in this ellipsoidal four-dimensional phase space is bounded for all initial conditions. The system being classically integrable, all the Lyapunov exponents are zero, implying non-chaotic motion in any phase space direction on a 2-torus.

7.3.2 *Power Spectrum and Lyapunov Exponent*

The mean photon number $a^\dagger a$ is treated as the dynamical variable, and its time series numerically obtained in this model for illustrative purposes. The ergodicity properties of this observable are analyzed for different values of γ/g. As before, the atomic oscillator is taken to be in its ground state initially, and the field in a CS or a PACS. Detailed investigations [7] reveal the following features.

For weak nonlinearity (say, $\gamma = 1$ and $g = 100$) it has been shown that, with increasing departure from coherence of the initial field state, there is an increase in the number of frequencies seen in the power spectrum (i.e., in the Fourier transform of the autocorrelation function of the observable). Further, for a given initial state, the number of characteristic frequencies in the power spectrum increases with an increase in $\nu = |\alpha|^2$.

For strong nonlinearity compared to the interaction strength ($\gamma/g \gtrsim 1$), the dynamics ranges from quasiperiodicity to fully-developed chaos, depending on the precise initial state considered. For example, if the field is initially in a CS with $\nu = 1$, both the time series analysis and the power spectrum reveal that the dynamics of the mean photon number is not chaotic. In contrast to this, if the initial field state is a PACS $|\alpha, m\rangle$ with a sufficiently large value of m, or a CS with a sufficiently high value of ν, chaotic behavior occurs. For $m = 5$, for instance, $d_{\rm emb} = 5$, and a plot of $\langle \ln\, d_j(k)\rangle$ versus time ($= k\delta t$, with the time step $\delta t = 10^{-1}$) yields a value ≈ 0.5 for the MLE $\lambda_{\rm max}$ (see Fig. 7.1[1]).

[1] Figures 7.1, 7.2 and Table 7.1 are reproduced from *Dynamics of quantum observables in entangled states*, Sudheesh et al. [7], with permission from Elsevier.

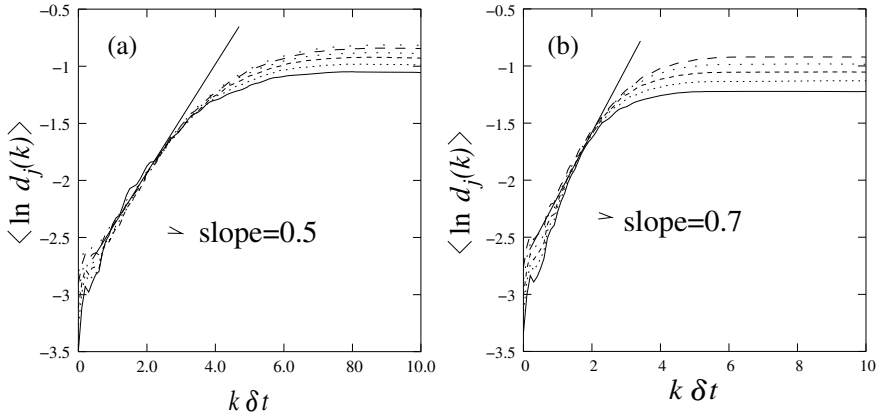

Fig. 7.1 $\langle \ln d_j(k) \rangle$ versus $t\ (= k\delta t)$, using the algorithm of Rosenstein et al. [5], for the initial states **a** $|(\alpha, 5); 0\rangle$ with $\gamma/g = 5$ and $\nu = 1$ and **b** $|\alpha; 0\rangle$ with $\gamma/g = 5$ and $\nu = 10$. The solid line corresponds to an embedding dimension $d_{\text{emb}} = 5$, and the dotted lines to values of d_{emb} from 6 to 10. These figures are reproduced from [7]

Table 7.1 Qualitative dynamical behavior of the mean photon number of a single-mode electromagnetic field interacting with a nonlinear medium

		Increasing departure from coherence → initial state		
		$\|\alpha; 0\rangle$	$\|(\alpha, 1); 0\rangle$	$\|(\alpha, 5); 0\rangle$
Increasing nonlinearity ↓	$\gamma/g = 10^{-2}$ $\nu = 1$	Regular	Regular	Regular
	$\gamma/g = 10^{-2}$ $\nu = 5$	Regular	Regular	Regular
	$\gamma/g = 5$ $\nu = 1$	Regular	Regular	$\lambda_{\max} \approx 0.5$
	$\gamma/g = 5$ $\nu = 5$	$\lambda_{\max} \approx 0.6$	$\lambda_{\max} \approx 0.7$	$\lambda_{\max} \approx 0.9$
	$\gamma/g = 5$ $\nu = 10$	$\lambda_{\max} \approx 0.7$	$\lambda_{\max} \approx 0.8$	$\lambda_{\max} \approx 1$

'Regular' $\Rightarrow \lambda_{\max} = 0$. The table is reproduced from [7]

The figures here also illustrate the appearance of the linear region in the plots after the initial transients have subsided, and before saturation occurs. Further, they confirm that an increase in d beyond the value 5 in this case does not change the dynamics, thus establishing that $d_{\text{emb}} = 5$.

The main inferences on the role played by the initial state and the parameter values on the subsequent evolution of the quantum observable are summarized in Table 7.1.

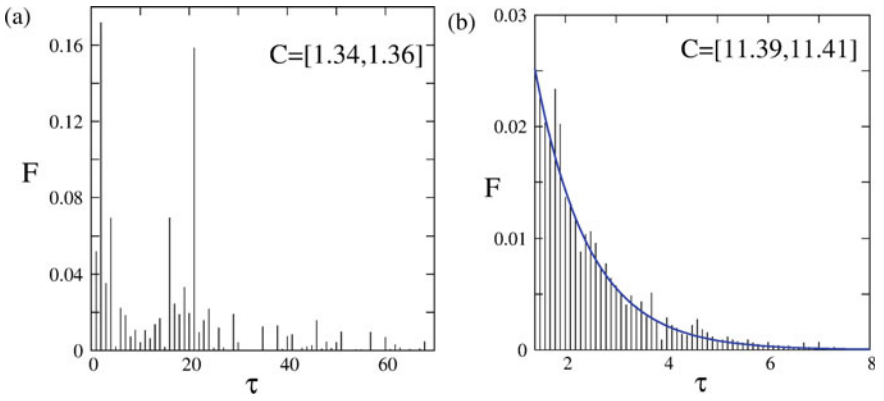

Fig. 7.2 First-recurrence-time distribution for the cell C from the time series of $\langle N(t)\rangle$, for **a** weak nonlinearity and **b** strong nonlinearity. These figures are reproduced from [7]

7.3.3 Recurrence Statistics

The findings in the foregoing are corroborated by analyzing another important characterizer of dynamical behavior: recurrence statistics of the coarse-grained dynamics of the observable, as represented by its time series. As the procedure involved in recurrence statistics will be used in subsequent sections, we explain its relevant features briefly. The idea is to coarse grain the effective phase space into cells of equal size, and numerically construct the invariant density (and hence the normalized stationary measure μ_0 for any generic cell C), as well as the distribution $F(\tau)$ of the time τ (in units of the time step) of the first recurrence or return to C. The mean recurrence time can then be calculated. A result that follows from the Poincaré recurrence theorem [8], assuming just ergodicity, is that the mean recurrence time is the reciprocal of the measure μ_0. Thus, a comparison between the numerically obtained mean recurrence time on the one hand, and the measure on the other, is used to decide if the dynamics is ergodic for all the initial states and parameter values considered. In the present instance, the cell size is 10^{-2} and the time interval considered is of the order of 10^5 to 10^6 time steps.

For illustrative purposes, consider two examples from the Table. The first corresponds to weak nonlinearity ($\gamma/g = 10^{-2}$, with the initial field state $|\alpha, 1\rangle$ and $\nu = 1$). This is an instance of regular dynamics of the mean photon number ($\lambda_{\max} = 0$). The corresponding first return time distribution is given in Fig. 7.2a.

This is a discrete distribution, indicative of quasiperiodic dynamics [9, 10]. In contrast, the first return distribution in Fig. 7.2b, which is well-fitted with an exponential distribution $\mu_0 e^{-\mu_0 \tau}$, corresponds to the case of strong nonlinearity, with $\gamma/g = 5$, initial field state $|\alpha, 1\rangle$, $\nu = 10$, and $\lambda_{\max} = 0.80$. This is the distribution expected of a hyperbolic system, for a sufficiently small cell size [11, 12]. With a longer time series of 10^7 steps, it can be confirmed numerically that two successive recurrences to a cell are uncorrelated, with a distribution $\mu_0^2 \tau e^{-\mu_0 \tau}$, the next term in

the Poisson distribution [13, 14], as expected from classical ergodic theory. We conclude from the analysis above that the predictions of classical ergodic theory for the recurrence time statistics of quasiperiodic and hyperbolic systems hold even for the quantum observable in the model considered (where its regular or chaotic dynamics is determined by whether $\lambda_{\max}$ is zero or positive). However, from the discussions in the preceding chapters, we know that the dynamics of HQ systems involving a finite number of atomic levels need not be similar to that of CV systems. We therefore proceed to examine the ergodic properties of the mean photon number in the model of the three-level atom interacting with one or more radiation fields.

7.4 Three-Level Atom Interacting with Radiation Fields

We begin by recalling from Chap. 6 the HQ model of a V-atom interacting with a single radiation field, in which signatures of the entanglement revival phenomena persisted even in the strong nonlinearity regime (this feature was in contrast to the situation in the case of the multilevel atom-field interaction model discussed in Chap. 5). The dynamics of the mean photon number has been investigated in this model in [15]. Using the procedure outlined above, we can readily demonstrate that the mean recurrence time to a phase space cell is the reciprocal of the measure of the cell, thus implying that the dynamics is ergodic. To recapitulate the notation: Transitions between the ground state $|3\rangle$ and the excited states $|1\rangle$ and $|2\rangle$ respectively are mediated by a single radiation field with photon destruction and creation operators a and $a^\dagger$. Direct transitions between the two excited states are forbidden. Setting the detuning to zero, and defining $\sigma_{ij} = |i\rangle\langle j|$ as usual, the system is modeled by the Hamiltonian

$$H_{\rm V} = \sum_{j=1}^{3} \omega_j \sigma_{jj} + \Omega a^\dagger a + \chi a^{\dagger 2} a^2 + \lambda a(\sigma_{13} + \sigma_{23}) + \text{h.}c. \tag{7.6}$$

The results that emerge for the recurrence time statistics of the mean photon number are in agreement with those obtained earlier. We consider strong nonlinearity compared to the interaction strength, setting $\chi/\lambda = 5$. As a representative case, let the atom initially be in $|1\rangle$, and the field initially in a CS. For $\nu = 1$, the first return distribution to a cell in the effective phase space is discrete, with several incommensurate frequencies, consistent with what is expected for regular (quasiperiodic) dynamics. In contrast, for $\nu = 10$, the distribution is exponential, indicative of hyperbolic dynamics. Further, the distributions for 2, 3 and 4 successive returns to a cell are uncorrelated, and are given by successive terms in the Poisson distribution.

A novel feature emerges, however, from a detailed time series analysis carried out using the package TISEAN [16] to implement the algorithm in [5]. Corresponding to the atom initially in $|1\rangle$, and the field initially in a CS with $\nu = 1$, $\lambda_{\max}$ is zero, consistent with a discrete first return distribution. However, for $\nu = 10$, while the

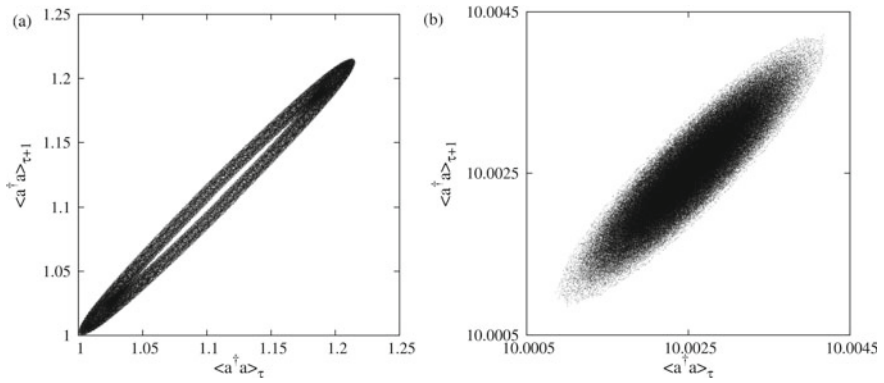

Fig. 7.3 Return maps of the mean photon number $\langle a^\dagger a \rangle$ in the bipartite system. Initial state $|1; \alpha\rangle$ with **a** $\nu = 1$ and **b** $\nu = 10$. These figures are reproduced from [15]

first return distribution is exponential in nature, $\lambda_{\max}$ remains equal to zero. It is clear that the limitation in the number of atomic transitions in this case plays a crucial role in determining the ergodicity properties of the observable. To understand this 'discrepancy' better, we turn now to the nature of the return maps (plots with $\langle a^\dagger a \rangle_\tau$ on the x-axis and $\langle a^\dagger a \rangle_{\tau+1}$ on the y-axis, corresponding to the two cases $\nu = 1$ and $\nu = 10$ as seen in Fig. 7.3[2]).

In the former case, consistent with a small value of ν, the return map has an annulus, whereas for large ν, it is entirely space-filling, reminiscent of a chaotic system, although $\lambda_{\max}$ is zero. This points to the important feature that, if the Hilbert space of a subsystem is small, the results from recurrence time statistics and return maps need not agree with what the Lyapunov exponent indicates about the dynamics.

Consider, now, a tripartite extension of the model at hand. Here, the two fields F_i $(i = 1, 2)$ mediate, respectively, the transitions $|3\rangle$ to $|i\rangle$. For zero detuning, and with Kerr-like nonlinearities in both fields with the same strength χ, setting the same value of the interaction strength λ between either field and the atom, another counter-intuitive result emerges. Investigations on the time series of the mean photon number of either field [15] reveal that, for certain initial states of the field, a positive value of $\lambda_{\max}$ could accompany a discrete first return distribution to a cell in the phase space. An example is the case of both fields initially in a CS with $\nu = 10$, with the atom initially in $|1\rangle$. Analysis of a long time series of the mean photon number corresponding to F_1, comprising 3×10^5 data points with time step unity, reveals that d_{emb} in this case is 7, with $\lambda_{\max} \approx 0.02$. However, the first return distribution is spiky, though tending to an exponential one, as can be seen from the envelope of the spikes. Thus, this investigation corroborates the general conclusion that the low dimensionality of the atomic Hilbert space is responsible for the unusual features in the dynamics of the observable concerned.

[2] Figure 7.3 is reproduced from *Dynamics of an open quantum system interacting with a quantum environment*, Shankar et al. [15] with permission from IOP Publishing.

7.5 The Tripartite HQ Model with Intensity-Dependent Couplings

7.5.1 The Model

We now revisit the tripartite HQ model comprising a three-level Λ-atom interacting with two radiation fields (Sect. 6.4.2). We recall that F_1 and F_2 induce $|1\rangle \leftrightarrow |3\rangle$ and $|2\rangle \leftrightarrow |3\rangle$ transitions respectively, while the transition $|1\rangle \leftrightarrow |2\rangle$ is dipole-forbidden. The general Hamiltonian incorporating field nonlinearities and atom-field intensity-dependent couplings is (setting $\hbar = 1$)

$$H_\Lambda = \sum_{j=1}^{3} \omega_j \sigma_{jj} + \sum_{i=1}^{2} \left\{ \Omega_i \, a_i^\dagger a_i + \chi_i \, a_i^{\dagger 2} a_i^2 \lambda_i \left[a_i \, f(\mathsf{N}_i) \, \sigma_{3i} + f(\mathsf{N}_i) \, a_i^\dagger \, \sigma_{i3} \right] \right\}. \tag{7.7}$$

Here $\sigma_{jk} = |j\rangle \langle k|$ are the Pauli spin operators, and $\{\omega_j\}$ are positive constants. χ_i represents the strength of the nonlinearity in F_i, and λ_i is the atom-field coupling parameter corresponding to the $|3\rangle \leftrightarrow |i\rangle$ transition ($i = 1, 2$). The IDC $f(\mathsf{N}_i) = (1 + \kappa_i \, \mathsf{N}_i)^{1/2}$, where $\mathsf{N}_i = a_i^\dagger a_i$. For simplicity, we shall set $\lambda_1 = \lambda_2 = \lambda$ and $\chi_1 = \chi_2 = \chi$. Further, we consider zero detuning, i.e., $\omega_3 - \omega_i - \Omega_i = 0$, $(i = 1, 2)$, set $\kappa_2 = 0$, and denote κ_1 by κ. For both fields initially in coherent states with sufficiently large $|\alpha|^2$ (say, 25), and for strong nonlinearity (say, $\chi/\lambda = 5$), we recall that the parameter space of H_Λ exhibits rich features during the dynamics. In particular, consider the time interval from initial time reckoned in terms of $\tau = \lambda t$, until $\tau = 12{,}000$. With small changes in the value of κ, substantial changes in the dynamics can be seen over the entire interval. The appearance of a bifurcation cascade in the entanglement measure corresponding to F_1 as κ is fine tuned, is mimicked effectively in the dynamics of the mean photon number (see Fig. 6.9). In particular, we recall that the cascade moves from entanglement collapse to a constant nonzero value for $\kappa = 0$ (with the collapse sustained over the entire time interval) through a pinched effect in the neighborhood of $\kappa = 0.002$ and 0.005, flanking a spread in the pinch at a special value $\kappa = 0.0033$. Further increase in κ creates a series of collapses and revivals culminating in oscillatory behavior close to $\kappa = 1$. A long time series of the observable $\langle N_1 \rangle$ (the mean photon number of F_1) reveals several other novel features, which could potentially be useful in relating classical dynamical systems theory to the dynamics of quantum observables. We now proceed to discuss this time series analysis in detail.

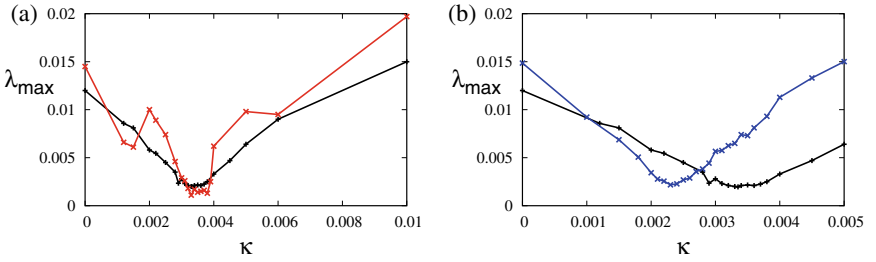

Fig. 7.4 **a** MLE versus κ for $N = 25{,}000$ (red curve) and $N = 3 \times 10^5$ (black curve). $|\alpha|^2 = 25$ and $\chi/\lambda = 5$. **b** MLE versus κ with $N = 3 \times 10^5$, $\chi/\lambda = 5$. $|\alpha|^2 = 25$ (black curve) and $|\alpha|^2 = 30$ (blue curve). These figures are reproduced from [17]

7.5.2 Time Series Analysis with Large and Small Data Sets

Following the procedure indicated earlier, the MLE can be computed [17]. We illustrate this by considering a long time series of the mean photon number $\langle N_1 \rangle$. For each chosen value of κ, this numerically generated data set comprises N_{tot} data points separated by equal time intervals (typically a scaled time step $\tau = \lambda \delta t = 1$). In order to examine only the long time regime (essentially beyond the time interval over which the bifurcation cascade occurs), the initial 10,000 data points are discarded. The resultant time series is denoted by $\{s(i)\}$ where $1 \leqslant i \leqslant N$ and $N = N_{\text{tot}} - 10{,}000$. We note that the range of values of $\{s(i)\}$ depends on the specific value of κ. Next, employing the procedure involved in carrying out the time series analysis which we have discussed earlier, an effective phase space of dimensions d_{emb} ($\ll N$) has been reconstructed from $\{s(i)\}$. In this space there are $N' = N - (d_{\text{emb}} - 1)t_d$ delay vectors $\mathbf{x}_j$ $(1 \leqslant j \leqslant N')$ given by

$$\mathbf{x}_j = \big[s(j),\ s(j + t_d), \ldots,\ s\big(j + (d_{\text{emb}} - 1)t_d\big)\big]. \tag{7.8}$$

Correspondingly there are d_{emb} Lyapunov exponents in the phase space. The MLE λ_{max} is computed using the standard TISEAN package.

The following interesting observations can now be made. The qualitative features of the plots of the MLE versus κ are similar for $N = 25{,}000$ and for $N = 3 \times 10^5$ data points (respectively, the red and black curves in Fig. 7.4a[3]). The curve becomes smoother with an increase in N. More important is the feature that the minimum of the MLE in both cases occurs at the same value of κ, which we denote by $\bar{\kappa}$. Although the short-time dynamics (including the bifurcation phenomenon around $\bar{\kappa}$) has been excluded in these data sets, the clear minimum in the MLE serves to identify this special value of κ. We emphasize that the value of $\bar{\kappa}$ is unique for a given value of $|\alpha|^2$. For instance, as seen in Fig. 7.4b when $|\alpha|^2 = 30$, $\bar{\kappa} = 0.0024$, and if $|\alpha|^2 = 25$,

[3] Figures 7.4, 7.5, 7.6 and 7.7 are reproduced from *Bifurcations, time-series analysis of observables, and network properties in a tripartite quantum system*, Laha et al. [17] with permission from Elsevier.

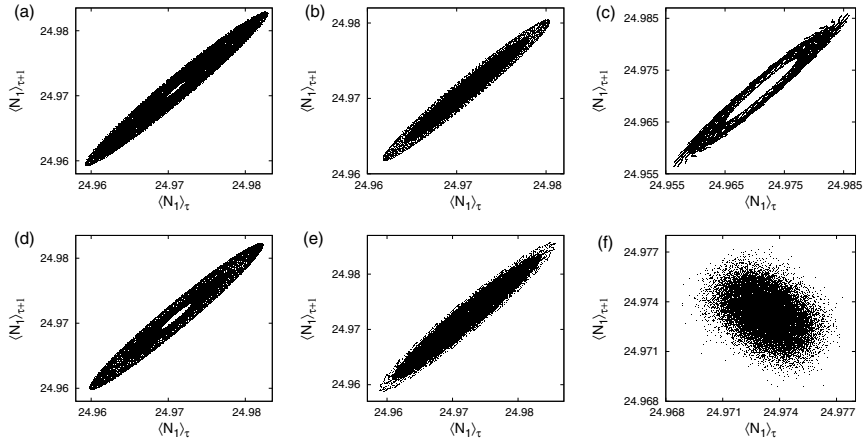

Fig. 7.5 Return maps of $\langle N_1 \rangle$. $|\alpha|^2 = 25$, $\chi/\lambda = 5$, and $\kappa =$ **a** 0, **b** 0.002, **c** 0.0033, **d** 0.005, **e** 0.02 and **f** 1. These figures are reproduced from [17]

$\bar{\kappa} = 0.0033$. We recall that the latter value is also a special value in the bifurcation cascade that occurs during the initial time interval corresponding to $|\alpha|^2 = 25$. The small numerical values of $\lambda_{\max}$, suggest weakly chaotic underlying dynamics of the observable. It has been verified, as shown in Fig. 7.4a that 25,000 data points alone suffice to capture the qualitative behavior of the dynamics in this system. We now summarize the main inferences drawn from the return maps and recurrence-time statistics, obtained with this reduced data set.

7.5.3 Return Maps and Recurrence Time Distributions

A detailed investigation of return maps and recurrence time statistics for various values of κ has been carried out [17], for $N = 25{,}000$, $|\alpha|^2 = 25$ and $\chi/\lambda = 5$.

The return maps in Fig. 7.5 correspond to $\langle N_1 \rangle$ for different values of κ. For $\kappa = \bar{\kappa}$, a prominent annulus is seen in the corresponding return map. This serves as a clear signature of this special value, because for $\kappa \neq \bar{\kappa}$, the return map is more 'dense'; and while other substructures are present, the absence of the distinct annulus is noteworthy. To complete the picture, we note that these substructures also disappear as κ approaches 1, and the return maps become more space-filling.

In order to obtain the recurrence time statistics, the first step is to coarse-grain the range of values in the time series of $\langle N_1 \rangle$ (for a given value of κ) into equal-sized cells. The distribution of the time of first return to a generic cell (given that the first time step takes $\langle N_1 \rangle$ to a value outside the initial cell) is obtained. In order to get a correct estimate of the recurrence time statistics, this procedure needs to be carried out for different values of κ. In each case, different initial cells and different cell sizes

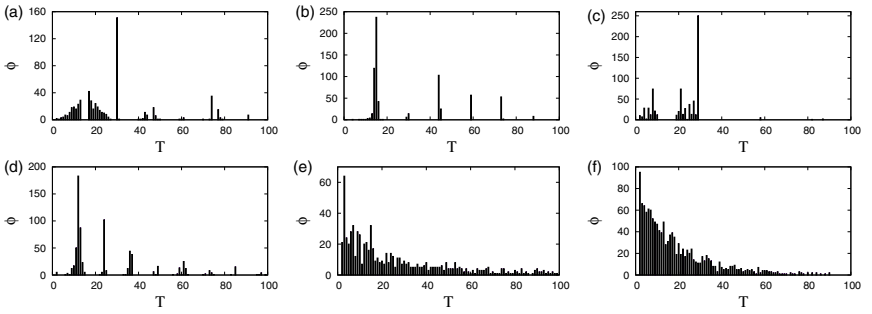

Fig. 7.6 First-return-time distribution of $\langle \mathsf{N}_1 \rangle$ for 50 equal-sized cells. $|\alpha|^2 = 25$, $\chi/\lambda = 5$, and $\kappa =$ **a** 0, **b** 0.002, **c** 0.0033, **d** 0.02, **e** 0.3 and **f** 1. These figures are reproduced from [17]

need to be considered. Typical first-return-time distributions are shown in Fig. 7.6. For values of κ close to 0, the distributions have a single pronounced spike. From our previous understanding, this is indicative of non-chaotic dynamics. With increase in the value of κ, the number of spikes in the first-return distribution also increase, till it becomes an exponential distribution as $\kappa \to 1$. The latter is reminiscent of chaotic dynamics. A qualitative feature of interest is worth pointing out here. For values of κ close to $\bar{\kappa}$, on either side of that value, all the other spikes in the distribution are to the right of the most pronounced spike. At $\kappa = \bar{\kappa}$, however, all these spikes occur to the left of the most pronounced one. The recurrence time distribution corresponding to the value $\bar{\kappa}$ is thus distinctly different from that for all other values of κ.

In what follows, we describe another tool from classical dynamical systems theory that has been exploited in understanding the dynamics of quantum observables.

7.5.4 Recurrence Plots and Recurrence Network

A clearer picture of the ergodicity properties of the observable concerned can be obtained by examining appropriate recurrence plots corresponding to these parameter values, with $N = 25{,}000$. These plots are particularly useful in relating time series analysis to the network analysis which we will carry out subsequently. We explain in brief their salient features before presenting the results obtained.

Recurrence plots are the outcome of a set of standard tools applied to a data set, in order to understand dynamics in a reconstructed phase space [18–21]. We begin with the $(N' \times N')$ recurrence matrix R whose elements are given by

$$R_{ij} = \Theta(\epsilon - \| \mathbf{x}_i - \mathbf{x}_j \|). \tag{7.9}$$

Here, N' is the number of delay vectors, Θ denotes the unit step function, and $\| \cdot \|$ is the Euclidean norm. It is clear from the definition of R that 'coarse graining' in

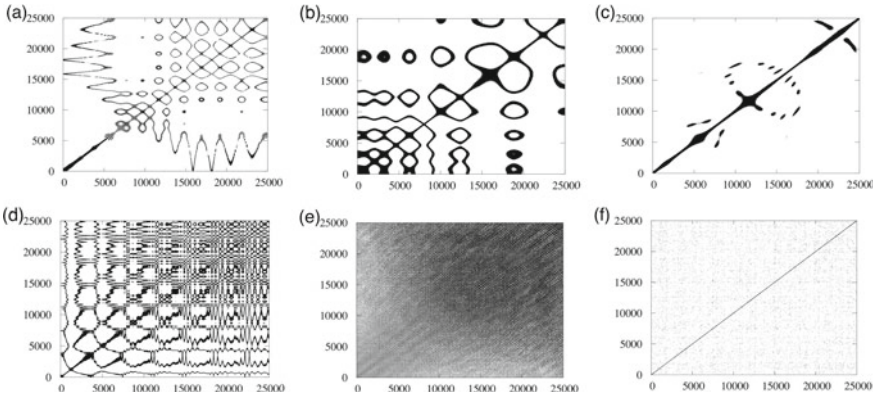

Fig. 7.7 Recurrence plots of $\langle N_1 \rangle$. $|\alpha|^2 = 25$, $\chi/\lambda = 5$, and $\kappa =$ **a** 0, **b** 0.002, **c** 0.0033, **d** 0.02, **e** 0.3 and **f** 1. These figures are reproduced from [17]

terms of a threshold parameter ϵ is necessary. A judicious choice of ϵ is important: too small a value of ϵ makes the plot very sparse with inadequate number of recurrences, while too large a value yields false recurrences. The choice of the optimal value of ϵ can be made, based on different criteria that have been proposed in the literature (see, for instance, [22–25]) It is useful to adopt the criterion suggested in the context of ϵ-recurrence networks, as this facilitates a transition to network analysis, where our aim will be to identify network quantifiers that capture the effects seen in the time series analysis [26].

We consider the $(N' \times N')$ Laplacian matrix L with elements

$$L = D - R + I \tag{7.10}$$

where I is the unit matrix, $D = \text{diag}\,(k_1, \ldots, k_{N'})$, and $k_i = \sum_{j=1}^{N'} R_{ij} - 1$. L is a real symmetric matrix, and each of its row sums vanishes. Together with the Gershgorin circle theorem (see, e.g., [27]), these properties imply that the eigenvalues of L are real, non-negative, and that at least one of the eigenvalues is zero. Increasing ϵ upward from zero, the smallest value of ϵ (denoted by ϵ_c) for which the next eigenvalue of L becomes nonzero, is to be determined. For each value of κ, a recurrence plot ($N' \times N'$ grid with elements R_{ij}) is obtained with ϵ set equal to ϵ_c. As in the earlier cases, these plots highlight the importance of the special value $\bar{\kappa}$.

It is evident from Fig. 7.7 that the plot is distinctly sparse for $\kappa = \bar{\kappa}$, in contrast to denser plots for other values of κ. The latter have either relatively better defined structures or are merely space-filling. Thus, as in the case of return maps, the qualitative features of the plot suffice to pick out the special value $\bar{\kappa}$ in the bifurcation cascade.

The Laplacian matrix L also plays a central role in network analysis. One of the reasons for using network analysis for investigating the behavior of classical dynamical systems is the necessity to work with small data sets which capture the

important features of the dynamics buried in a long time series. The advantage is that the 'smallness' could permit less computer-intensive procedures. While several types of network analysis have been examined in the literature, recurrence networks were investigated in considerable detail in an interesting paper [28] and their novel features highlighted. Further, topological properties of recurrence networks can be related to the nontrivial statistical properties of the effective phase space densities. This facilitates in placing the conceptual framework of the analysis on a firm footing. The program involves interpreting the recurrence matrix appropriately, so that the dynamics is effectively replaced by a time-independent network with nodes and links. The general procedures of network analysis have been applied to diverse problems in classical physics. Examples include investigations on environment-induced amplitude death in networks [29], and a network model for explaining synapse loss and progress of Alzheimer's disease [30]. Since large data sets are now available for measured quantities pertaining to the dynamics of certain quantum systems as well, more recently, this analysis has been applied to specific quantum observables in different tripartite models and in analogous classical counterpart systems wherever possible [31]. Before we summarize the inferences pertaining to the usefulness of network analysis, we first explain its main features [32], by adapting it to the present context of the tripartite system, in which the time series of the mean photon number is used as the starting point.

The detailed network analysis for this tripartite system has been carried out in [33]. As mentioned earlier, for each value of κ, we have a long time series $\{s(i)\}$ ($i = 1, 2, \ldots, N$, where $N = 25{,}000$) in the interval $10{,}000 \leqslant \tau < 35{,}000$. As is evident, the range of variation of $\{s(i)\}$ naturally depends on the value of κ. Each time series is first rescaled to fit into the unit interval [0, 1], in order to facilitate comparison between them. Now consider any one of the time series, denoted by $\{y(i)\}$. It has been demonstrated in the context of classical dissipative systems [34] that the conversion of $\{y(i)\}$ into a uniform deviate time series $\{u(i)\}$ stretches the attractor (the region of phase space into which a dissipative system eventually settles down) in all directions to fill the unit interval optimally, without affecting the dynamical invariants, and provides better convergence of data points. In the quantum context, too, it must be remembered that the subsystem corresponding to F_1 is dissipative as it exchanges energy with the other two subsystems. As a result of this the mean photon number, treated as analogous to a classical dynamical variable, will settle down in an appropriate attractor. For each $y(i)$, if $n(i)$ is the number of data points $\leqslant y(i)$, the uniform deviate time series is given by $u(i) = n(i)/N$.

Next, employing the method described in [35] for carrying out the time series analysis for networks, a suitable time delay t_d is identified. We recall that this is the first minimum of the time-delayed mutual information. An effective phase space of dimensions $d_{\text{emb}} (\ll N)$ is reconstructed from $\{u(i)\}$ and t_d. In this phase space we then have a total of $N' = N - (d_{\text{emb}} - 1)t_d$ state vectors $\mathbf{x}_j$ $(1 \leqslant j \leqslant N')$ given by

$$\mathbf{x}_j = [u(j),\ u(j + t_d), \ldots,\ u(j + (d_{\text{emb}} - 1)t_d)]\,. \tag{7.11}$$

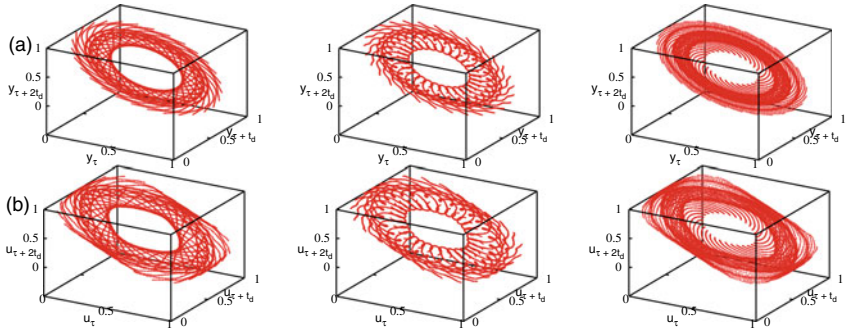

Fig. 7.8 Left to right: Attractors for $\kappa = 0.0032,\ 0.0033$ and 0.0034, respectively. **a** Top: rescaled time series $\{y(i)\}$. **b** Bottom: uniform-deviate time series $\{u(i)\}$. (τ = dimensionless time, t_d = time delay.) These figures are reproduced from [33]

We have used the same notation $\mathbf{x}_j$ as in the case of the recurrence plots discussed earlier, to denote the state vectors (or nodes) in the effective phase space. It is to be noted, however, that the space is now constructed from a much smaller and rescaled data set, and there is no dynamics to consider. The relevant matrix here is the adjacency matrix A, with $L = D - A$ (equivalently, $A = R - I$, where I is the $(N' \times N')$ unit matrix), and D is a diagonal matrix with elements $D_{ij} = \delta_{ij}\, k_i$ (no summation over i) and $k_i = \sum_{j=1}^{N'} A_{ij}$ is the degree of the node i. Two nodes $\mathbf{x}_i$ and $\mathbf{x}_j$ $(i \neq j)$ are connected iff $A_{ij} = 1$. The network therefore comprises links between such connected nodes. It is fully connected if L has a single zero eigenvalue, and the second-smallest eigenvalue l_2 is positive. As before, by calculating l_2 for different values of ϵ, the smallest value of ϵ for which $l_2 > 0$ is ascertained. In keeping with the notation used earlier in the context of recurrence plots, we denote this value by ϵ_c.

In Fig. 7.8,[4] we see the manner in which the conversion of the rescaled time series $\{y(i)\}$ into a uniform deviate time series $\{u(i)\}$ stretches the attractor. The figure displays the attractor plots for $\kappa = 0.0032$, 0.0033 and 0.0034, respectively. It is evident from the figure that the special value $\kappa = 0.0033$, corresponding to $|\alpha|^2 = 25$, is captured in the qualitative features of the corresponding attractor, which are quite distinct from those for even very slightly different values of κ. This observation provides an interesting connection between the short and long time scales in the problem. A striking feature is that, as κ is varied from 0 to 0.1, the parameter ϵ_c calculated from the corresponding $\{u(i)\}$ changes from 0.025 for $\kappa = 0$ to 0.200 for $\kappa = 0.1$, passing through a minimum value of 0.020 when $\kappa = 0.0033$.

[4] Figures 7.8 and 7.9 are reproduced from *Recurrence network analysis in a model tripartite quantum system*, Laha et al. [33] with permission from IOP Publishing.

7.5.5 Network Analysis

Classical network analysis involves some important quantifiers of networks such as average path lengths, link densities, clustering coefficients, transitivities, degree distributions and assortativities, which characterize the dynamics underlying generic networks. These have been defined and their usefulness has been discussed extensively in the literature (see, for instance, [32, 35–37]). Of direct interest to us here is the sensitivity of the network quantifiers to the value of κ. Our investigations show that, in the tripartite system under consideration, the clustering coefficient and transitivity are good quantifiers that carry signatures of the special value $\bar{\kappa}$ corresponding to each value of $|\alpha|^2$.

For ready reference, we define several network quantifiers below. The average path length APL (or the characteristic path length) of a network of P nodes is given by

$$\mathrm{APL} = \frac{1}{P(P-1)} \sum_{i,j}^{P} d_{ij}, \tag{7.12}$$

where d_{ij} is the *shortest* path length connecting nodes i and j. The link density LD of the network is defined as

$$\mathrm{LD} = \frac{1}{P(P-1)} \sum_{i}^{P} k_i, \tag{7.13}$$

where k_i is the degree of the node i (defined earlier in terms of the elements of the adjacency matrix A). The local transitivity characteristics of the network are quantified by the local clustering coefficient, which measures the probability that two randomly chosen neighbours of a given node i are directly connected. For finite networks, this probability is given by

$$C_i = \frac{1}{k_i(k_i-1)} \sum_{j,k}^{P} A_{jk}\, A_{ij}\, A_{ik}. \tag{7.14}$$

The global clustering coefficient (CC) is defined as the arithmetic mean of the local clustering coefficients taken over all the nodes of the network, i.e.,

$$\mathrm{CC} = \frac{1}{P} \sum_{i}^{P} C_i. \tag{7.15}$$

The transitivity $\mathcal{T}$ of a network is defined as

$$\mathcal{T} = \sum_{i,j,k}^{P} A_{ij}\, A_{jk}\, A_{ki} \Big/ \sum_{i,j,k}^{P} A_{ij}\, A_{ki}. \tag{7.16}$$

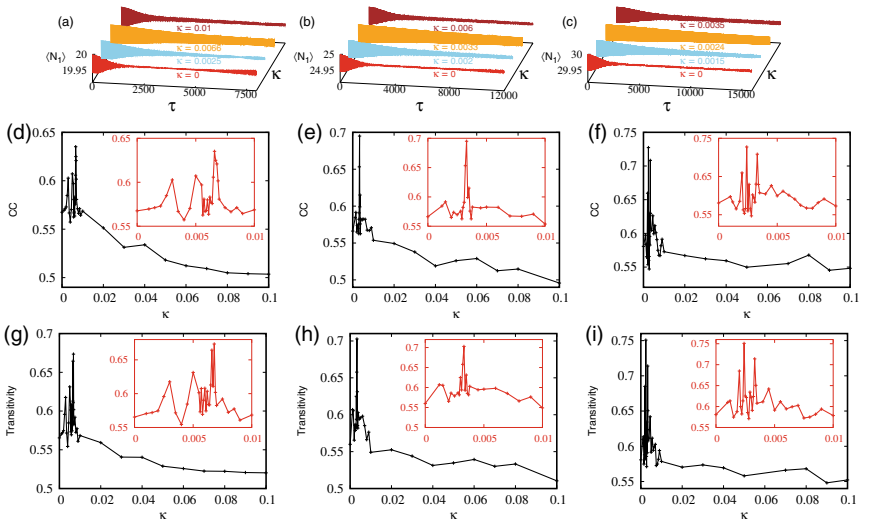

Fig. 7.9 Top panel: $\langle N_1 \rangle$ versus τ for different values of κ, with $|\alpha|^2$ equal to **a** 20, **b** 25 and **c** 30. Clustering coefficient versus κ (center panel) and transitivity versus κ (bottom panel) for **d** and **g** $|\alpha|^2 = 20$, **e** and **h** $|\alpha|^2 = 25$, and **f** and **i** $|\alpha|^2 = 30$. These figures are reproduced from [33]

It is straightforward to verify numerically that, for all values of κ, APL decreases and LD increases with increasing ϵ. This is to be expected: the number of links in the network increases with increasing ϵ, and this results in a shorter average path length, and larger link densities. However, CC decreases for sufficiently large ϵ, indicating that the closed loops in the network do not increase significantly. In the reconstructed dynamics, this would suggest that periodic orbits are few, and long-period and/or ergodic trajectories are more prevalent.

An interesting inference that emerges through extensive numerical investigations of the dynamics as a function of κ for different values of $|\alpha|^2$, is the following. In every case, the special value $\bar{\kappa}$ identified in the short-time dynamics retains its distinct nature in the long-time dynamics as well, as reflected in the clustering coefficient obtained from ϵ-recurrence network analysis. The pinching effect in the neighborhood of $\bar{\kappa}$ is evident in Fig. 7.9a–c that depict the short-time dynamics for $|\alpha|^2 = 20$, 25 and 30, respectively. The corresponding dependence of CC and the transitivity on κ for fixed ϵ_c is shown in Fig. 7.9d–i. (The precise value of ϵ_c obviously depends on the value of κ). It is evident that at $\kappa = \bar{\kappa}$ ($= 0.0066$, 0.0033 and 0.0024, respectively for $|\alpha|^2 = 20$, 25 and 30) obtained from the bifurcation cascade, the corresponding clustering coefficient is at its maximum. The insets in Fig. 7.9d–i highlight the peaks in both CC and the transitivity at the special value $\bar{\kappa}$ for different values of $|\alpha|^2$.

7.6 Concluding Remarks

In this chapter, we have focussed on the novel aspects that emerge in the ergodicity properties of quantum observables, when tools from classical dynamical systems theory are applied to quantum systems, with the objective of comprehending the dynamics on various time scales, and with optimal data sets. We get glimpses of surprising features that arise in the quantum context, counter-intuitive to expectations based on the results of time series analysis applied to classical dynamical variables. Expectations regarding the ergodicity properties of quantum observables based on recurrence time statistics in classical dynamical systems need not hold in several HQ systems, in which the finite number of atomic levels is indicative of the 'size' of the effective Hilbert space. This feature has been demonstrated in this chapter by an investigation of the time evolution of the mean photon number of a radiation field both in the presence and absence of intensity-dependent couplings. A specific tripartite model of field-atom interactions has been used to advantage, in order to demonstrate the appearance of a bifurcation cascade as the intensity parameter κ is tuned over a small range of values. Surprisingly, the salient features of the cascade are mirrored in the manner in which the maximal Lyapunov exponent (obtained from both large and relatively smaller data sets procured from the time series of the mean photon number) varies with κ. Even more interesting is the fact that a network constructed out of this time series can be used to identify quantifiers which reflect the important features of the bifurcation cascade and the Lyapunov exponents computed from the time series. The present discussion is merely a report of exploratory investigations in this regard. More work needs to be done on several model systems along these lines before a more comprehensive picture emerges about the dynamics of quantum observables.

References

1. H.D.I. Abarbanel, *Analysis of Observed Chaotic Data* (Springer, New York, 1996)
2. F. Takens, Detecting strange attractors in turbulence, in *Dynamical Systems and Turbulence*, ed. by D. Rand, L.S. Young (Springer, Berlin, 1981)
3. A.M. Fraser, H.L. Swinney, Phys. Rev. A **33**, 1134 (1986)
4. P. Grassberger, I. Procaccia, Phys. Rev. Lett. **50**, 346 (1983)
5. M.J. Rosenstein, J.J. Collins, C.J. de Luca, Physica D **65**, 117 (1993)
6. H. Kantz, Phys. Lett. A **185**, 77 (1994)
7. C. Sudheesh, S. Lakshmibala, V. Balakrishnan, Phys. Lett. A **373**(32), 2814–2819 (2009). https://doi.org/10.1016/j.physleta.2009.06.010
8. M. Kac, *Probability and Related Topics in Physical Sciences* (Interscience, New York, 1959)
9. M. Theunissen, C. Nicolis, G. Nicolis, J. Stat. Phys. **94**, 437 (1999)
10. S. Seshadri, S. Lakshmibala, V. Balakrishnan, Phys. Lett. A **256**, 15 (1999)
11. M. Hirata, Ergod. Theor. Dyn. Syst. **13**, 533 (1993)
12. V. Balakrishnan, M. Theunissen, Stoch. Dynam. **1**, 339 (2001)
13. M. Hirata, Dyn. Sys. Chaos **1**, 87 (1995)
14. V. Balakrishnan, G. Nicolis, C. Nicolis, Stoch. Dynam. **1**, 345 (2001)

15. A. Shankar, S. Lakshmibala, V. Balakrishnan, J. Phys. B: At. Mol. Opt. Phys. **47**(21), 215505 (2014). https://doi.org/10.1088/0953-4075/47/21/215505
16. R. Hegger, H. Kantz, T. Schreiober, Chaos **9**, 413 (1999)
17. P. Laha, S. Lakshmibala, V. Balakrishnan, Phys. Lett. A **384**(23), 126565 (2020). https://doi.org/10.1016/j.physleta.2020.126565
18. J.-P. Eckmann, S.O. Kamphorst, D. Ruelle, Europhys. Letts. **4**, 973 (1987)
19. M. Thiel, M.C. Romano, J. Kurths, Phys. Lett. A **330**, 343 (2004)
20. N. Marwan, M.C. Romano, M. Thiel, J. Kurths, Phys. Rep. **438**, 237 (2007)
21. N. Marwan, Eur. Phys. J. Spec. Top. **164**, 3 (2008)
22. G.M. Mindlin, R. Gilmore, Physica D **58**, 229 (1992)
23. J.P. Zbilut, C.L. Webber Jr., Phys. Lett. A **171**, 199 (1992)
24. J.P. Zbilut, J.-M. Zaldivar-Correnges, F. Strozzi, Phys. Lett. A **297**, 173 (2002)
25. M. Thiel, M.C. Romano, J. Kurths, R. Meucci, E. Allaria, F.T. Arecchi, Physica D **171**, 138 (2002)
26. D. Eroglu, N. Marwan, S. Prasad, J. Kurths, Nonlinear Proc. Geoph. **21**, 1085 (2014)
27. V. Balakrishnan, *Mathematical Physics* (Springer, Cham, 2020), p. 191
28. R.V. Donner, Y. Zou, J.F. Donges, N. Marwan, J. Kurths, New J. Phys. **12**, 033025 (2010)
29. V. Resmi, G. Ambika, R.E. Amritkar, G. Rangarajan, Phys. Rev. E **85**, 046211 (2012)
30. G. Kashyap, D. Bapat, D. Das, R. Gowaikar, R.E. Amritkar, G. Rangarajan, V. Ravindranath, G. Ambika, Sci. Reps. **9**, 6555 (2019)
31. P. Laha, S. Lakshmibala, V. Balakrishnan, Int. J. Theor. Phys. **59**, 3476 (2020)
32. M. Newman, *Networks: An Introduction* (Oxford University Press, Oxford, 2010)
33. P. Laha, S. Lakshmibala, V. Balakrishnan, Europhys. Lett. **125**(6), 60005 (2019). https://doi.org/10.1209/0295-5075/125/60005
34. R. Jacob, K.P. Harikrishnan, R. Misra, G. Ambika, Phys. Rev. E **93**, 012202 (2016)
35. Y. Zou, R.V. Donner, N. Marwan, J.F. Donges, J. Kurths, Phys. Rep. **787**, 1 (2019)
36. D.J. Watts, S.H. Strogatz, Nature **393**, 440 (1998)
37. S. Boccaletti, V. Latora, Y. Moreno, M. Chavez, D.-U. Hwang, Phys. Rep. **424**, 175 (2006)

Chapter 8
Conclusion and Outlook

Tell all the truth but tell it slant.
Emily Dickinson

The broad theme of this work falls under the large canopy of explorations into the quantum-classical divide. In particular, we have focused our attention on contexts in which the links between the classical and quantum regimes are strong. Bearing in mind the importance of nonclassical effects displayed by different quantum states and the manner in which these effects are mirrored in the behavior of observables, we have reported details of various investigations on generic CV, spin and HQ systems from which instructive and valuable inferences can be drawn. We have placed emphasis on two approaches.

First, we have explained procedures to estimate different properties of the quantum state of a system *solely* from tomograms. A substantial body of literature exists on both classical and quantum tomograms, and we have drawn attention wherever possible to important results of direct relevance to us. However, applications of the tomographic approach to estimate nonclassical effects displayed by specific states (in particular, various states of light), identification of bipartite entanglement indicators solely from tomograms, and validating the role of these indicators by comparing their performance with that of standard measures of entanglement systematically, are less well known. We have emphasized these aspects as well, as they open up several possibilities for future investigations.

Second, we have outlined how to identify important aspects of the dynamics of quantum observables through tools such as time series and network analysis. While these have been employed extensively to examine data in a variety of classical systems, relatively less research has been carried out on analyzing data pertaining to quantum observables using these tools. In this work, we have elaborated upon this aspect of dynamical systems theory, which holds the promise of novel avenues of research.

© The Author(s), under exclusive license to Springer Nature Switzerland AG 2022

S. Lakshmibala and V. Balakrishnan, *Nonclassical Effects and Dynamics of Quantum Observables*, SpringerBriefs in Physics,
https://doi.org/10.1007/978-3-031-19414-6_8

As elaborated in the preceding chapters, attempts to extract information about nonclassical effects in a readily and easily accessible form from histograms of distributions which respect the requirements of *classical* probability theory, provide information on the overlap between classical and quantum physics. Further, assessment of the extent to which results from classical ergodicity theory hold for the temporal evolution of quantum observables sheds light on the manner in which the nature of the initial quantum state, the interaction strengths between subsystems of the full system, and the inherent nonlinearities in the system control both the short-time and long-time dynamics of those observables.

A substantial part of this work uses optical tomograms to investigate and quantify nonclassical effects. We have elaborated upon the limitations that arise in identifying the occurrence of revivals and fractional revivals by inspecting tomograms, particularly in systems with more than one time scale. We have demonstrated, using procedures reported in the literature, how successful and exact computations of various types of squeezing such as quadrature, higher-order and entropic squeezing can be carried out from tomograms of different optical states without performing state reconstruction. Several bipartite entanglement indicators that can be obtained directly from optical and spin tomograms have been proposed, and their performance gauged through detailed comparison with standard measures of entanglement. The definitions of some of these indicators stem from properties related to distances between probability distributions that are defined even in classical settings. For illustrative purposes, we have mostly examined nonclassical properties captured through numerically generated tomograms of quantum states obtained from known initial states evolving under given nonlinear Hamiltonians. The purpose of this exercise is to create a 'glossary' of the roles played by different initial states, their extent of coherence and the ratio of various coupling strengths in any given system on the subsequent evolution, and on the nonclassical features displayed.

We have also used experimental data (obtained from NMR experiments) to understand squeezing and bipartite entanglement as quantified from tomograms. Further, in certain cases, equivalent circuits corresponding to specific HQ systems have been analyzed in the IBM quantum computing platform. Among other advantages, this provides an estimate of the effects of decoherence and experimental losses. Thus, comparison between experimentally obtained tomograms and numerically generated tomograms has been made feasible in certain cases.

Before we comment on the dynamics of observables, it is worth recapitulating briefly the main conclusions about the usefulness of tomograms in assessing nonclassical effects. The performance of tomographic entanglement indicators reveals that, while there is no universal, ready-to-use, efficient indicator applicable in all cases, some general remarks can be made about their efficacy in specific contexts. This is not an unusual feature, as even in the case of entanglement monotones and witnesses constructed from the density matrix, no universal characterizer of entanglement can be uniquely identified, particularly for systems with high-dimensional Hilbert spaces. We have observed that ξ_{BD} performs as well as ξ_{TEI} close to avoided energy-level crossings in both CV and HQ systems. On the other hand, for bipartite states which are superpositions of Hamming-uncorrelated states, such as the

eigenstates of certain number-conserving Hamiltonians, $\xi_{\rm IPR}$ is a better entanglement indicator than $\xi_{\rm TEI}$. Even $\varepsilon_{\rm IPR}$ (the corresponding indicator from a single section of the tomogram) suffices to estimate entanglement reliably near avoided energy-level crossings. In the case of bipartite CV systems, $\xi'_{\rm TEI}$ (obtained by averaging only over the dominant values of $\varepsilon_{\rm TEI}$) is found to be a reasonably good entanglement indicator. However, the degree to which it agrees with $\xi_{\rm SVNE}$ is very sensitive to the precise initial state, the nature of the interaction, and the inherent nonlinearities in the system. In contrast to the foregoing, $\xi'_{\rm TEI}$ is a poor entanglement indicator for qubit systems, and we need to compute $\xi_{\rm TEI}$.

We now highlight novel effects seen in the dynamics of quantum observables, and the limitations of theorems pertaining to recurrences in coarse-grained dynamics, obtained in classical ergodicity theory, when applied to quantum observables. While the importance of observables in both theoretical calculations and in measurements has been well recognized even from the early days of quantum physics, the increased possibility in recent years of experimental identification and production of new quantum states (particularly in CV systems) has opened up several avenues of research. We have illustrated the importance of the mean and higher moments of quadrature operators in identifying various aspects of the revival phenomena, and also demonstrated how fractional revivals are captured in CV tomograms. A similar line of thought is also used to clarify how the mean photon number and the quadrature operators mirror signatures of dips in entanglement during the temporal evolution of a bipartite CV system, under nonlinear Hamiltonians.

The connection with classical dynamical systems theory is brought about through a time series analysis of the mean photon number in a generic bipartite CV system. It has been illustrated that the sensitivity of this observable to the initial state increases exponentially with the departure from coherence of the initial radiation field. Extensions of this line of research to HQ systems, comprising radiation fields and atoms in interaction, provide a wide arena for exploring entanglement sudden death and entanglement collapse to a constant nonzero value over significant intervals of time. The sensitivity of these effects to the precise nature of the initial state, and the interplay between various couplings and nonlinearities, have been demonstrated in simple terms using generic models which could describe laboratory experiments.

The appearance of a bifurcation cascade in the bipartite entanglement in a generic system with a tunable intensity-dependent coupling between field and atom provides a new approach to understanding the classical-quantum overlap. The time series and network analysis of the mean photon number reveals interesting connections between seemingly unrelated phenomena, namely, the manner in which the Lyapunov exponent calculated with long data sets changes with the value of the tunable intensity-dependent parameter, the appearance of a bifurcation cascade in short time scales, network quantifiers such as the clustering coefficient, and so on. We have also illustrated how the finite dimensionality of the atomic Hilbert space leads to a connection between recurrence time distributions, on the one hand, and the value of the Lyapunov exponent, on the other, that is different from predictions based on classical ergodic theory.

In the light of the foregoing summary of results based on the two approaches mentioned earlier, it will not be an exaggeration to claim that these investigations, if pursued further, could reveal several novel aspects pertaining to the classical-quantum divide. The use of tomograms alone for extracting as much information as possible about the quantum state would have an increased significance in the case of multipartite systems with high-dimensional Hilbert spaces, as is expected of arrays of qubits and different HQ platforms that are presently being envisaged. State reconstruction becomes very messy and cumbersome as the Hilbert space dimensionality increases, and it increasingly uses more 'supports' from network theory, faster computational techniques and machine learning. The tomographic approach that we have described provides elegant procedures to assess trends in nonclassical effects during the time evolution of systems. An important line of research would be to extract multipartite entanglement indicators. Yet again, the genuine 'quantumness' of correlations captured directly from tomograms needs to be substantiated by considering Bell-type inequalities obtained from the tomograms. While such inequalities have certainly been reported in the literature, their application to specific systems and the documentation of the nature of correlations for various initial states of HQ and CV systems is still in its infancy. Other aspects that need to be examined relate to the appearance and effects of sub-Planckian structures in tomograms, as well as variants of the basic entropic uncertainty principle that can be readily obtained from tomograms.

From the point of view of the time series and network analysis of quantum observables, much more needs to be done before a clear picture of the applicability and limitations of known results from dynamical systems theory can be built up. Since network analysis in this context is still in its infancy, the first task would be the identification of good network quantifiers which capture the salient features of the dynamics of observables in generic quantum systems. A comparison of the efficacy of these quantifiers in classical counterpart systems, wherever available, is necessary to draw firm conclusions about the classical-quantum similarities and differences, In particular, more investigations need to be carried out in order to understand where and how departures from known results on recurrence time distributions in classical dynamics arise in the quantum case. A comparative study between multipartite systems comprising several two-level or three-level atoms (thus involving high-dimensional Hilbert spaces), as compared to CV systems, also needs to be carried out in this context.

We have outlined some of the aspects that need further investigation. The picture that has emerged so far, using the two approaches that constitute the central theme of this work, is nowhere near completion. It can be stated with a fair measure of certainty that many more novel features and unanticipated results are yet to be unearthed.